ANALYSIS OF A CYCLOIDAL WAVE ENERGY CONVERTER USING UNSTEADY REYNOLDS AVERAGED NAVIER-STOKES SIMULATION

by

Christopher J. Caskey

B.Sc.Eng, University of New Brunswick, 2012

A Thesis Submitted in Partial Fulfillment
of the Requirements for the Degree of

Master of Science in Engineering

in the Graduate Academic Unit of Mechanical Engineering

Supervisor: Tiger L. Jeans, PhD, Mechanical Engineering

Examining Board: A. Gordon Holloway, PhD, Mechanical Engineering
Joseph W. Hall, PhD, Mechanical Engineering
Brian Lowry, PhD, Chemical Engineering

This thesis is accepted by the
Dean of Graduate Studies

THE UNIVERSITY OF NEW BRUNSWICK

May, 2014

ABSTRACT

A computational fluid dynamic study was completed to investigate the two-dimensional wave generation and cancellation characteristics of the Atargis Cycloidal Wave Energy Converter (CycWEC). The numerical modeling was based on the unsteady Reynolds average Navier Stokes (URANS) equations and determined the free surface fluctuations using the volume of fluid method. A specialized hybrid grid design was required to accurately resolve the complex viscous flow field resulting from one or more hydrofoils rotating beneath the free surface at a constant angular velocity. The research progressed incrementally from single and two-hydrofoil wave generation concluded with two-hydrofoil wave cancellation. Unlike previous inviscid simulations, the URANS simulations were able to model nonlinear free surface interactions and viscous effects, allowing shaft torques to be numerically predicted for first time. It also provided complete velocity and pressure fields which previous experimental work could not.

A grid refinement and time step sensitivity study are completed to increase simulation accuracy and computational efficiency. Fluctuations of wave height, surface pressure distribution, hydrodynamic force, and device efficiency from generated and cancelled wave fields are examined in detail for various hydrofoil pitch angles. For two-

hydrofoil wave generation with large pitch angles URANS simulations predicted 94% of the required shaft power is transferred directly to the generated wave field. When operated as an energy extraction device the URANS simulations predicted that up to 92% of the incident wave field was cancelled and 82.7% of the average incident wave power was converted to useful shaft power.

DEDICATION

To my girlfriend, Tracy, my brother, Alexander, and my parents, Graeme and Martha.

ACKNOWLEDGEMENTS

I would like to express my sincere gratitude and appreciation to my supervisor, Dr. Tiger Jeans of the University of New Brunswick. This research would not have been possible without your help, knowledge and contributions. I appreciated your support and encouragement as challenges arose during the research process. Working with you has been a great overall experience and am grateful to have had this opportunity.

To the examining committee of Dr. Gordon Holloway, Dr. Joseph Hall, and Dr. Brian Lowry, thank you for helping me complete the final stages of my research in a timely manner. I would like to thank my colleagues in the lab H-12, Cory, Stanley, and Adam for their often helpful technical discussions, and for making the many hours we spent in the lab together enjoyable. My gratitude is also extended to Atargis Energy Corporation for their financial support.

To my parents, Martha and Graeme, thank you for your continuous support and guidance as I continue to develop as an engineer. I'd like to thank Eric Thomas, on behalf of my brother Alex and I, for providing that extra spark to get up early and keep working hard, even when the going gets tough. Finally, I would specifically like to thank my girlfriend Tracy for always being there to support me when I needed it most, and for challenging me to push my own limits and see what I can become.

Table of Contents

List of Tables

List of Figures

Nomenclature

c – Chord length

C_g – Group velocity

C_P – Pressure coefficient

C_R – Radial force coefficient

C_T – Tangential force coefficient

D – Water depth

D_s – Submerged depth of mass source zone

E – Total average energy per unit surface area

E_{Shaft} – Total shaft power per unit width

$\bar{E}_A$ – Average incident wave power per unit width

$\bar{E}_{Shaft}$ – Total average shaft power per unit width

$\bar{E}_T$ – Average total wave power per unit width

$\bar{E}_U$ – Average up-wave wave power per unit width

$\bar{E}_1$ – Average primary wave power per unit width

$\bar{E}_2$, $\bar{E}_3$ – Average first, second harmonic wave power per unit width

$\dot{E}_T$ – Total wave power per unit width

f – Surface tension force

F_1 – Blending factor in SST turbulence model

g – Gravitational acceleration

g_i – Component of the gravitational acceleration

h_s – Height of mass source zone

H – Wave height

H_A – Incident wave height

H_1 – Fundamental wave height

H_2 – First harmonic wave height

k – Turbulent kinetic energy per unit mass

k_w – Wave number

p – Static pressure with hydrostatic pressure removed

p_{mean} – Mean pressure

p_∞ – Atmospheric pressure

$\overline{p}$ – Time-averaged pressure

P_k – Shear production of turbulence

R – Radius of CycWEC

s_m – Mass source function

t – Time

T – Period

T_{std} – Period of rotating hydrofoil

u – Horizontal component of the flow velocity

u_i – Flow velocity tensor

u'_i – Fluctuating component of the flow velocity tensor

$\bar{U}_i$ – Time-average flow velocity tensor

v – Vertical component of the flow velocity

w_s – Width of mass source zone

W_1, W_2, W_3 – Fundamental down-wave wave field, first and second harmonic

W_{-1}, W_{-2}, W_{-3} – Fundamental up-wave wave field, first and second harmonic

W_A – Approaching Wave Field

x – Global coordinate in horizontal direction

x_c – Horizontal position of center shaft of CycWEC

x_o – Horizontal position for start of Ω

x_s – Horizontal position of center shaft of the mass source zone

X_1 – Body-fixed coordinate in horizontal direction of top hydrofoil

X_2 – Body-fixed coordinate in horizontal direction of bottom hydrofoil

y – Global coordinate in vertical direction

y_c – Submerged depth of center shaft of CycWEC

y_s – Submerged depth of center shaft of the mass source zone

y^+ – Y-plus, measurement of the first node height near a wall or other surface

Y_1 – Body-fixed coordinate in vertical direction of top hydrofoil

Y_2– Body-fixed coordinate in vertical direction of bottom hydrofoil

Greek Symbols

α_1 – Pitch angle of top hydrofoil

α_2 – Pitch angle of bottom hydrofoil

δ_{ij} – Identity matrix

Δt – Time step size

Δx – Mesh spacing size in the x-direction

Δy – Mesh spacing size in the y-direction

ε_G – Average wave generation efficiency

ε_{PC} – Average power conversion efficiency

ε_{TP} – Average total power extraction efficiency

ε_{WC} – Average wave cancellation efficiency

η – Vertical elevation of the free surface

γ – Volume fraction

λ – Wavelength

λ_1 – Fundamental wave wavelength

λ_2 – First harmonic wave wavelength

μ – Dynamic viscosity

μ_t – Turbulent viscosity

ν_{mean} – Mean kinematic viscosity

φ_A – Phase angle of incident wave

$\varphi_1, \varphi_2, \varphi_3$ – Phase angle of fundamental wave, first and second harmonic

ψ – Phase shift of a wave field

ψ_A – Phase shift of an incident wave field

$\psi_1, \psi_2, \psi_3,$ – Phase shift of the fundamental wave field, first and second harmonic

ω – Angular speed

ϖ – Turbulence frequency

ρ – Density

ρ_{air} – Density of air

ρ_{mean} – Mean density of element

ρ_{water} – Density of water

$\rho\overline{u'_i u'_j}$ – Reynolds stresses in tensor form

θ – Rotational position, measured from the y-axis to the quarter chord point on hydrofoil

σ_{k3}, β', $\sigma_{\omega 3}$, α_3 , β_3 – Constants in SST turbulence model

CHAPTER 1

1. INTRODUCTION

1.1. Background

Due to the steadily increasing global population and the industrialization of China, India and other parts of Asia, global energy requirements have continued to grow. Fossil fuels have been heavily relied upon to meet the increasing energy demands. These fossil fuels are, however, in limited supply and are projected to run out before the turn of the century [1]. Without the use of fossil fuels the energy demand required for continual global development cannot currently be met. For this reason, there is a need for alternative forms of energy collection and extraction methods.

The tremendous potential of ocean waves to provide clean renewable energy is well known. The total annual global energy requirement is currently estimated at 16 Peta Watt Hours (PWh=10^{12} kWh), and according to Boyle [2], The World Energy Council has estimated the total annual energy stored in ocean waves to be 17.5 PWh. Thus, ocean

wave energy remains one of the most abundant renewable energy sources available that is virtually untapped.

The fundamental properties of an ocean wave are summarized in Figure 1 where λ represents the wavelength and H represents the wave height, which is measured from wave-crest to wave-trough. The wave propagation direction and the circular paths of the water particles below the wave are also shown. The rate at which the wave propagates, or the wave speed, is equal to the quotient of the wavelength and the wave period [3].

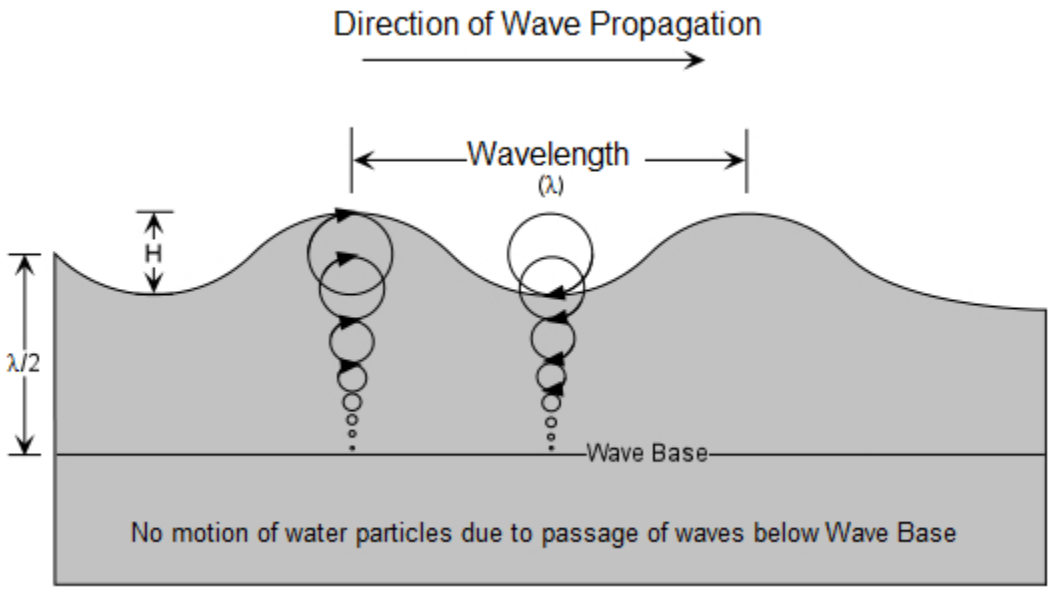

Figure 1 - Deep ocean wave schematic [4].

Unlike an ocean current, which transfers energy using a net mass transport, deep ocean waves transport energy in the direction of wave propagation without a net mass transport. Using inviscid linear wave theory it can be shown that the total average energy per unit surface area is defined as:

$$E = \frac{1}{8}\rho g H^2 \tag{1}$$

where ρ is the density of the fluid, and g is the gravitational acceleration [3]. The average rate at which the wave energy is transferred, commonly referred to as the total wave power per unit width, is defined as:

$$\dot{E}_T = EC_g \tag{2}$$

where C_g is the group velocity, which for deep ocean waves is equal to half the wave speed [3]. Thus, the magnitude of energy transported by an ocean wave is proportional to both the wavelength and wave height.

The mean position of water particles under a deep ocean wave is considered to be at the center of their circular rotational path, as shown in Figure 1 [3]. The radius of the rotational path cannot exceed half of the wave height, and decays exponentially until the water depth reaches the wave base. Once the water depth reaches the wave base, which is equal to half the wavelength, the water particles are no longer affected by the deep ocean wave.

As a result of the unsteady nature of the power available in ocean waves and the extreme environment in which the energy converter must operate, creating an efficient, reliable, and cost effective ocean wave energy converter has been a significant engineering challenge. A major draw-back of many existing wave energy converters is that the energy is converted to reciprocating mechanical motion, which then drives an intermediate power-take-off system that converts the energy to a useful form [5]. Atargis Energy Inc. is developing a novel lift based Cycloidal Wave Energy Converter

(CycWEC) that is capable of converting wave energy directly to rotational mechanical energy. A 1:10 scale model of the CycWEC is shown in Figure 2.

Figure 2 - 1:10 Scale model of the Atargis CycWEC [6].

The CycWEC consists of one or more rotating hydrofoils aligned parallel with the incident wave crest and located just below the free surface, as shown in Figure 3. The local flow field induced by the propagating incident wave will cause the hydrofoils to rotate about the main shaft at the incident wave frequency [9].

Based on its operating principle the CycWEC is defined as a wave terminator in which the goal is to “terminate” the incident wave, thereby extracting its energy. As pointed out in Falnes [1], and showing in Figure 4, an effective wave terminator must generate a one-sided wave field propagating in the same direction as the incident wave

field and be of equal amplitude, but with 180° of phase shift. The interaction of the incident wave and the wave generated by the WEC results in the complete cancellation of the incident wave past the converter, also shown in Figure 4, and thus the wave energy is completely extracted.

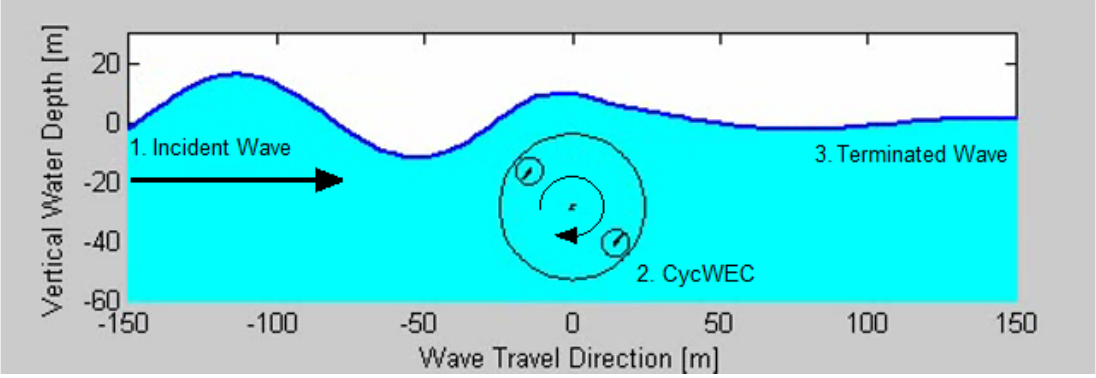

Figure 3 - Wave termination capabilities of the CycWEC based on inviscid potential flow simulations [11]. Note the free surface elevation is scaled up by a factor of ten for visualization purposes.

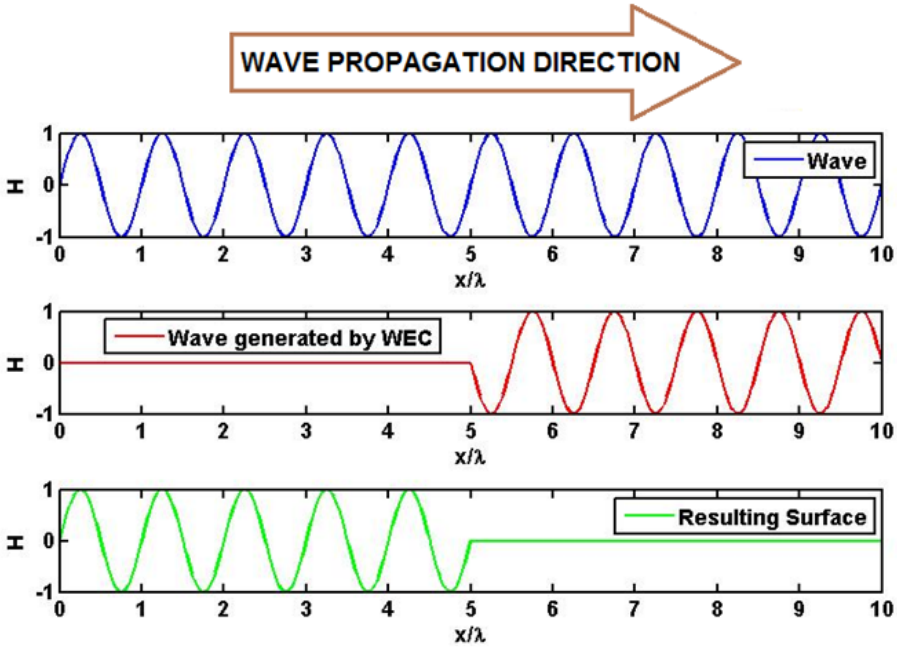

Figure 4 - Operating principles of a wave terminating device.

1.2. Research Objectives

To date numerical investigations of the CycWEC have employed inviscid potential flow methods. In this work, investigations will be extended to include viscous and non-linear effects using unsteady Reynolds Averaged Navier-Stokes (URANS) simulations. The URANS simulations are superior to the inviscid simulations because they model nonlinear free surface interactions and viscous effects, while allowing the resulting shaft torques to be predicted. In addition, the URANS simulations provide details of the flow field that experiments cannot, such as complete velocity and pressure fields.

As previously mentioned, for effective wave termination the ideal wave energy converter must generate a single sided wave of equal amplitude and period as the incident wave while being exactly out of phase. Therefore, understanding the wave generation and cancellation abilities of the CycWEC as a function of the various device parameters, such as the hydrofoil pitch angle, is critical. To accomplish this, a series of specific research objectives were developed:

- Develop a two-dimensional CFD model of a single hydrofoil rotating beneath a free surface at a fixed pitch angle and angular speed.
- Complete a grid and time step sensitivity study to ensure that a grid and time step independent solutions have been achieved.
- Investigate the wave generation properties of a single rotating hydrofoil as a function of blade pitch angle.
- Develop a two-dimensional CFD model of the CycWEC model featuring two hydrofoils rotating beneath a free surface at a fixed pitch angle and angular speed.

- Investigate the wave generation properties of the CycWEC model featuring two hydrofoils as a function of blade pitch angle.
- Develop a two-dimensional numerical wave tank to generate a desired incident wave field based on user input.
- Investigate the two-dimensional wave cancellation abilities of the CycWEC using the numerical wave tank and a CycWEC model featuring two hydrofoils. Emphasis will be put on investigating the resulting shaft torques, viscous effects, and the hydrodynamic efficiency of the CycWEC.

CHAPTER 2

2. LITERATURE REVIEW

2.1. Previous CycWEC Investigations

Research involving wave energy extraction using rotating hydrofoils initially began in 1980 at TU Delft University [8]-[10]. Experimental results supported the concept that a single hydrofoil attached to a fully submerged horizontal shaft could operate as a winch in regular long crested waves. Further numerical and experimental investigations on the topic by Marburg [8] and van Sabben [10] demonstrated the feasibility of the CycWEC concept, as well as its ability to potentially synchronize with the incoming wave frequency and rotational phase. However, the conversion efficiencies were found to be only a few percent.

The original work completed at TU Delft University was extended at the United States Air Force Academy [11]. The primary objective was to increase conversion efficiencies by operating at higher blade speeds relative to the wave-induced velocity and

by using a feedback-flow-control to continuously adjust the blade orientation and position to match the incident wave field. An initial potential flow analysis completed by Siegel and al. [11] predicted efficiencies greater than 99% when the CycWEC was subject to incoming harmonic waves. The device efficiency was heavily dependent on the relative phase between the incident wave and rotating hydrofoils and magnitude of the hydrofoil's bound circulation. Siegel and al. [12] experimentally investigated the performance of a 1:300 scale CycWEC model using a two-dimensional wave tank. Efficiencies for harmonic wave cancellation were found to be as high as 95%, which agreed well with the findings of Siegel and al. [11].

The performance of the CycWEC in a long crested irregular wave field was initially investigated numerically by Jeans and al. [5] and experimentally by Siegel and al. [12]. Jeans and al. [5] concluded that a two hydrofoil device could achieve efficiencies ranging from 70 to 90% when exposed to a standard Bretschneider energy spectrum [22]. However, several numerical simulations were able to achieve efficiencies as high as 98%. Further 1:300 scale experiments by [12] verified these results, achieving experimental efficiencies of 77% in a similar two-dimensional wave field. The current limitation preventing improved device efficiency in an irregular wave field is the performance of the feedback-flow-controller.

More recently, a one-tenth scale prototype, as shown in Figure 2, has been manufactured for large scale testing at the Texas A & M offshore technology research centre. The prototype consists of two hydrofoils located 180° apart, and each having a modified NACA 0015 profile with a chord of c = 0.75 m, and span of 4.5 m. The hydrofoils rotate at a radius of 1 meter from the axis of rotation. A major advantage of

this larger scale prototype is that it can quantify the amount of power directly delivered to the CycWEC shaft, while previous experiments and potential flow simulations could not. Preliminary experiments verified that the device was able to generate a net power output of 370 W at the design point when subject to a harmonic incoming wave [13].

2.2. Previous Computational Studies of Hydrofoils near a Free Surface

Recently, viscous numerical simulations of a lifting hydrofoil translating in the vicinity of a free surface were completed at the University of Edinburgh by Gretton and al. [14]. The principle research objective was to complete a mesh refinement study so that an optimal mesh was obtained that accurately predicted the resulting wave field in the downstream wake. Free surface heights were compared to the results of the classical experiment of Duncan [15] who measured the free surface height behind a two-dimensional submerged hydrofoil being towed at a constant horizontal velocity and angle of incidence. For the numerical simulations, a coarse, medium and fine mesh were created and it was found that the coarse mesh did not capture the free surface elevation in the wake accurately. However further investigation revealed that by coarsening only the mesh surrounding the hydrofoil and not the mesh created to capture the free surface, the free surface elevations were the same as those predicted by the medium density mesh.

2.3. Numerical Wave Tank Development

To numerically test the wave cancellation abilities of a wave energy converter, a desired incident wave field must be generated to interact with the energy converter. To accomplish this, numerical wave tanks have been developed that can produce regular or

irregular wave fields in both two and three-dimensions [16]-[17]. Note this research only investigated two-dimensional numerical wave tanks.

Creating waves within a numerical domain requires one of three different wave-making approaches, namely: ‘inlet-velocity boundary condition’, ‘momentum source term’, or a ‘mass source term’. Guo and Steen [17] investigated the accuracy of these three wave-making techniques as a function of both grid densities and time steps size. The overall computational efficiencies of the three methods were also investigated.

For the inlet-velocity boundary condition method the complete velocity distribution and free surface position is required at the boundary. This method does not work without a free stream current velocity because the high turbulent viscosity ratio causes problems with the numerical solver along the inlet boundary [17]. Since the inlet-velocity boundary condition is located directly on the inlet interphase it is more sensitive to any errors in the velocity field or free surface modeling at the inlet compared to the momentum or mass source terms. The inlet-velocity boundary condition approach was found to be an effective method to study the interaction between waves and currents. However, when any type of body was present in the flow that caused a reflection back towards the inlet, this method lost its numerical accuracy. When subject to different time step sizes and grid density it was found that 1200 time steps per wave period, 90 cells per wavelength and 20 cells per wave height, were required for simulation results to replicate analytical results [17].

The momentum source term method generates a wave field using an internal momentum source zone that manipulates the URANS equations by adding a source term that specifies the horizontal and vertical components of velocity and the averaged

pressure required to generate a wave field [17]. A supplementary feature that is required for the application of a momentum source term to be successful as a wave-maker is the presence of a zone located between the momentum source zone and the numerical domain of interest that absorbs any reflected waves. The reflected wave must be absorbed before reaching the momentum source zone or they will distort the outgoing generated wave field. The wave absorption zone must however be unidirectional as to not absorb the generated wave field that is propagating from the momentum source zone towards the numerical domain of interest. With a wave absorption zone in place, the momentum source term wave-maker can create a constant wave field whose amplitude and frequency matches analytical values. In terms of time step and grid density, the momentum source term was able to produce accurate results with 600 time steps per wave period and 45 cells per wavelength, which was an improvement compared to the computational requirements of the inlet-velocity boundary condition wave-making technique [17].

The final wave-making technique that was investigated involved the addition of a mass source zone, located underwater, to the domain. A wave field is generated within the mass source zone by introducing a mass source term to the continuity equation. The result of a correctly defined mass source term is a user defined surface wave which propagates towards the outer boundaries. Unlike the momentum source term, the mass source term method does not required a reflected wave absorption zone as any reflected waves from a body in the domain will pass through the numerical wave-maker without distorting the generated wave field [17]. This occurs because the momentum source is a force per unit volume in a specified direction, so any unexpected velocity components, such as those resulting from a reflected wave, become part of the new velocity field [19].

A fluid mass source however, adds a mass flow rate per unit volume and only requires the direction of the added mass to be fully defined, not the exact velocity profile [19]. Since waves travel without a net mass transport, they are able to propagate through the mass source term without negatively affecting the generated wave field.

One drawback to the mass source term is that the amplitude of the generated wave is affected by the vertical position of the source zone relative to the free surface and the overall size of the source zone. However, using suggested parameters ranges based on previous work by Guo and Steen [17], small amplitude waves of desired wave height and frequency can be generated using basic linear wave theory. It is also important to note that unlike the other wave-making techniques, for the mass source term method a two-side wave train is generated that propagates in both directions from the source. When the performance of the mass source term was examined as a function of time step and grid spacing it was found that the time step and grid spacing requirements were the same as those for the momentum source term [17].

CHAPTER 3

3. Methodology

The required parameters and procedures to complete URANS simulations that test the single and double hydrofoil wave generation and cancellation abilities of the CycWEC model are defined in this chapter. Details are also included concerning the development of a numerical wave tank. For generating the incident wave field the geometry of the numerical domain is initially explained, the flow solver is then outlined and lastly the applied boundary conditions are explored.

3.1. Geometry

The hydrofoil geometry and rotation rate were chosen to match the existing 1/10 scale model experiments. It is important to note that for the current research a two-dimensional approach for modeling the CycWEC was chosen to help reduce the computational requirements of the simulations. Essentially, the simulations model a hydrofoil of infinite span, which is equivalent to assuming the hydrofoil has a very large aspect ratio. This

assumption is similar to previous computational studies by Siegel and al. [11] which were also two-dimensional. Figure 5 displays a schematic of the CycWEC, as will be considered throughout this research. It features two hydrofoils that are attached parallel to the horizontally oriented main shaft at a radius, R = 1 m, and rotating clockwise at angular speed ω = 2.503 rad/s in the positive θ direction, which is measured from the y-axis to the quarter chord point of each hydrofoil. The two hydrofoils are offset by $\theta = 180°$. The rotational point for these simulations remains at the fixed submerged depth y_c = 1.4 m which is measured relative to an inertial Cartesian coordinate system (x, y) with y = 0 m being the undisturbed free surface. The water depth, D = 5.8 m, was also measured relative to the undisturbed free surface.

The hydrofoils are modified NACA 0015 hydrofoils, which were cambered so that when the pitch angle is α_1 or $\alpha_2 = 0°$ the mean camber line is aligned with the rotational path. Note that the pitch angles α_1 and α_2 are defined in Figure 5 as a rotation of the body-fixed coordinate system (X_1, Y_1) or (X_2, Y_2) with their origins located at the hydrofoil quarter chord. The chord length, c, had a value of 0.751 m.

The local elevation of the free surface relative to its undisturbed position is defined as η, and the peak-to-peak amplitude of the generated waves (or wave height) is defined by H. The approaching incident ocean wave, W_A is assumed to travel left to right, and waves generated by the CycWEC propagating in the opposite direction of W_A are considered travelling in the up-wave direction and are identified as W_{-1}, W_{-2}, W_{-3}. Generated waves propagating in the same direction as W_A are considered to be travelling down-wave and are identified as W_1, W_2, W_3. Note that the subscript 1 represents the fundamental wave, while subscripts 2 and 3 represent the 1st and 2nd harmonics, respectively.

The mass source zone, which physically represents a wave making device, is located up-wave relative to the CycWEC. It has a central point located at (x_s, y_s) and a mass source zone height and width of h_s and w_s, respectively. The submerged depth of the mass source upper surface from the undisturbed free surface is D_s.

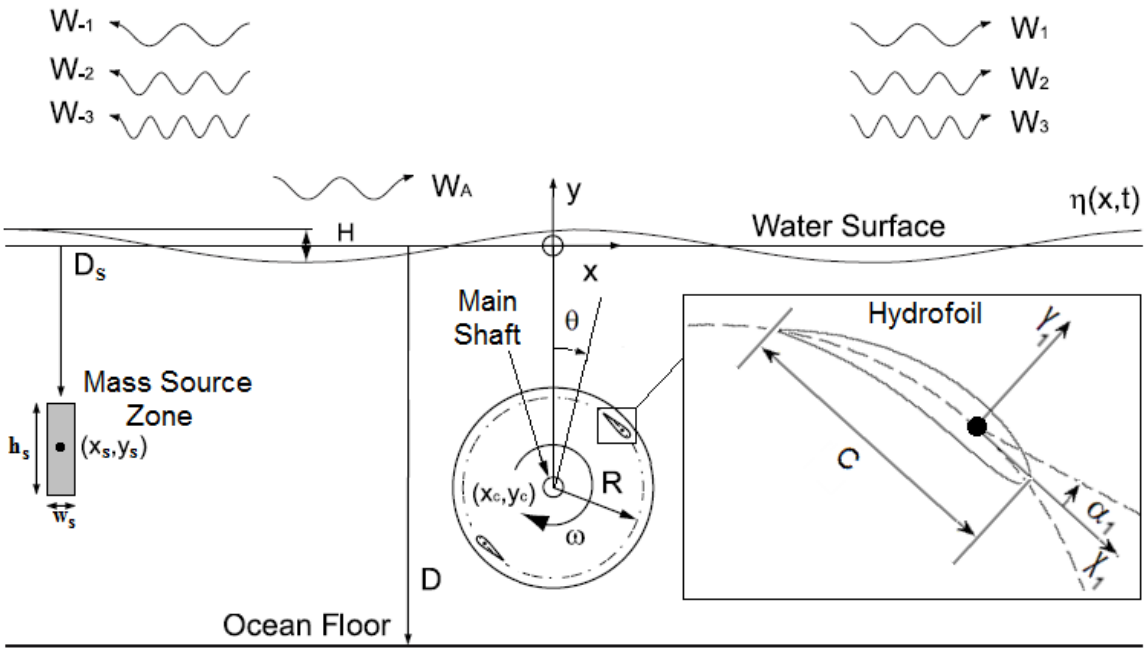

Figure 5 - A schematic of CycWEC two-hydrofoil geometry with mass source zone. Note α_1 = 0° in this figure.

3.2. Flow Solver

In the current research the resulting unsteady flow field is modeled using the unsteady Reynolds averaged Navier-Stokes (URANS) equations and the free surface is modeled using the volume of fluid method. To include an internal wave-maker in the numerical domain, a mass source term is employed. Numerical beaches are also present near the boundaries to invoke numerical wave dissipation and prevent waves from reaching the boundaries and reflecting back into the domain of interest.

3.2.1. Unsteady Reynolds Averaged Navier-Stokes Solver

The URANS simulations employ ANSYS CFX, a commercially available finite element/ finite volume based unsteady Navier-Stokes solver [19]. To fully solve a high Reynolds number turbulent flow field would require an impractical amount of computational resources due to the presence of extremely small grid elements needed to fully capture all the turbulent length scales. To improve the practicality of numerical simulations the URANS method approximates the turbulent fluctuations of the flow based on an average and fluctuating component of the velocity field [19]. Using this approach the velocity is modelled in tensor form is as follows:

$$u_i = \overline{U_i} + \overline{u'_i} \tag{3}$$

where u_i is the flow velocity tensor, $\bar{U}_i$ is the time-averaged flow velocity tensor, and u'_i is the fluctuating component of the flow velocity tensor [19].

The continuity equation, accounting for mass conservation, in tensor form is:

$$\frac{\partial \rho}{\partial t} + \frac{\partial \rho \overline{U_i}}{\partial x_i} = 0 \tag{4}$$

where ρ is the density of the fluid, and t is time [19]. The Reynolds averaged momentum equation in tensor form is therefore:

$$\frac{\partial(\rho \overline{U_i})}{\partial t} + \frac{\partial(\rho \overline{U_j}\,\overline{U_i})}{\partial x_j} = -\frac{\partial \overline{p}}{\partial x_i} + \frac{\partial}{\partial x_j}\left(\mu\left(\frac{\partial \overline{U_i}}{\partial x_j} + \frac{\partial \overline{U_j}}{\partial x_i}\right)\right) + \rho g_i - \frac{\partial}{\partial x_j}\left(\rho \overline{u'_i}\,\overline{u'_j}\right) \tag{5}$$

where $\overline{p}$ is the time-averaged pressure, μ is the dynamic viscosity, g_i is the component of the gravitational acceleration in the direction of x_i, and $\rho \overline{u'_i}\,\overline{u'_j}$ are known as the Reynolds

stresses. The addition of Reynolds stresses to the momentum equation as a result of time-averaging results in six additional unknowns, three normal stresses and three shear stresses [19]. To close the system of mean flow equations, the unknown Reynolds stresses must be modelled using turbulence models.

The Shear Stress Transport (SST) turbulence model is a two-equation model that uses an extended Bossinesq relationship to relate the Reynolds stress terms in the URANS equations to the velocity gradient in the flow as follows:

$$-\rho\overline{u'_i}\overline{u'_j} = \mu_t\left(\frac{\partial\overline{U_i}}{\partial x_j} + \frac{\partial\overline{U_j}}{\partial x_i}\right) - \frac{2}{3}\rho k\delta_{ij} \tag{6}$$

where μ_t is the turbulent viscosity, k is the turbulent kinetic energy per unit mass, and δ_{ij} is the identity matrix [19]. The Bossinesq relationship is based on the Reynolds stresses being proportional to the mean rate of deformation [19]. The SST turbulence model is a hybrid turbulence solver which employs the k-ε turbulence model in the fully turbulent region far from the wall and the k-ω turbulence model near the wall. This is accomplished by substituting the rate of viscous dissipation for the product of the turbulent frequency and the turbulent kinetic energy [19]. The governing transport equation for the turbulent kinetic energy per unit mass, k, in tensor form is:

$$\frac{\partial(\rho k)}{\partial t} + \frac{\partial(\overline{U_i}\rho k)}{\partial x_i} = \frac{\partial}{\partial x_i}\left(\left(\mu + \frac{\mu_t}{\sigma_{k3}}\right)\frac{\partial k}{\partial x_i}\right) + P_k - \beta'\rho k\varpi \tag{7}$$

where P_k is the shear production of turbulence, ϖ is the turbulence frequency, σ_{k3} and β' are constants. The transport equation for the turbulent frequency, ϖ, in tensor form is then:

$$\frac{\partial(\rho\varpi)}{\partial t}+\frac{\partial(\overline{U_i}\rho\varpi)}{\partial x_i}=\frac{\partial}{\partial x_i}((\mu+\frac{\mu_t}{\sigma_{\varpi 3}})\frac{\partial\varpi}{\partial x_i})+(1-F_1)2\rho\frac{1}{\sigma_{k3}\varpi}\frac{\partial k}{\partial x_i}\frac{\partial\varpi}{\partial x_i}+\alpha_3\frac{\varpi}{k}P_k-\beta_3\rho\varpi^2 \quad (8)$$

where $\sigma_{\varpi 3}$, α_3 ,and β_3 are constants, and F_1 is a blending factor [19]. The transport equations for turbulent kinetic energy and turbulent frequency both follow a similar form. The first term on the left hand side of equation (7) & (8) is composed of a time rate of change for the transported variable, which is followed by a term defining transport of the variable by convection. The right hand side of the transport equations are composed of the transport of the variable by turbulent dissipation, the rate of production of the variable and rate of dissipation of the variable [19].

3.2.2. Free Surface Modeling - The Volume of Fluid Method

The concept of modeling the free surface fluctuations using the volume of fluid method was initially introduced by Hirt and Nichols in 1979 [20]. The method allows the position of the free surface to be determined using a series of volume-averaged flow equations and an advection equation [20]. The result of the volume of fluid method is that each element in the numerical domain is assigned a single value for the water volume fraction, γ. For two-phase flow, the water volume fraction has a value of unity in the water phase and zero in air. The free surface is then approximated as the position where the water volume fraction is 0.5 within the elements that contain both water and air. An example is shown in Figure 6 of the volume of fluid method being applied to model an air bubble submerged in water.

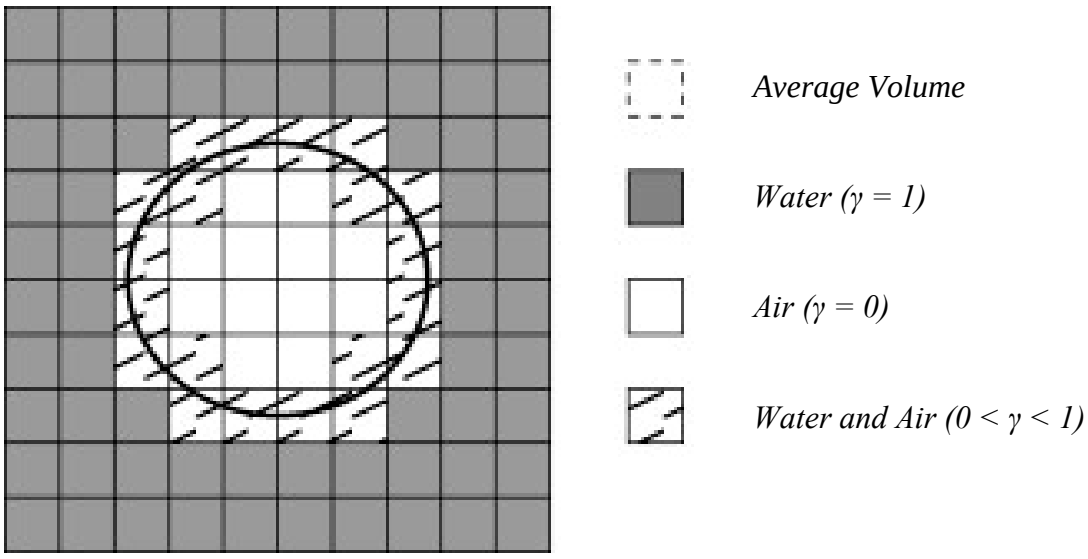

Figure 6 - Volume of fluid method modeling an air bubble submerged in water [21]

The volume fraction, γ, is a scalar property of the fluids within each control volume in the numerical domain. The variation of the volume fraction is governed by an advection equation as follows:

$$\frac{\partial \gamma}{\partial t} + \frac{\partial u\gamma}{\partial x} = 0 \tag{9}$$

$$\frac{\partial \gamma}{\partial t} + \frac{\partial v\gamma}{\partial y} = 0 \tag{10}$$

where *u* and *v* are the horizontal and vertical component of the flow velocities [21]. With the volume fraction value resolved for each element, the location of the free surface requires the development of a set of equations that define the flow properties within each element. The mean density for the element is solved as follows:

$$\rho_{mean} = \gamma\rho_{water} + (1-\gamma)\rho_{air} \tag{11}$$

where ρ_{mean} is the mean density, ρ_{water} is the density of water and ρ_{air} is the density of air [21]. A mean value is also determined for the pressure (p_{mean}) and kinematic viscosity (ν_{mean}) using the same method as equation (11). The mean density, pressure and viscosity combined with the assumption that the velocity of the two phases is continuous across the interface results in a continuity and momentum equation unique to each element [19]. The continuity equation is defined as follows:

$$\frac{\partial\rho_{mean}}{\partial t} + \frac{\partial(\rho_{mean}u)}{\partial x} + \frac{\partial(\rho_{mean}v)}{\partial y} = 0 \tag{12}$$

and the momentum equations are defined as:

$$\frac{1}{\rho_{mean}}\frac{\partial\rho_{mean}}{\partial t} + \frac{\partial u}{\partial t} + u\frac{\partial u}{\partial x} + v\frac{\partial u}{\partial y} = -\frac{1}{\rho_{mean}}\frac{\partial p_{mean}}{\partial x} + \nu_{mean}\left(\frac{\partial^2 u}{\partial x^2} + \frac{\partial^2 u}{\partial y^2}\right) + f \tag{13}$$

$$\frac{1}{\rho_{mean}}\frac{\partial\rho_{mean}}{\partial t} + \frac{\partial v}{\partial t} + u\frac{\partial v}{\partial x} + v\frac{\partial v}{\partial y} = g - \frac{1}{\rho_{mean}}\frac{\partial p_{mean}}{\partial y} + \nu_{mean}\left(\frac{\partial^2 v}{\partial x^2} + \frac{\partial^2 v}{\partial y^2}\right) + f \tag{14}$$

where f is the surface tension force [21]. The transient density term is present to account for the temporal fluctuations in the mean density within the element.

3.2.3. Internal Wave-Generation - Mass Source Term

As previously noted, numerical wave generation for a CFD simulation can be achieved by appropriately prescribing an inlet-velocity boundary condition, an internal momentum source, or an internal mass source term. When compared, the mass source term method was selected for this research because no free stream current was desired in the flow field which eliminated the inlet-velocity method and because it is significantly

simpler to implement than the momentum source term method while obtaining similar performance.

For two-dimensional numerical wave generation, the mass source term is incorporated into the governing equations of the solver through the continuity equation as follows:

$$\frac{\partial u}{\partial x} + \frac{\partial v}{\partial y} = s_m(x, y, t) \tag{15}$$

where $s_m(x,y,t)$ is a nonzero mass source function inside a defined source zone [18]. By design, the mass source term is able to simultaneously produce two wave fields that propagate in opposite directions away from the source zone.

The mass source term utilized in this research was successfully developed and applied by [18] for the numerical generation of small amplitude waves of short and long wavelengths. The mass source strength is a function of the induced horizontal and vertical velocity components of a linear progressive wave field and the CFD mesh size in the x-direction, Δx, within the mass source zone. Using linearized inviscid wave theory [22], the horizontal velocity component of a progressive wave field is defined as follows:

$$u(x, y, t) = \frac{H\omega \cosh\left[(k_w(y + D)\right]}{2\sinh\left[k_w D\right]} \cos\left[k_w x - \omega t + \psi\right] \tag{16}$$

where $u(x,y,t)$ is the horizontal velocity component of the wave field, k_w is the wave number, and ψ is the phase shift of the wave field [22]. The vertical velocity component of a progressive wave field is defined as follows:

$$v(x,y,t) = \frac{H\omega \sinh\left[(k_w(y+D)\right]}{2\sinh\left[k_w D\right]} \sin\left[k_w x - \omega t + \psi\right] \tag{17}$$

where *v(x,y,t)* is the vertical velocity component of the wave field [22]. Based on these velocity components the mass source strength is defined in [18] as follows:

$$s_m(x,y,t) = \frac{4H\omega \sinh\left[k_w D\right]\cosh\left[(k_w(y+D)\right]}{\left(\sinh\left[2k_w D\right] + 2k_w D\right)\Delta x} \cos\left[k_w x - \omega t + \psi\right] . \tag{18}$$

Within ANSYS CFX the mass source strength function is incorporated into the solution through a Total Mass Source which defines the total mass of fluid being introduced to, or subtracted from, the domain per second. The velocity fields required to generate a linear progressive wave are developed as a direct result of the spatial and temporal variations in mass source strength as defined in equation (18).

The strength of a fluid mass source term is defined as a mass flow rate into the mass source zone [24]. In principle, a mass source term operates like a momentum source term because both numerically add or subtract momentum to the domain. However, mass source terms differ from a momentum source term, because they introduce secondary source terms into all other equations [24]. These secondary source terms require all the components of velocity along with the mass source strength to be defined within the mass source zone [24].

If spatially invariant mass sources are used and have positive source strengths, the specified velocity components are applied along the boundaries of the source zone to define the direction of the fluid flowing from the mass source zone into the domain [24]. Once the mass source strength becomes negative, all specified velocity components values are ignored by the solver which then uses the local velocity fields to regulate the

direction of the fluid flowing from the domain into the mass source zone [24]. It must be noted that the magnitude of mass flowing in and out of the source zone is only regulated by the strength of the mass source term.

If a spatially variant mass source term is applied to generate a wave field, as it is in this research, the specified components of velocity can be set equal to zero but must still be defined [24]. The variation in mass source strength throughout the mass source zone regulates the outflow direction and replaces the need for the flow direction to be predetermined when the source strength is positive. When the source strength becomes negative, although the local velocity field does influence the mass inflow direction, the spatially variant mass source term dominates the overall mass inflow direction.

The mass source zone for this research is located up-wave relative to the CycWEC and has central points fixed at x_s = -10 m and y_s = -1.93 m based on the recommendations of [16], which fixed the central point based on water tank depth, desired wave height, and desired wavelength. These recommendations also outlined the suggested size of the mass source zone for deep ocean wave production. The mass source zone has a height of h_s = 1.45 m, and a width of w_s = 0.45 m, and generates the incident wave field, W_A. The submerged depth of the mass source upper surface is D_s = -1.205 m.

As noted in Section 2.3, minor variations can be noted in the generated wave field relative to analytical solutions because the mass source method is dependent on the size of the mass source zone and its position relative to the undisturbed free surface. Therefore the accurate implementation of the mass source term will be an iterative process [17].

3.3. CFD Domain Layout and Boundary Conditions

To model all the details of the rotating hydrofoils and the mass source region the computational model consists of four sub-domains. The first domain is an inner rotating domain that encompasses the hydrofoils and surrounding fluid. The second is a stationary outer domain that encompasses the free surface interface and extends to the outer boundaries. The third domain is a small stationary rectangular domain that contains the mass source region. Lastly, a small stationary domain was placed in the centre of the rotating domain for added simulation stability. The four sub-domains are connected using a general grid interface which allows the solution to be interpolated at each region interface without requiring one-to-one grid connections.

The six boundary conditions that were applied to the computational domain are shown in Figure 7. A no-slip wall was used on the surface of the hydrofoils and a free-slip wall was used on the domain's bottom surface. Openings with prescribed static pressure values were used at the left and right faces and an opening with entrainment was used on the top face to allow air to leave and enter the domain as necessary. To force the solution to be 2D, symmetry planes were used on all side faces. Note that during initial single hydrofoil testing, the mass source and second hydrofoil were completely removed from the domain.

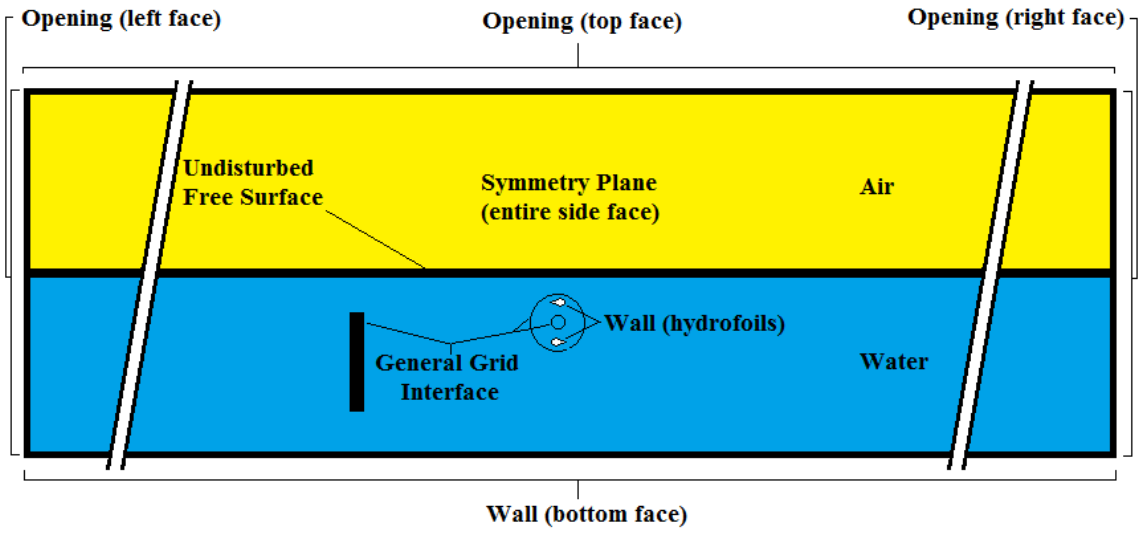

Figure 7 - Computational domain with applied boundary conditions.

3.4. Simulation Setup

The URANS simulations employed a transient solver based on a second order backward Euler transient scheme. Each transient simulation was run for up to 4800 time steps, or 60.24 seconds, which allowed for up to twenty-three and a half full hydrofoil rotations. Based on the findings of the time step study, presented in the next chapter, the simulations had a constant time step of Δt = 0.01255 seconds which was 1/200th of the rotational period of the hydrofoils. For added simulation stability the rotating hydrofoil was accelerated from rest linearly over the first 200 time steps, to a constant rotational speed of ω = 2.503 rad/s. The selected rotational speed resulted in a rotational period of T_{std} = 2.51 s and was chosen to match experimental parameters used while testing the 1:10 scale CycWEC model. Based on the device rotation radius and hydrofoil cord, this resulted in a Reynolds number of Re = 1.87×10^{6}. During the simulations the RMS residual target for *u* and *v*-momentum was defined as 10^{-5}. The maximum number of

coefficient loops per time step was set to 20, but convergence was typically achieved within 14 coefficient loops.

CHAPTER 4

4. GRID DESIGN

The required grid for URANS simulations was a specialized hybrid grid based on each unique simulation requirement. To test the wave generation and cancellation abilities of the CycWEC, and to design a numerical wave tank, different gridding approaches procedures were employed. The single hydrofoil and numerical wave tank grid design included in this chapter minimized the discretization error and computational requirements of the simulations, while a grid and time step sensitivity study is used to access the overall accuracy of the results.

4.1. Single-Hydrofoil Grid Design

In order to accurately capture the effects of a single rotating hydrofoil near a free surface, a hybrid grid consisting of structured and unstructured regions was designed. Images of the grid topology are shown in Figure 8. The grid consists of a structured inner region intended to capture the resulting flow field around the hydrofoil and wake. As

shown in Figure 8a), this structured inner region consists of body fixed C-grid around the hydrofoil. It also contained a secondary fine grid which was placed in the anticipated path of the generated wake. First node heights were set such that the maximum y+ was less than 1.5 on the hydrofoil surface. As shown in Figure 8b), a second structured grid at the free surface interface region is designed to effectively capture the interference of the hydrofoil and free surface, and to propagate the generated waves away from the device. It features an extremely fine structured grid extending twenty chord lengths in both the positive and negative *x*-directions, and was design specifically so that the free surface fluctuations resulting from the generated waves would not extend vertically beyond this region. Unstructured mesh was used to transition between the two regions efficiently.

As shown in Figure 8c), beginning at twenty chord lengths in the positive and negative *x*-directions, a numerical beach extending an additional sixty-six chord lengths in each direction was created. The grid spacing was systematically increased in both the *x* and *y* directions in the numerical beach to promote numerical dissipation, which prevented waves from reflecting off the outer boundaries back into the computational region of interest.

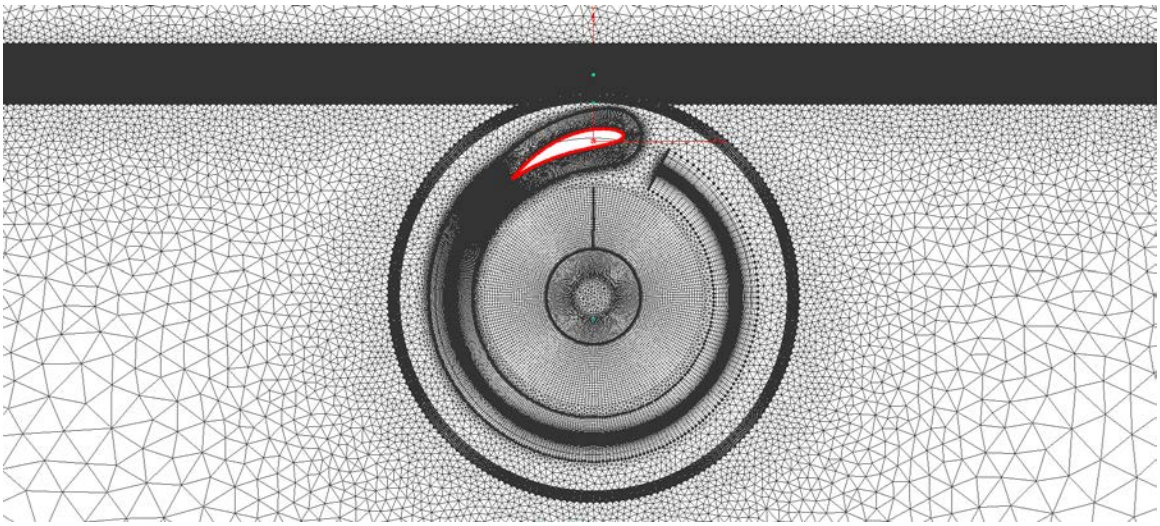

a)

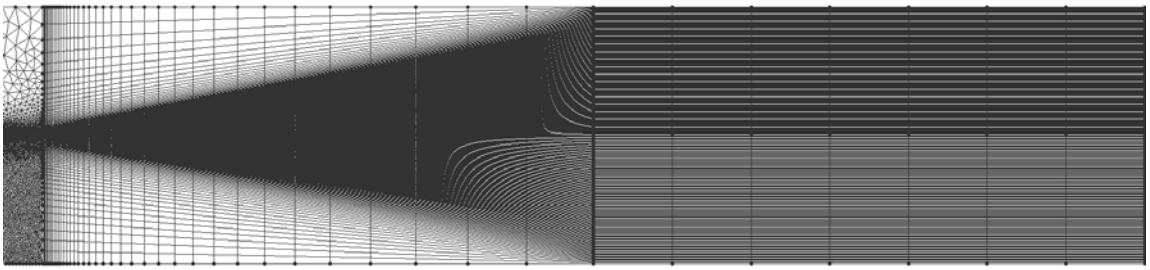

b)

Figure 8 - Hybrid mesh showing: a) wake and free surface capturing region and b) numerical beach region.

4.1.1. Grid Refinement Study

The primary objective of the grid refinement study was to ensure that the URANS simulations were spatially converged such that they reliably captured the interactions of the hydrofoil and free surface, while minimizing the required computational time by removing unnecessary mesh. The study was carried out at two pitch angles, specifically at $\alpha_1 = 0°$ and $\alpha_1 = 10°$. These pitch angles were chosen because at $\alpha_1 = 0°$ low amplitude waves will be generated, and thus wave propagation should be most difficult to model for this case. In contrast, at $\alpha_1 = 10°$ large amplitude waves will be generated and nonlinear

interactions of the hydrofoil and free surface will be most difficult to model for this case. Also, it will be more difficult to predict the flow around the hydrofoil at higher pitch angles.

It is important to note that the grid spacing was not reduced in the same proportions in all regions. This was because the spacing in the structured C-grid encompassing the hydrofoil and wake was optimized during initial simulations, so the grid density in those regions was held constant throughout study. Therefore the focus of the grid refinement study was on the free surface region as it contained up to 80% of the total elements while only making up 0.4% of the total domain area.

A course, medium and fine mesh was created for each pitch angle. Mesh statistics for the free surface region are summarized in Table 1 for $\alpha_1 = 0°$ and in Table 2 for $\alpha_1 = 10°$. Also shown in each table is the total number of grid elements in the entire domain. The number of nodes in the free surface region is summarized as ratios of λ_1, λ_2, H_1, and H_2, which are the wavelengths and the amplitude of the generated fundamental and 1st harmonic waves propagating in the down-wave direction. Note that H_1, and H_2 are based on predicted values using the medium mesh.

Table 1 - Meshing statistics of free surface region for $\alpha_1 = 0°$.

Meshing Statistics for α = 0°					
Mesh Type	$\frac{Nodes}{\lambda_1}$	$\frac{Nodes}{\lambda_2}$	$\frac{Nodes}{H_1}$	$\frac{Nodes}{H_2}$	Total # of Elements
Coarse	123	31	7	8	133378
Medium	246	62	13	16	266140
Fine	492	123	27	31	756253

Table 2 - Meshing statistics of free surface region for α_1 = 10°.

Meshing Statistics for α = 10°					
Mesh Type	$\frac{Nodes}{\lambda_1}$	$\frac{Nodes}{\lambda_2}$	$\frac{Nodes}{H_1}$	$\frac{Nodes}{H_2}$	Total # of Elements
Coarse	123	31	44	25	134186
Medium	246	62	88	50	264440
Fine	492	123	175	101	759529

Predicted free surface elevations as a function of time are shown in Figure 9 for a constant axial location of x = 8 m. Results are shown for each mesh at both pitch angles. Note that free surface elevation is normalized by the hydrofoil chord and time is normalized by the period of the rotating hydrofoil, T_{std}. In general, the predicted free surface topology was similar for all three meshes at both α_1 = 0° and α_1 = 10°. However, minor differences in predicted free surface elevations did occur for all cases at both pitch angles. It is important to note that at α_1 = 0°, the coarse mesh often predicted the largest free surface variation, but this was a result of the linear interpolation process used to determine the location of the free surface. As shown in Table 1, there were less than 10 nodes to capture the peak-to-peak wave height of both the fundamental and 1st harmonic waves for this case.

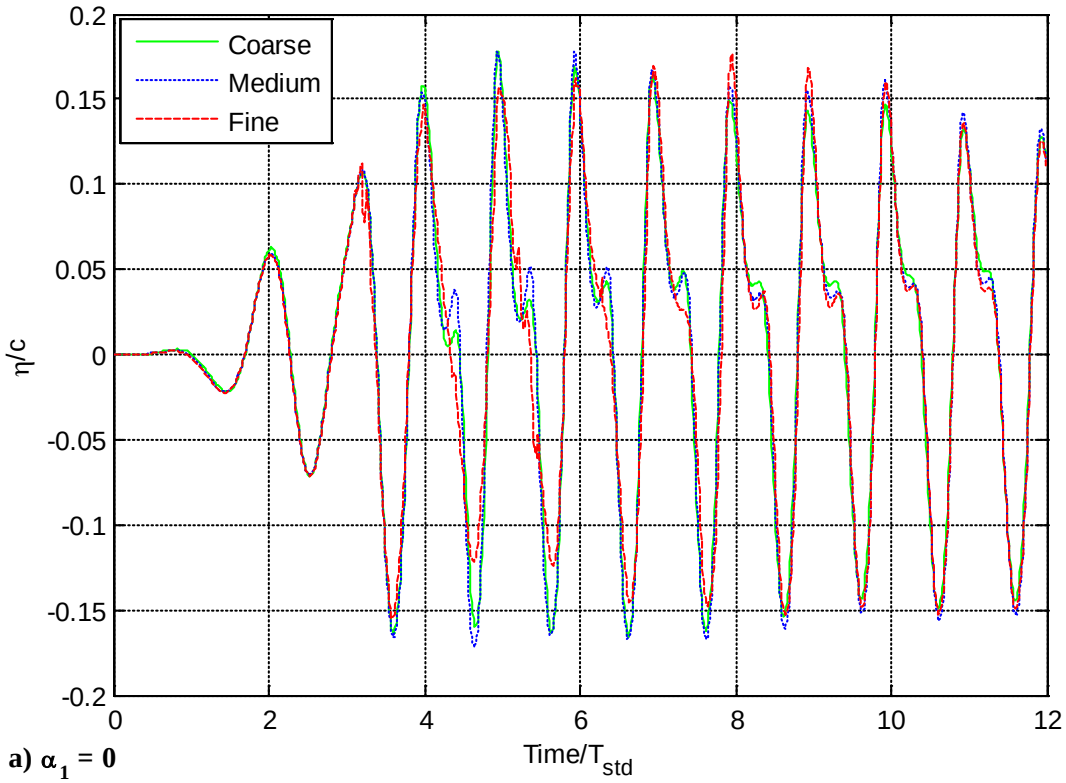

a) α_1 = 0

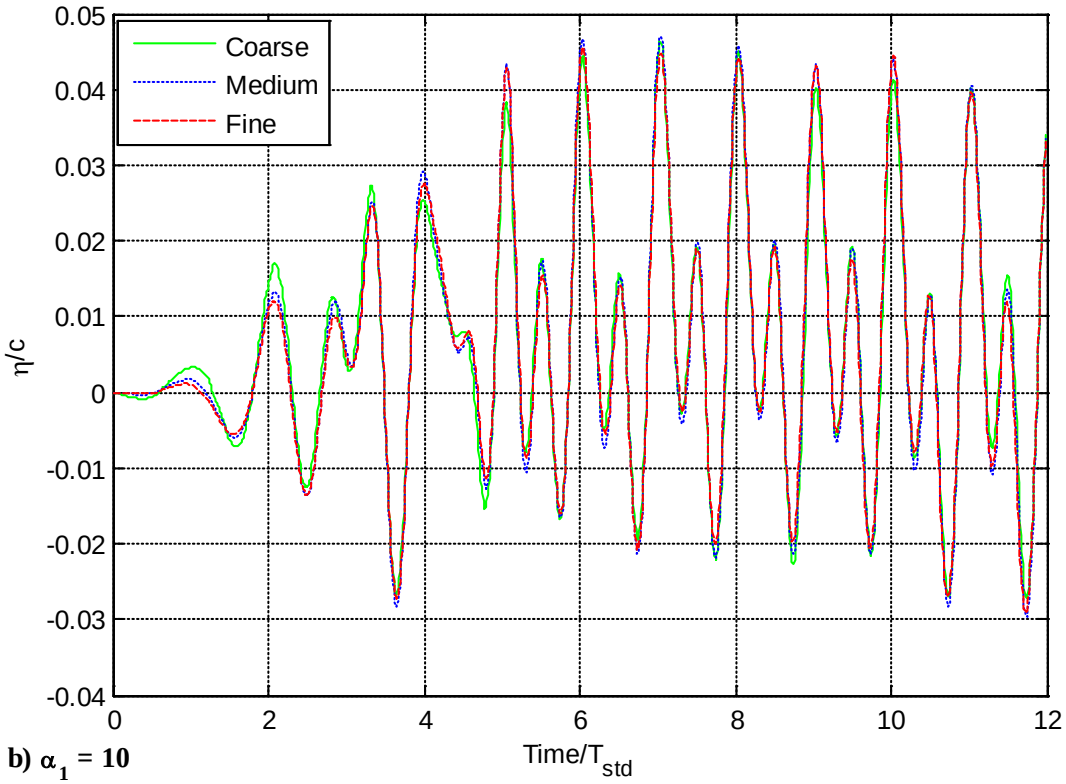

b) α_1 = 10

Figure 9 - Free surface variation 8 meters from origin in the *x*-direction.

To analyse the amplitude and frequency of the wave components contained in the generated wave train a Fast-Fourier Transform (FFT) was applied to the time series of free surface elevation data shown in Figure 9. The free surface elevation data was sampled at a frequency of $1/\Delta t$ for 15.06 seconds which spanned over the last 600 time steps, or 6 revolutions, of the simulations to ensure that any initial transients were removed. The applied FFT produced 300 independent complex numbers each having a unique frequency of up to half the sampling frequency [25]. The 300 frequencies are the frequencies of all the detected generated wave components. The absolute value of the complex numbers produced the amplitude of the wave components, which when doubled and normalized by the hydrofoil chord length produced the non-dimensional wave height, H/c, as shown in Figure 10. The period of each wave component, T, is found through its corresponding frequency and is normalized by the rotational period of the hydrofoil. Each wave component phase angle is calculated as the inverse tangent of the quotient of the imaginary and real part of its complex number. The resulting FFT plot for the waves generated x = 8 m from the origin are shown in Figure 10 for all three mesh densities at both pitch angles. For both pitch angles the FFT analysis revealed that the generated wave train is composed of the fundamental wave, W_1, whose period is equal to T_{std}, and the first three harmonics, W_2, W_3, and W_4, with periods equal to $T_{std}/2$, $T_{std}/3$, and $T_{std}/4$, respectively. The medium and fine grids were able to accurately capture W_3 and W_4, but this was not the case for the coarse grid.

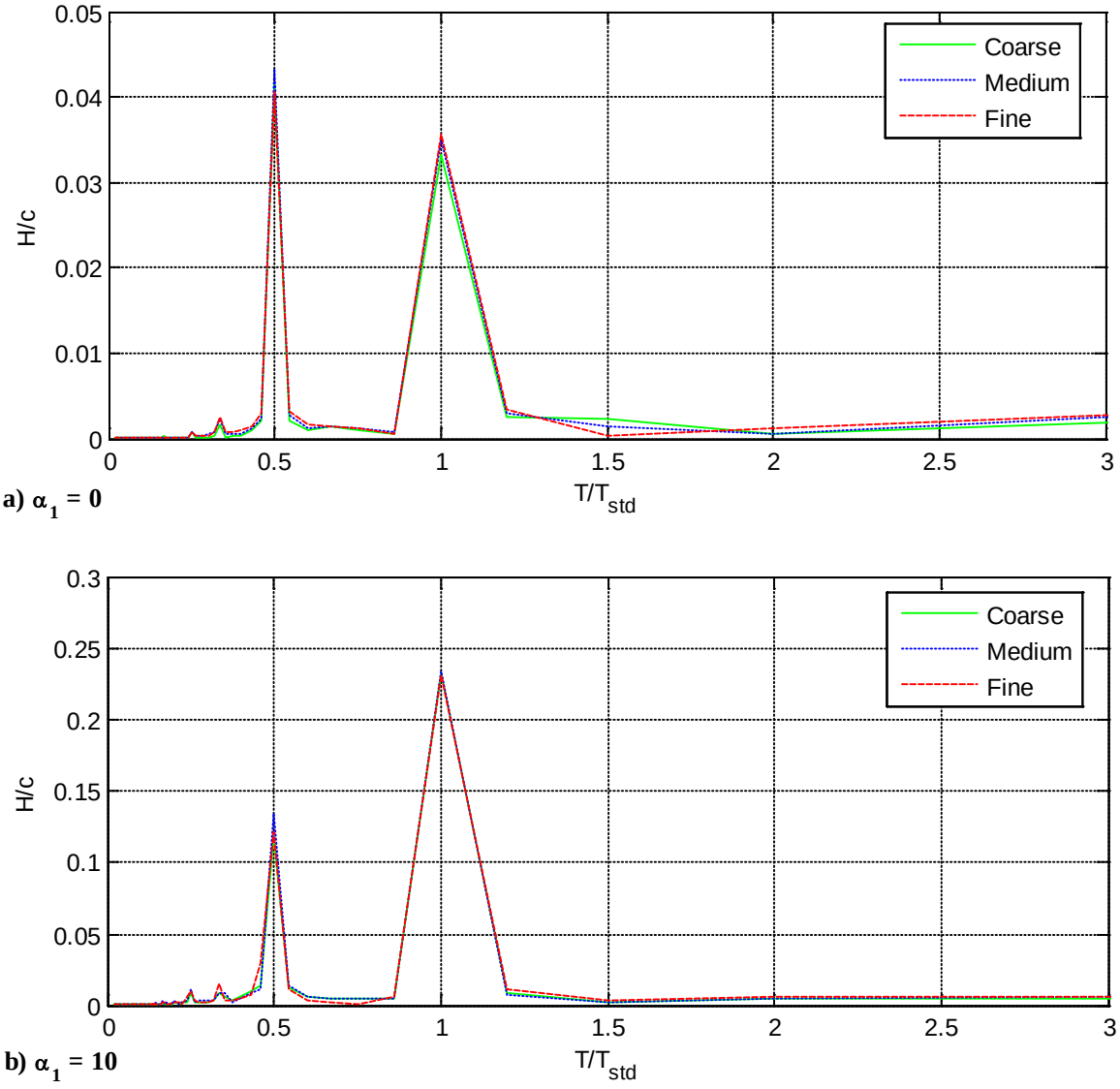

Figure 10 - FFT analysis of free surface variation 8 meters from origin in the *x*-direction.

To determine the variation of the fundamental and 1st harmonic wave heights predicted by the FFT analysis, wave heights are plotted in Figure 11 as a function of vertical grid density for both pitch angles. To highlight the variation of wave heights as the generated wave train propagates in the down-wave direction, results are shown at x = 4, 6, 8, 10 and 12 m from the origin. For α_1 = 0º the variation of wave height is more significant between the coarse and medium grids compared to the difference between the

medium and fine grids. In particular, the average variation of H_1 between the medium and fine density grids was 1.53% at the four locations investigated, while H_2 varied an average of 3.47%. In comparison, the average variations of H_1 and H_2 between the coarse and fine grids were 7.23% and 4.17%, respectively.

For $\alpha_1 = 10^o$ the variation in wave height between the coarse and medium grids were comparable to that between the medium and fine grids. In particular, the fundamental wave height varied on average by 1.87% between the medium and fine grids, and 2.30% between the coarse and fine grids, at the four locations investigated, while H_2 varied and average of 5.49% between the medium and fine grids, and 3.91% between the coarse and fine grids. It is interesting to note that the variation of H_2 was similar at $\alpha_1 = 0^o$ and 10^o even though its magnitude was significantly greater at $\alpha_1 = 10^o$, which, as shown in Tables 1 and 2, resulted in significantly more nodes per waves height.

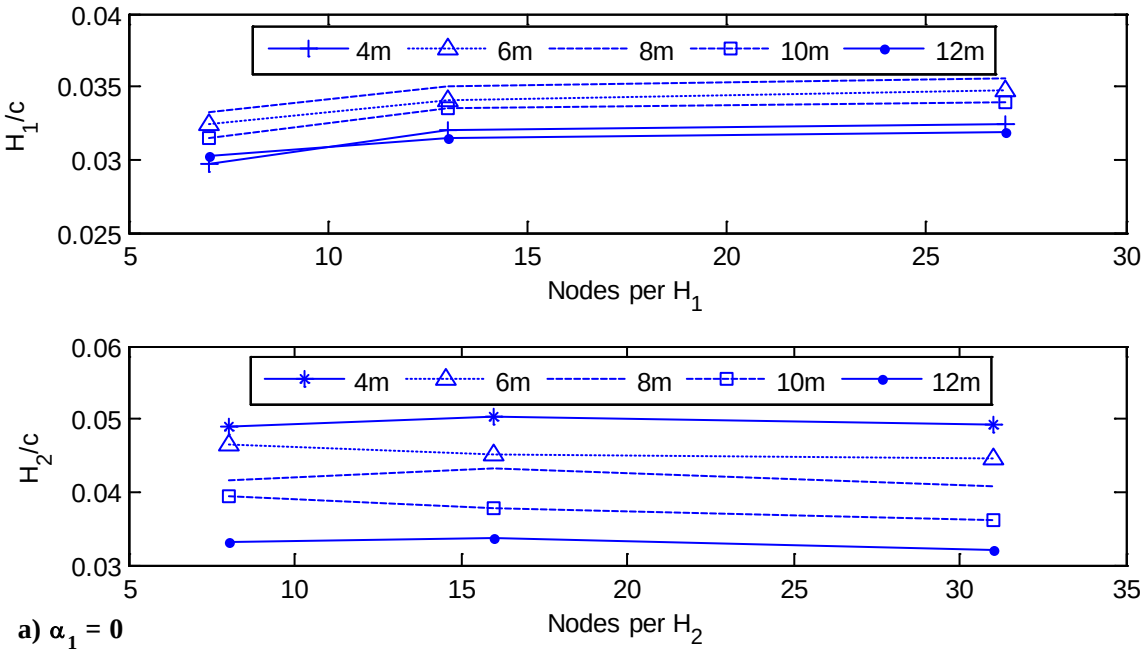

Figure 11 - Primary and secondary wave height as function of mesh size at 4, 6, 8, 10 and 12 meters away from the origin in the *x*-direction.

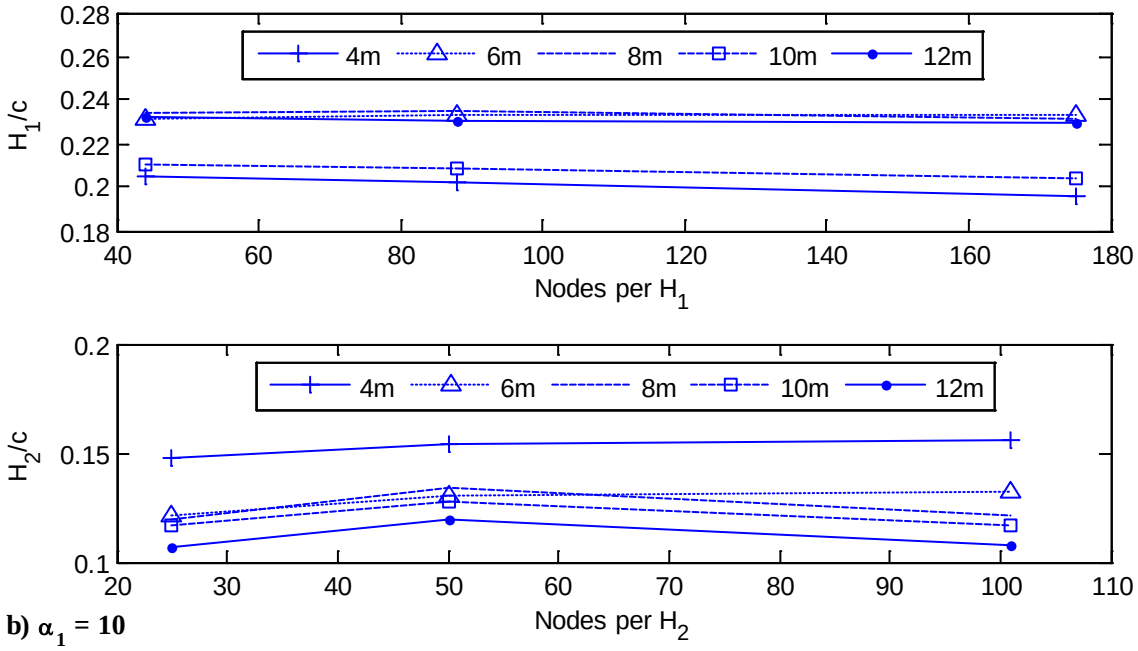

b) α_1 = 10

Figure 11 - Continued.

To determine if a grid independent solution was obtained in the inner region encompassing the hydrofoil and wake, resulting unsteady hydrodynamics forces were determined for all three grids at α_1 = 0° and α_1 = 10°. Although the structured grid properties directly surrounding the hydrofoil and wake region were held constant, the remainder of the unstructured mesh in the rotating domain changed proportionally to the variation of Δx and Δy applied in the free surface region. Total X and Y forces were outputted at each time step relative to a body-fixed coordinate system shown in Figure 5. Force coefficients, C_T and C_R are plotted in Figure 12 for all three grid densities, where C_T is the component of hydrodynamic force in the x-axis direction and C_R is the component in the positive Y-axis direction. Force per unit width is normalized by the chord length, c, and $(1/2)\rho(\omega R)^2$. For the results shown in Figure 12 the hydrofoil is assumed to be neutrally buoyant, and thus any fluctuation in the forces must result from the interaction of the hydrofoil with the free surface or its own wake. For the α_1 = 0° case,

the force predictions by the coarse mesh had an RMS difference from the fine mesh predictions of 8.14×10^{-3} and 6.20×10^{-4} for C_R and C_T, respectively, while the RMS difference of the medium mesh was 3.29×10^{-3} and 2.91×10^{-4}. For the $\alpha_1 = 10°$ case, the coarse mesh had an RMS difference from the fine mesh predictions of 1.07×10^{-2} and 1.91×10^{-3} for C_R and C_T respectively, while the RMS difference of the medium mesh was 2.25×10^{-3} and 5.50×10^{-4}. This suggests that the coarse mesh is incapable of accurately predicting the near body flow around the hydrofoil and resulting wake.

Figure 12 also provided the opportunity to investigate the effect of the free surface on the resulting body forces. At $\alpha_1 = 0°$, C_T was found to fluctuate between 0 and -0.005, while C_R varied between -0.0075 and -0.062 for the medium and high density grids. At $\alpha_1 = 10°$, C_T was found to fluctuate between values of 0 and -0.015, while C_R varied between 0.284 and 0.451. Note that at $\alpha_1 = 0°$, C_R was negative but at $\alpha_1 = 10°$, C_R was positive and ten times larger in magnitude. This correlates well with the wave amplitudes shown in Figure 10 because the radial force is linearly related to the bound circulation through the Kutta-Joukowski theorem and it was shown in [12] that the bound circulation and wave amplitude are also linearly related.

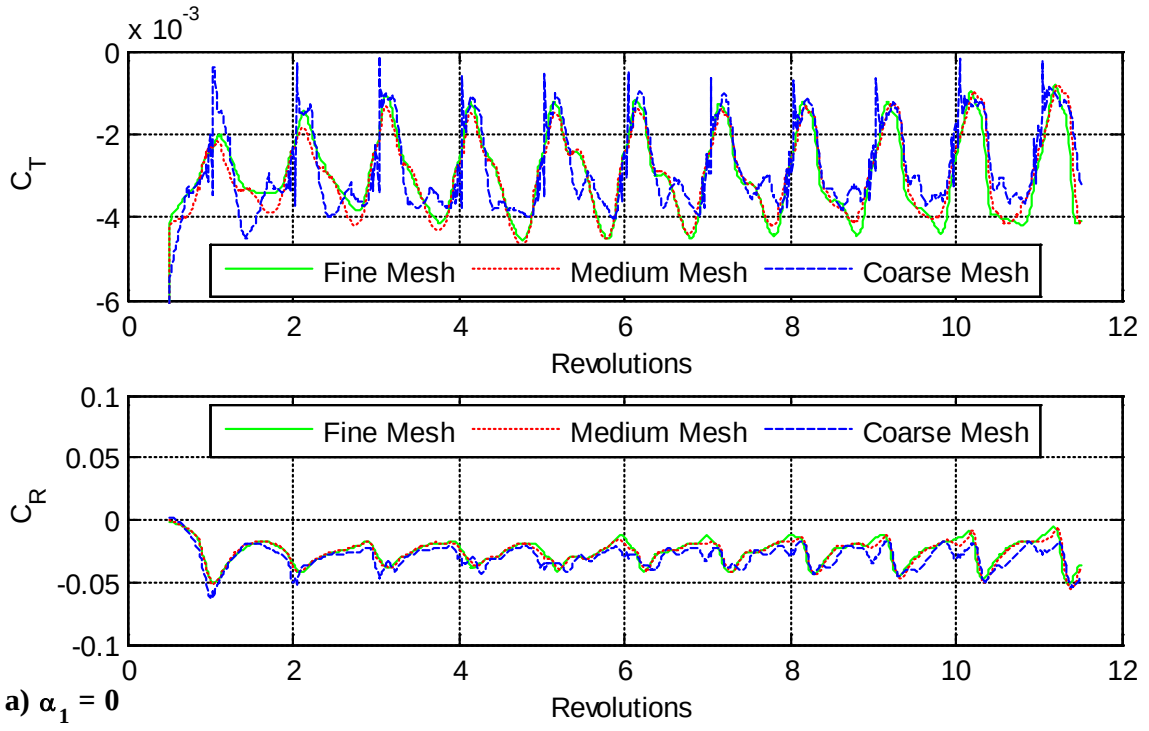

a) $\alpha_1 = 0$

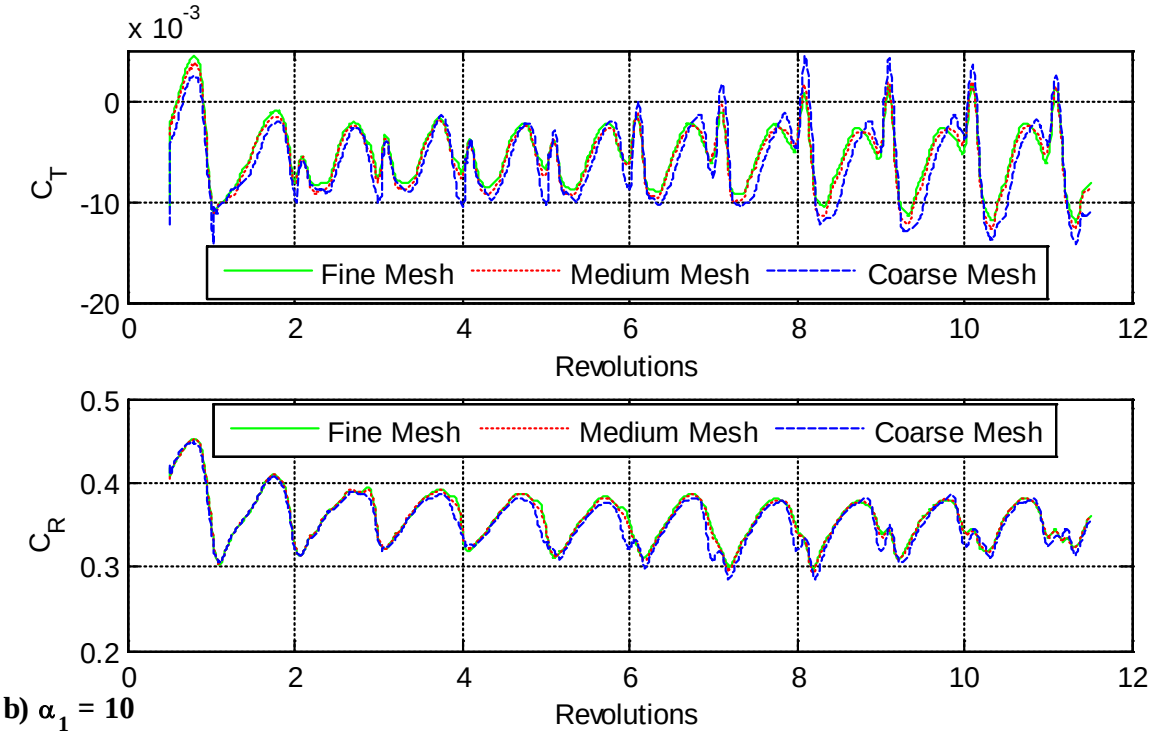

b) $\alpha_1 = 10$

Figure 12 - Hydrofoil body-fixed force coefficients throughout each revolution for three different mesh densities.

4.1.2. Time Step Study

To ensure that the solution is not only grid independent but also independent of time step size, a time step study was completed. In this study, the time step sizes were Δt = 0.01255, 0.0251, and 0.0502 seconds, which were equal to $T_{std}/200$, $T_{std}/100$, and $T_{std}/50$, respectively. The simulation with the smallest time step size needed 2400 time steps to achieve a total simulation time of 30.12 seconds, while the medium and large time step simulations needed 1200 and 600 time steps respectively.

The study evaluated the abilities of the numerical solver to accurately model the generated wave field with different time step sizes. The findings of the study, shown in Figure 13 and Figure 14, suggest that the solutions generated for these three time steps were not identical. The free surface plot shows that the simulation with the largest time step size predicts much smaller free surface fluctuations compared to the medium and small time step size simulations. An FFT was applied to the free surface fluctuations which required varying sampling rates based on time step size but a constant time interval of 15.06 seconds was used for all simulations. For the largest time step the wave heights summarized in Figure 14 show an 8.02% decrease in the fundamental wave height and a 42.82% decrease in the first harmonic wave height compared to the medium time step simulation. Reducing the time step by a factor of 2 to the smallest size of 0.01255 seconds caused the fundamental wave height to increase by 4.55% and the first harmonic wave height to grow by 18.59%. These results suggest the use of the smallest time step size, or one even smaller is required to achieve a truly time step size independent solution.

The required use of the smallest time step was further confirmed upon analysis on the correlation between time step size and resulting wave heights. Figure 15 shows the results of single hydrofoil simulations completed at ten other pitch angles. The fundamental wave heights were found to increase by an average of 2.86% when the smaller time step was used. A greater difference, however, was noted for the first harmonic wave height, as simulations with the smaller time step size resulted in the first harmonic wave height increasing by an average of 19.17%.

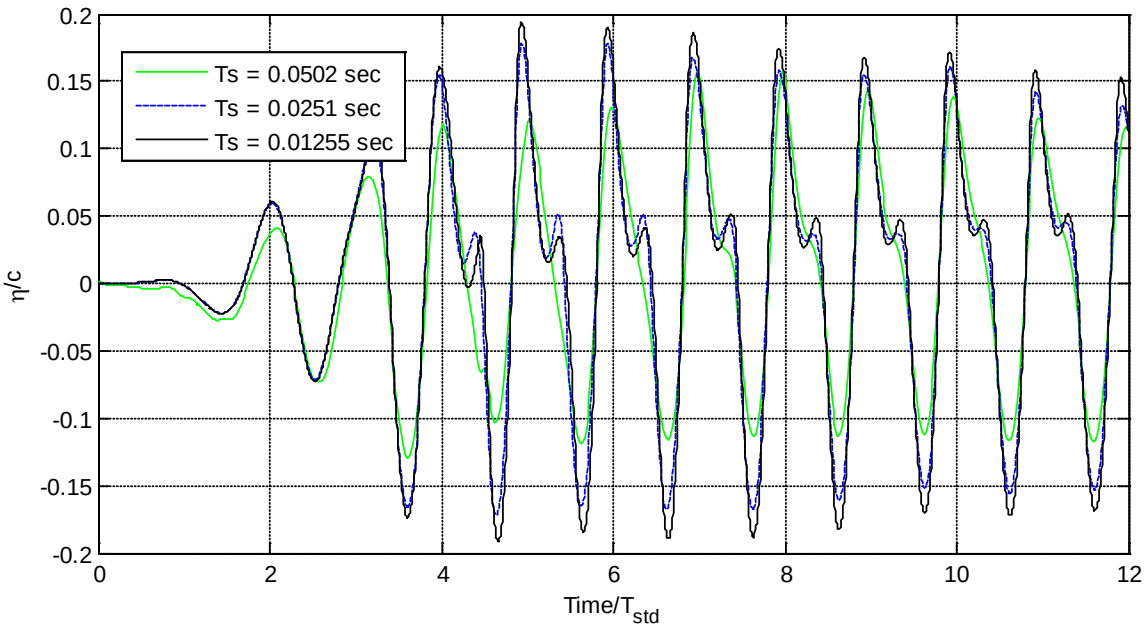

Figure 13 - Free surface variation 8 m from origin in the x-direction showing effects of time step size.

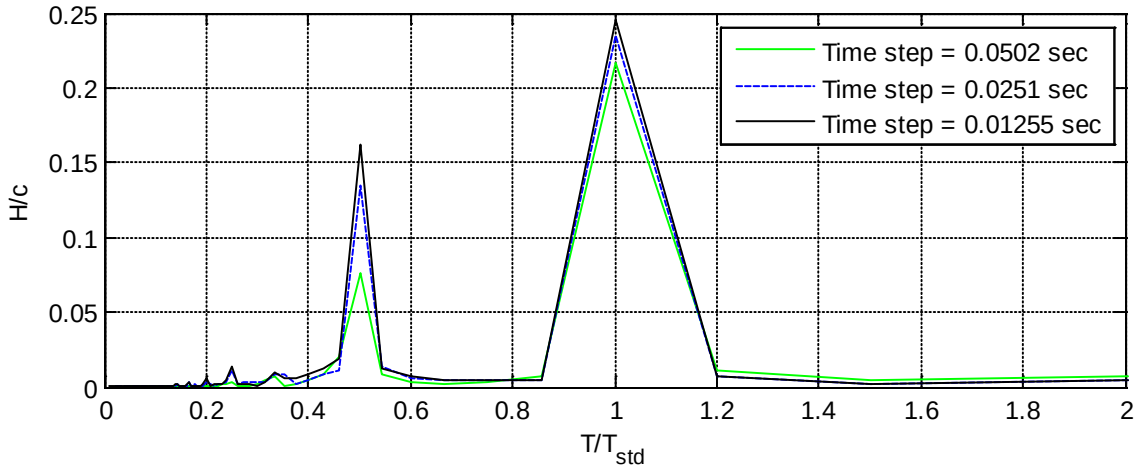

Figure 14 - FFT analysis of free surface variation 8 m from origin in the x-direction showing effects of time step size.

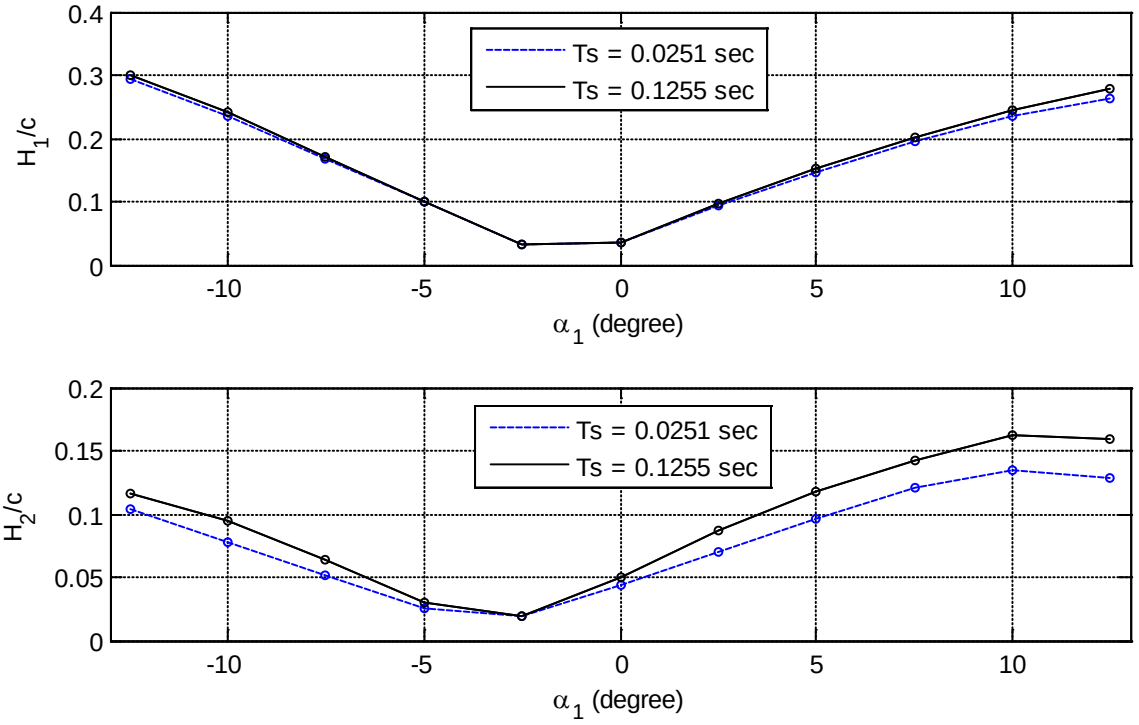

Figure 15 - Primary and secondary wave heights as function of hydrofoil pitch angle for two different time step sizes.

4.2. Mass Source Region Grid Design

To model the waves generated from the mass source term the hybrid mesh used for the single hydrofoil simulations was modified to meet several specific criteria. The circular wake capturing region that contained the hydrofoil was removed and replaced with structured grid in the free surface capturing region and unstructured grid elsewhere. The mass source region was added thirteen chord lengths in the up-wave direction relative to the original position of the hydrofoil as shown in Figure 16. The mass source region has horizontal and vertical grid spacing values of Δx = 0.0375 m and Δy = 0.0320 m, respectively, based on the specifications outlined in [17], which defined required horizontal and vertical grid spacing for numerical wave generation using a mass source term based on the wavelength and wave height of the generated wave. To generate an incident wave train of desired amplitude and period the mass source strength within the region was defined according to equation (18).

To evaluate the performance of the mass source term, several parameters were initially studied independently. Specifically, the grid density in the region occupied with water and time step size was altered and their impact on the generated wave field was investigated. The ability of the mass source term to effectively model wave phase shifts was also tested and the results are included in this section.

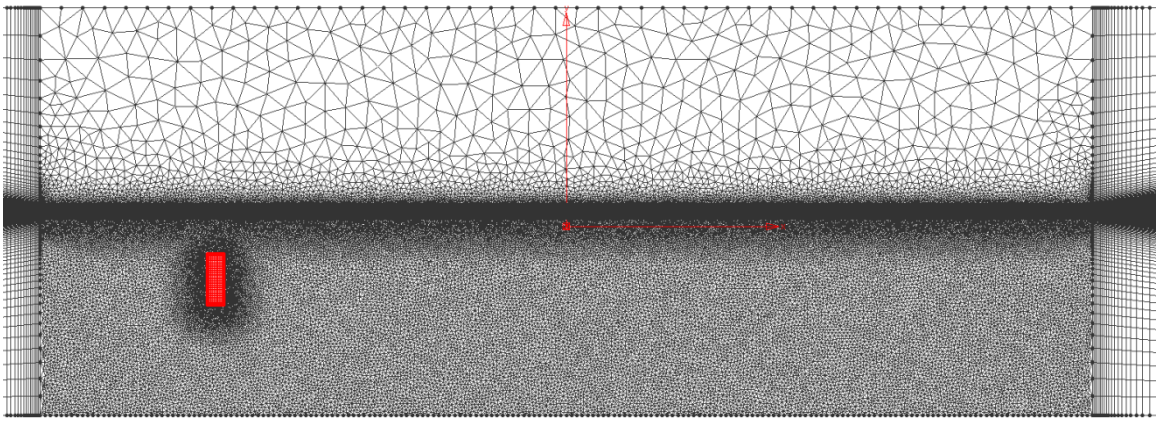

Figure 16 - Hybrid mesh showing the placement of the mass source region in the domain of interest

4.2.1. Grid Resolution in Water Region

The single hydrofoil simulations completed during the time and grid size studies showed that outside the far field region, the solver had a quantifiable damping effect on the wave amplitudes. This resulted in a spatial decrease in wave height as the wave propagated from the hydrofoil. Using the finest grid tested and a pitch angle of $\alpha_1 = 10^o$, H_1/c decreased by as much as 2.684×10^{-3} or 2% per meter down-wave.

In an effort to minimize the spatial damping of the waves as they propagate away from their source the medium density grid was used however the concentration of the unstructured grid below the free surface was increased for the numerical wave tank simulations. By decreasing the maximum grid size by 80% and increasing the boundary decay from the default value of 0.5 to 0.99, the number of unstructured elements in the water region increased by 600% from 1.2×10^4 elements to 7.2×10^4 elements.

To test the impact of the refined grid in water, the resulting incident wave height, H_A/c, generated from the mass source term located at x = -10 m was determined for the coarse and fine grids shown in Figure 17. For the fine grid, H_A/c was found to decrease by 6.665 x 10^{-4} per meter down-wave, representing a 75.2% reduction in wave height dissipation per meter compared to the coarse grid solution, supporting the inclusion of the additional mesh elements for all future simulations.

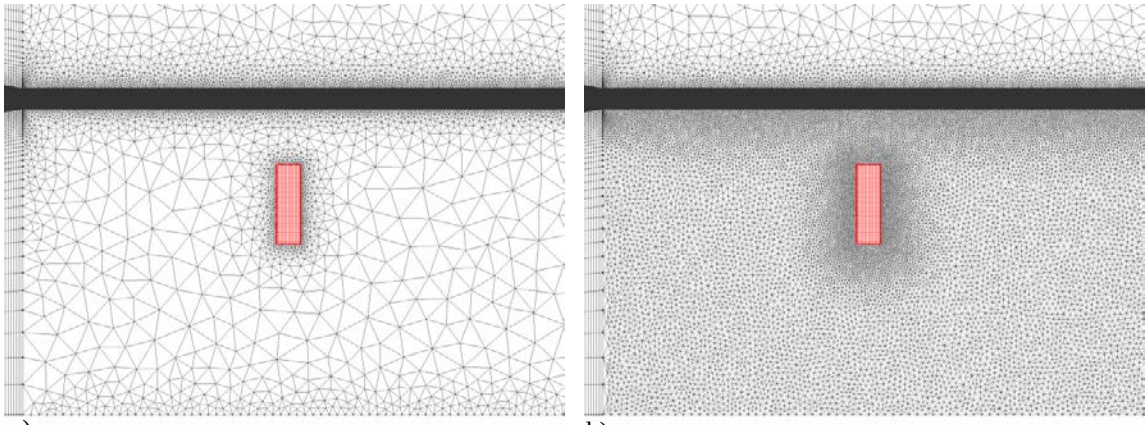

a) b)

Figure 17 - Hybrid mesh a) initial coarse grid in water region, b) fine grid in water region.

4.2.2. Time Step Study

To verify that the generated incident wave field is independent of time step size, a time step study was once again completed. In this study, the time step sizes were Δt = 0.01255 and 0.0251 seconds, which were equal to $T_{std}/200$ and $T_{std}/100$. The simulations needed 2400 and 1200 time steps, respectively, to achieve a total simulation time of 30.12 seconds.

The purpose of this study was to evaluate the performance of the mass source term with different time step sizes. The findings of the study, shown in Figure 18, suggest that

the waves generated for these two time steps are similar but do have quantifiable differences. It was determined that the simulation using the smaller time step size had a wave height 3.8% larger than the simulation that used the larger time step. These findings agree with the findings of the time step study performed during the single hydrofoil wave generation phase, summarized in section 4.1.2 of this report, which concluded that Δt = 0.01255 seconds, or $T_{std}/200$, was required for all simulations moving forward.

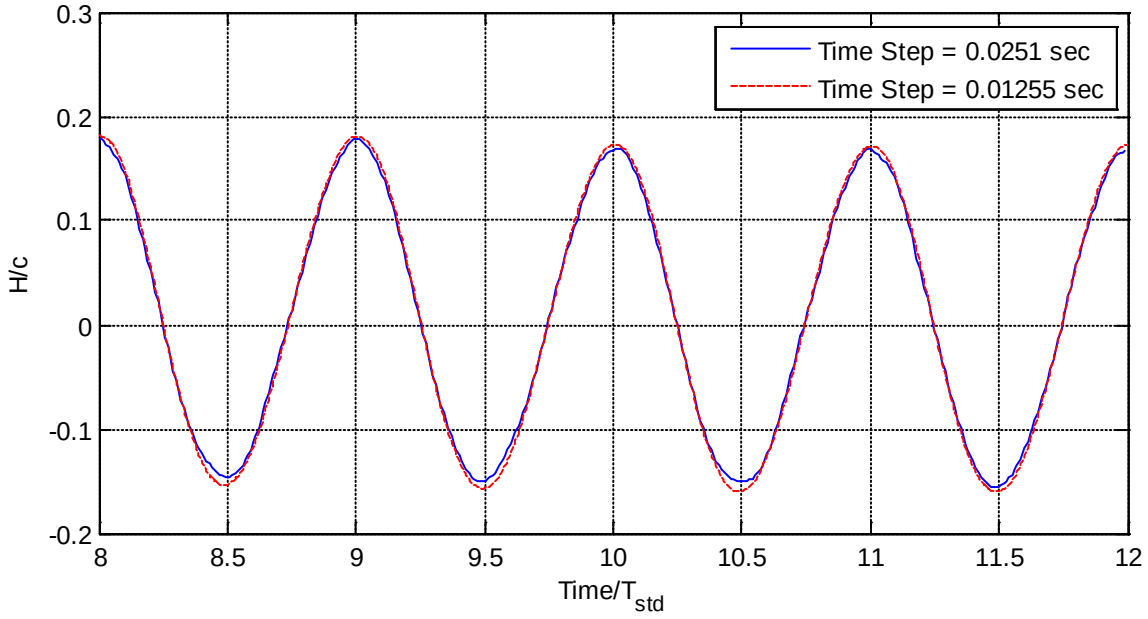

Figure 18 - Free surface topology measured at x = 0 m generated by mass source term showing effects of time step size.

4.2.3. Phase Angle Study

The final parameter that was studied while designing the mass source zone was the ability of the mass source to effectively model an incident wave field phase shift, ψ_A, as defined by the user. Initially, a wave field was generated with an incident wave height of H_A/c = 33.39 and phase shift of ψ_A = 0°. The resulting free surface topology at x = 0 m is

defined by the dashed red line in Figure 19. A second wave field was then generated with the identical incident wave height, but with a phase shift of ψ_A = -60°. The resulting generated wave field was added to Figure 19 to displays the effects of adding a positive phase shift to the mass source term input. Upon closer inspection it was determined the generated wave field had an actual phase shift of -59.8°. With a difference of only 0.2° it was confirmed that the mass source term can accurately model phase shifts as defined by the user.

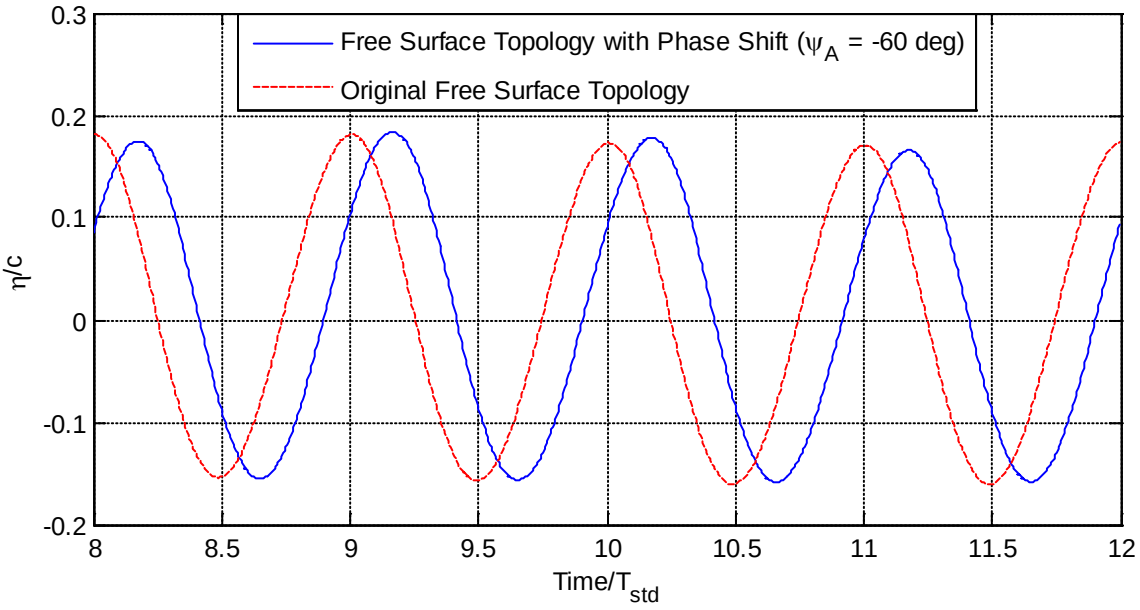

Figure 19 - Free surface topology at *x* = 0 m generated by mass source term showing accuracy of a user defined phase shift.

4.3. Two-Hydrofoil Grid Design

To accurately capture the effects of a two-hydrofoil CycWEC model operating near a free surface, a hybrid grid was constructed. The grid design was based on the single

hydrofoil grid design and grid refinement study, while also incorporating the required refined unstructured grid below the free surface, as detailed in section 4.2.1.

The hybrid grid consists of a structured inner region intended to capture the flow field around the hydrofoil and wake. The structured inner region has a body fixed C-grid around the each hydrofoil as shown in Figure 20. It also contains one supplementary fine grid per hydrofoil which is placed in the anticipated path of its generated wake. Parameters for grid resolution in this region were chosen based on the results of the single hydrofoil grid refinement study.

The resolution of the free surface region was also chosen based on the findings of the single hydrofoil grid refinement study, which concluded that the medium density grid was optimal. In addition, the resolution of the unstructured region below the free surface capturing region was also increased based on the results of the numerical wave maker grid refinement study. This permitted the two-hydrofoil grid design to effectively capture the interaction of the hydrofoils and the free surface, and to propagate the generated waves away from the device. The free surface capturing region features extremely fine grid extending twenty chord lengths away from the device in both directions. This structured grid region was extended vertically as large free surface fluctuations were anticipated from the two-hydrofoil model and having the free surface exit the free surface capturing region was not desired.

The two-hydrofoil grid design featured a total of 380 000 elements for wave generation simulations with hydrofoil pitch angles of α_1 = 7.5° and α_2 = -7.5°, and α_1 = 5° and α_2 = -5°. For hydrofoil pitch angles of α_1 = 10° and α_2 = -10°, and α_1 = 12.5° and α_2 =

-12.5°, the final grid required 420 000 elements due to the extended free surface capturing region needed as a result of the larger wave heights of the generated wave field.

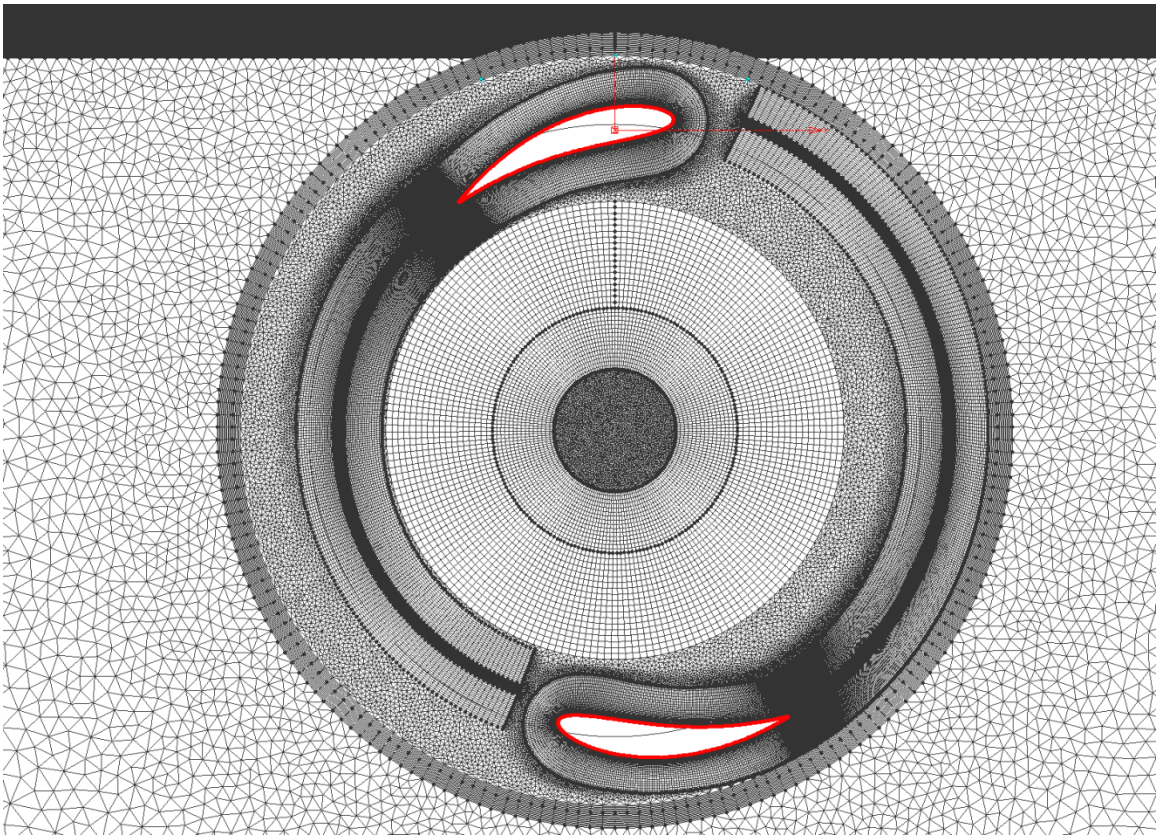

Figure 20 - Hybrid grid showing wake capturing region for two-hydrofoil model.

4.4. Final Grid Design

To design the grid used to test the two-dimensional wave cancelation abilities of the two-hydrofoil CycWEC model, aspects from the single and double-hydrofoil grid designs along with features from the mass source zone grid design were all incorporated into one final grid. The CFD domain included a mass source zone, two-hydrofoil wake capturing regions, a refined unstructured grid below the free surface capturing region, and the medium density resolution within the free surface capturing region. The position of the

mass source zone relative to the two-hydrofoil device, within the domain, is shown in Figure 21.

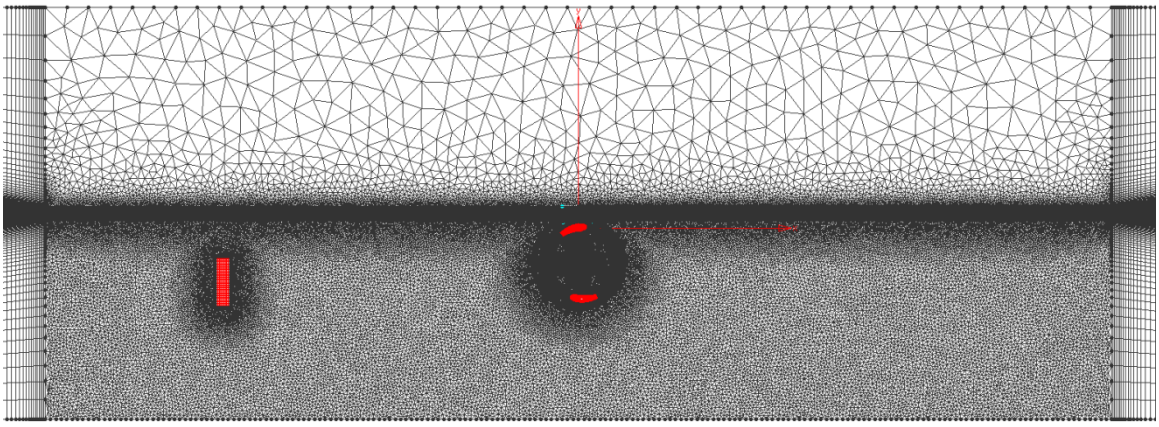

Figure 21 - General view of CFD domain for hybrid grid designed to test wave cancellation abilities of two-hydrofoil CycWEC model.

Similar to the two-hydrofoil grid design, the final grid design also featured a total of 380 000 elements for wave cancellation simulations that had hydrofoil pitch angles of α_1 = 7.5° and α_2 = -7.5°, and α_1 = 5° and α_2 = -5°. For hydrofoil pitch angles of α_1 = 10° and α_2 = -10°, and α_1 = 12.5° and α_2 = -12.5°, the final grid required 420 000 elements due to the extended free surface capturing region needed as a result of the larger wave heights of the incident wave field. Figure 22 provides a more detailed view of the grid designed to incorporate numerical wave generation through the mass source term and wave cancellation by the two-hydrofoil model. The progression of the grid from its basic form during initial stages of the single hydrofoil research to its current final form has seen major improvement in the overall accuracy and computational efficiency of the simulations.

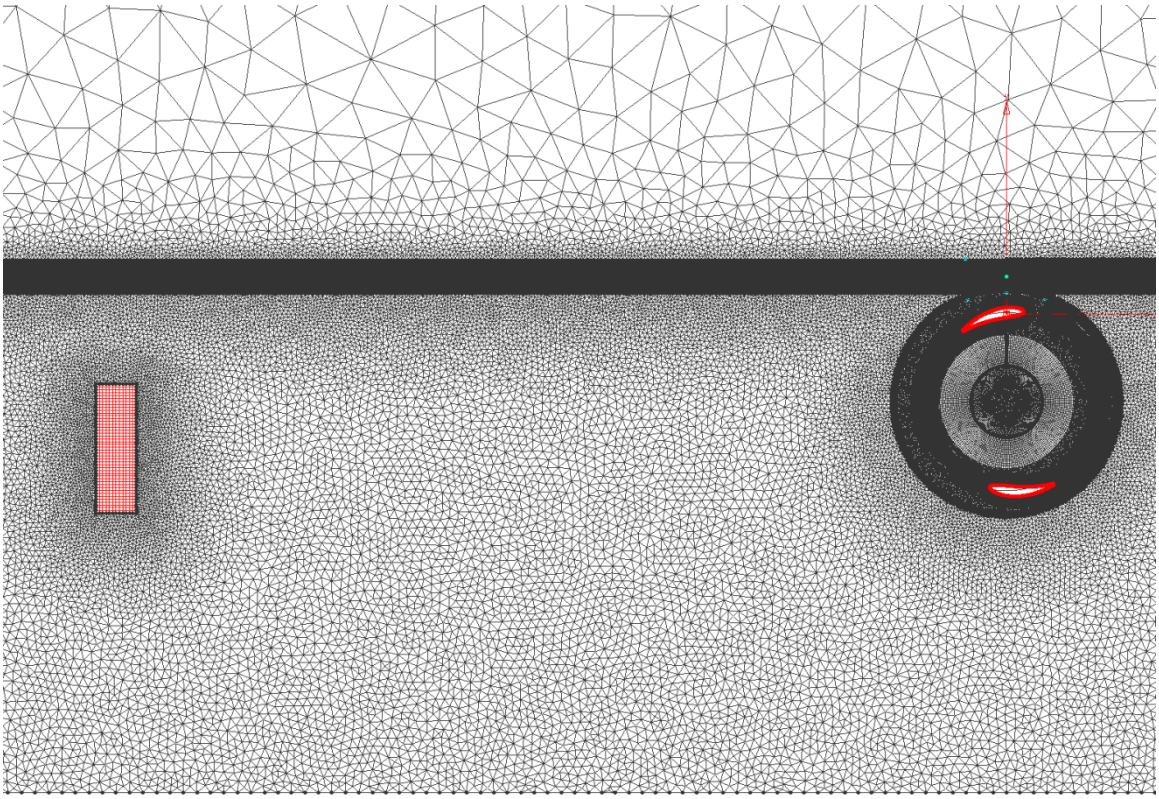

Figure 22 - Detailed view of the domain of interest for the hybrid grid designed to test wave cancellation abilities of the two-hydrofoil CycWEC models.

CHAPTER 5

5. SINGLE HYDROFOIL WAVE GENERATION RESULTS

In this chapter preliminary CFD simulations of the two-dimensional wave generation capabilities of the single hydrofoil CycWEC model, along with the performance of the numerical wave tank, are presented. A fundamental property of an ideal wave terminating device, such as the CycWEC studied in this research, is the generation of a one-sided wave field travelling in the down-wave direction that can interfere destructively with the incident wave field. Thus, wave generation simulations allow the wave cancellation potential of such a device to be inferred. The performance of the numerical wave tank is compared to linear wave theory. The evaluation of both simulations concerns the resulting free surface topologies and the development of complex velocity fields in both the near and far field regions.

5.1. Single Hydrofoil Wave Generation

URANS predictions of the generated waves resulting from a single hydrofoil rotating near a free surface are contained in this section for pitch angles of α_1 = ±5°, ±7.5°, ±10°, and ±12.5°. Based on the findings of the grid refinement and time step studies, a constant medium sized mesh and Δt = 0.01255 seconds was used for all eight simulations. Predicted free surface variation, primary and secondary wave heights, surface pressure distributions, and resulting forces are examined as a function of α_1.

5.1.1. Characteristics of the Generated Wave Field

To visualize the flow topology resulting from the rotating hydrofoil, contours of velocity in a stationary frame are plotted in Figure 23 at an instant in time near the end of the twelfth revolution for α_1 = -10° and α_1 = 10°. These figures capture the velocity field when the hydrofoil circumferential position is θ = 19.4° (i.e., near the top of the rotation), where the interaction with the free surface is strongest. The velocity contours demonstrate that the radial variation of the hydrofoil's trailing edge between α_1 = -10° and α_1 = 10° also results in a significant variation of the hydrofoil wake location. It can be seen that the radial position of the wake for α_1 = -10° is near the path of the leading edge for the negatively pitched hydrofoil, which was not the case for the positive pitch angle. Also note that when α_1 = -10° the hydrofoil pushes the free surface up as it passes underneath, and when α_1 = 10° the hydrofoil pulls the free surface downward as it passes underneath. The impact of this difference will be noted when analysing the free surface variation.

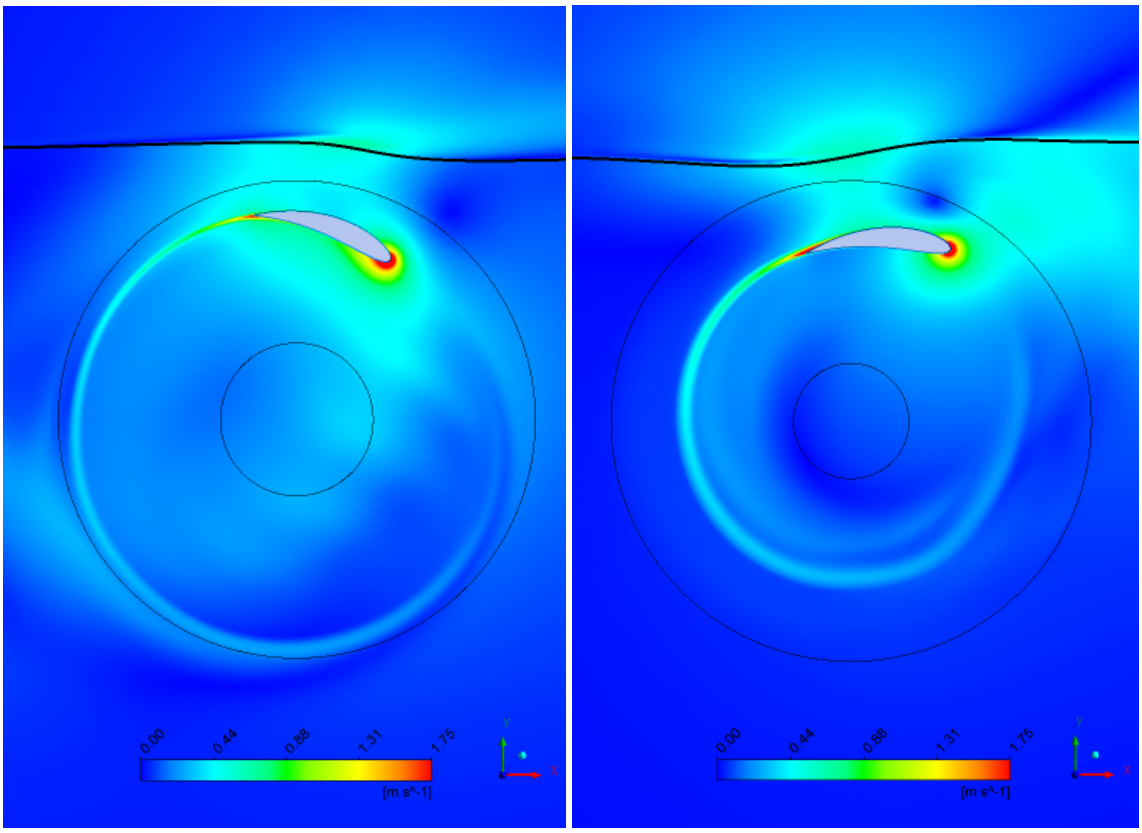

a) α_1 **= -10°** **b)** α_1 **= 10°**

Figure 23 - Velocity in stationary frame during the twelfth rotation. The free surface is also shown as a solid black line.

The temporal free surface variation resulting from the generated wave field at x = 8 m is shown in Figure 24 a) and b) for pitch angles of α_1 = 5°, 7.5°, 10°, 12.5° and in Figure 25 a) and b) for pitch angles of α_1 = -12.5°, -10°, -7.5°, -5°. The free surface variations agree with the findings of [11], which concluded that a rotating hydrofoil generates a one-sided wave field travelling in the down-wave direction that is composed of several waves with different frequencies and amplitudes. As shown in Figure 24 and Figure 25, significant waves travelling in the down-wave direction were generated at all pitch angles, and the amplitude of the peak-to-peak surface variation increased as the absolute

value of α_1 increased. Incremental changes in the free surface topology occur as the absolute value of pitch angle becomes larger but a major difference is noted when comparing the free surface topology from two equal pitch angles of opposite sign. This is a direct result of the difference in both the generated bound circulation, and the influence the free surface has on positive pitch angles versus negative pitch angles, as shown in Figure 23.

Although an ideal CycWEC would have no up-wave effects resulting from its operation, Figure 26 suggests the presence of a small amplitude disturbance travelling in the up-wave direction with that same period as the rotating hydrofoil. This will reduce the overall efficiency of the device, however, the amplitude of the peak-to-peak up-wave disturbance was an order of magnitude smaller than that of the down-wave disturbance so its effect will be small.

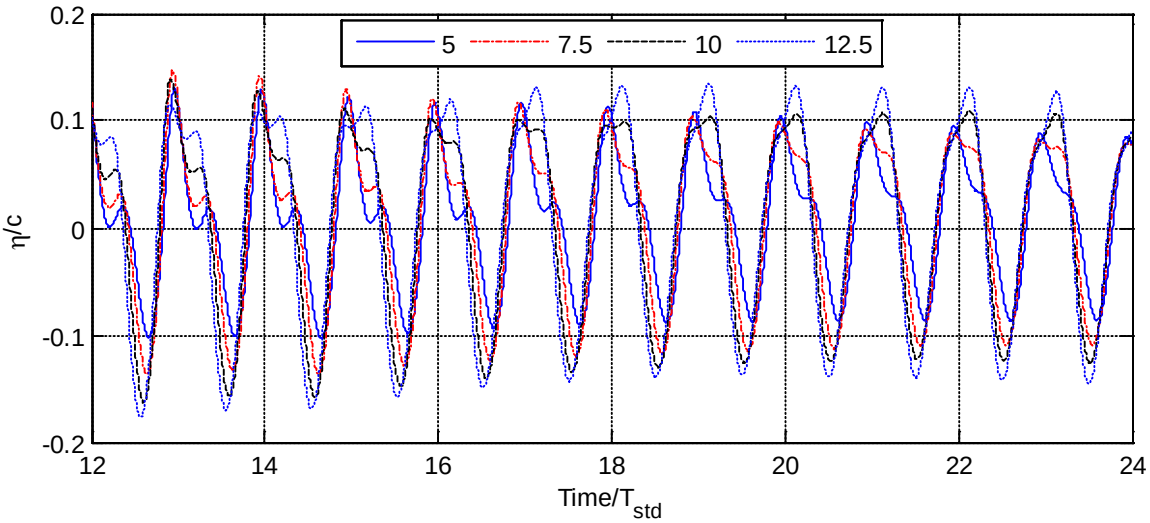

a) General view of free surface topology at *x* = 8 m from origin.

Figure 24 - Free surface topology for single hydrofoil wave generation at positive pitch angles.

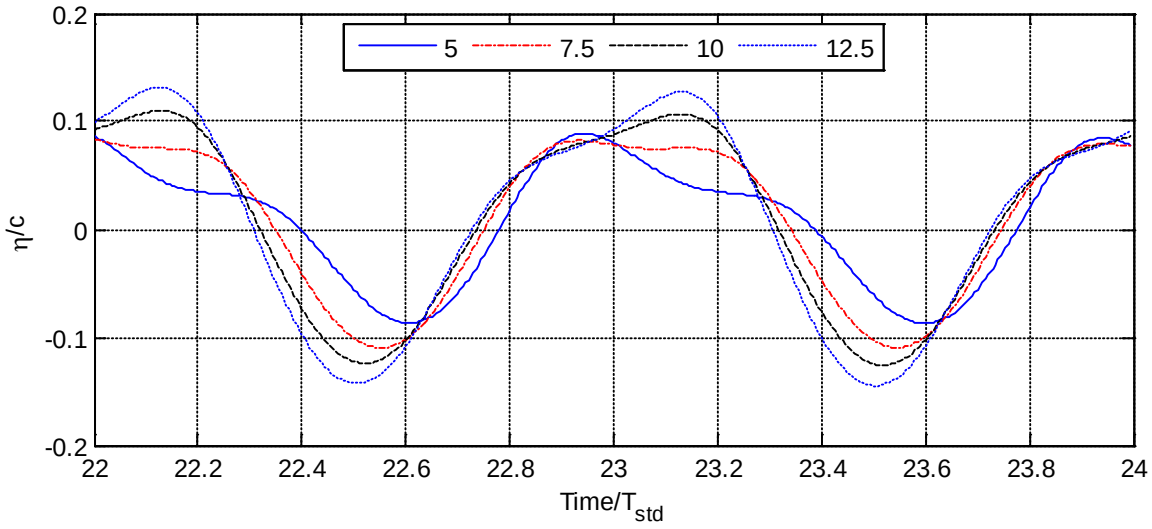

b) Detailed view of free surface topology at *x* = 8 m from origin.

Figure 24 – Continued.

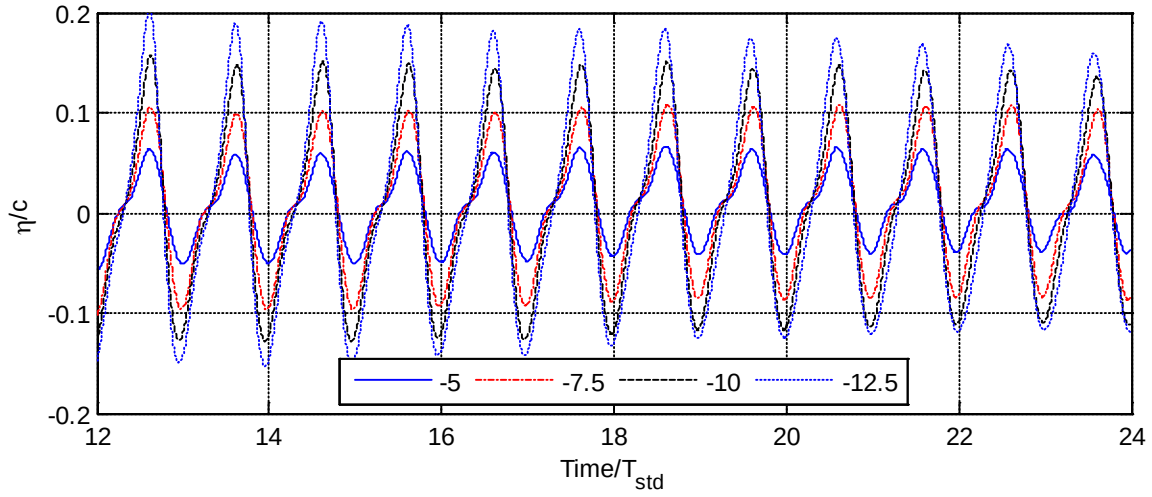

a) General view of free surface topology at *x* = 8 m from origin.

Figure 25 - Free surface topology for single hydrofoil wave generation at negative pitch angles.

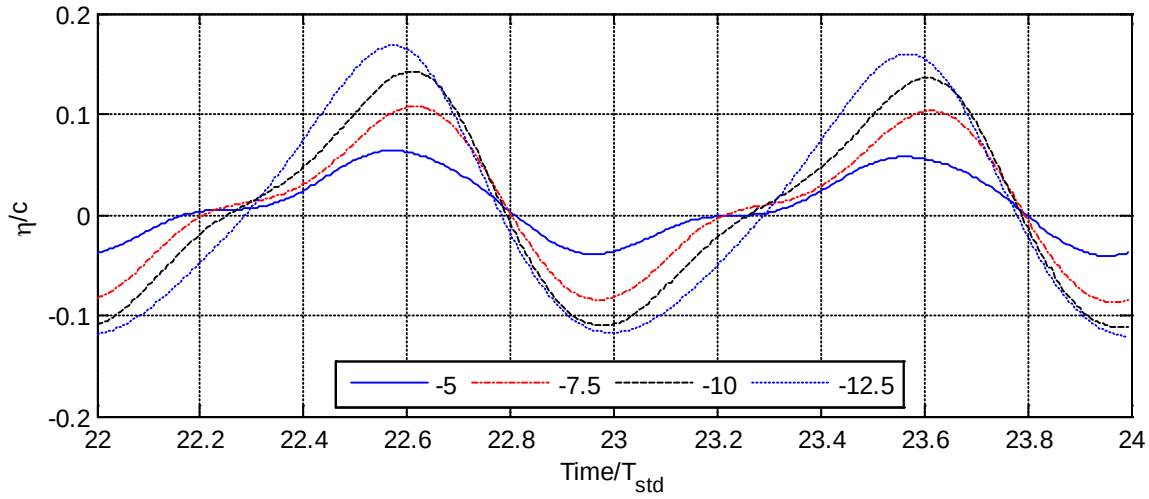

b) Detailed view of free surface topology at x = 8 m from origin.

Figure 25 - Continued.

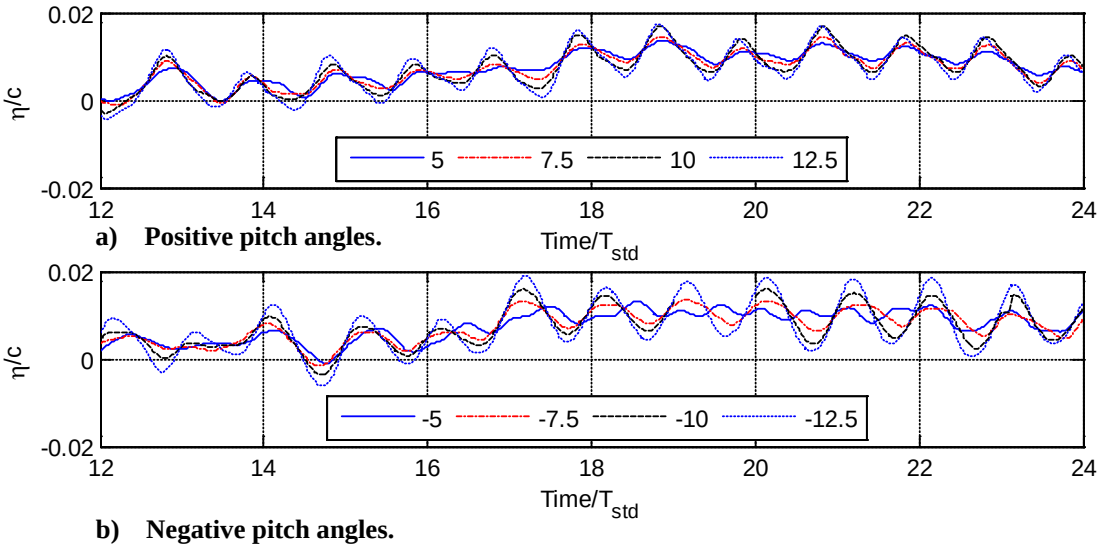

a) Positive pitch angles.

b) Negative pitch angles.

Figure 26 - General view of free surface topology for single hydrofoil wave generation at x = -8 m for all eight pitch angles.

To examine in further detail the characteristics of the generated wave fields an FFT was performed on the free surface topologies shown in Figure 24 and Figure 25. The analysis was completed using the data for $12 \leq Time/T_{std} \leq 24$ to exclude the initial transient start-up period. The results of the FFT analysis agree with the findings of [11],

which concluded that regardless of the bound circulation (or in this case α_1), a rotating hydrofoil near a free surface will generate a wave field, primarily consisting of a fundamental wave, W_1, with period T_{std} and its 1st harmonic, W_2, with period $T_{std}/2$. Note that the URANS simulations do predict higher order harmonics, W_3 and W_4, but their amplitudes are at least one order of magnitude smaller than W_2 and therefore do not carry significant amounts of energy.

The amplitude variation of the primary and secondary wave heights, H_1 and H_2, and phase angles, ψ_1 and ψ_2, as a function of α_1 are shown in Figure 27. The primary wave height, H_1, increased at a greater rate as α_1 increased for negative pitch angles compared to an equivalent increase in positive pitch angle. The trends noted in Figure 27 suggest the primary wave heights will continue to decrease as the absolute value of pitch angle decreases, however initial simulations (not shown) suggested the minimum will occur at $\alpha_1 = -2.5°$ instead of $\alpha_1 = 0°$. The secondary wave height, H_2, was found to decrease as the pitch angle varied positively from $\alpha_1 = 0°$, and increase as the pitch angle was varied negatively from $\alpha_1 = 0°$. This trend held true until $\alpha_1 = \pm 10°$, at which point H_2 remained relatively constant as the absolute value of α_1 increased.

Examining the primary and secondary phase angles, ψ_1 and ψ_2, as a function of pitch angle showed the primary phase angles varied by less than 10° and 2°, for positive and negative pitch angles, respectively. The mean difference in phase angles between equal but oppositely pitched hydrofoils is 176.6°, suggesting that oppositely pitched hydrofoils would be near ideal for two-hydrofoil wave generation. The secondary phase angle, ψ_2, was found to vary linearly with positive pitch angles, whereas negative pitch angles fluctuations resulted in minimal change in ψ_2. This suggests that cancellation of the first

harmonic generated by each hydrofoil to increase device efficiency, as suggested in [11], is possible but not ideal.

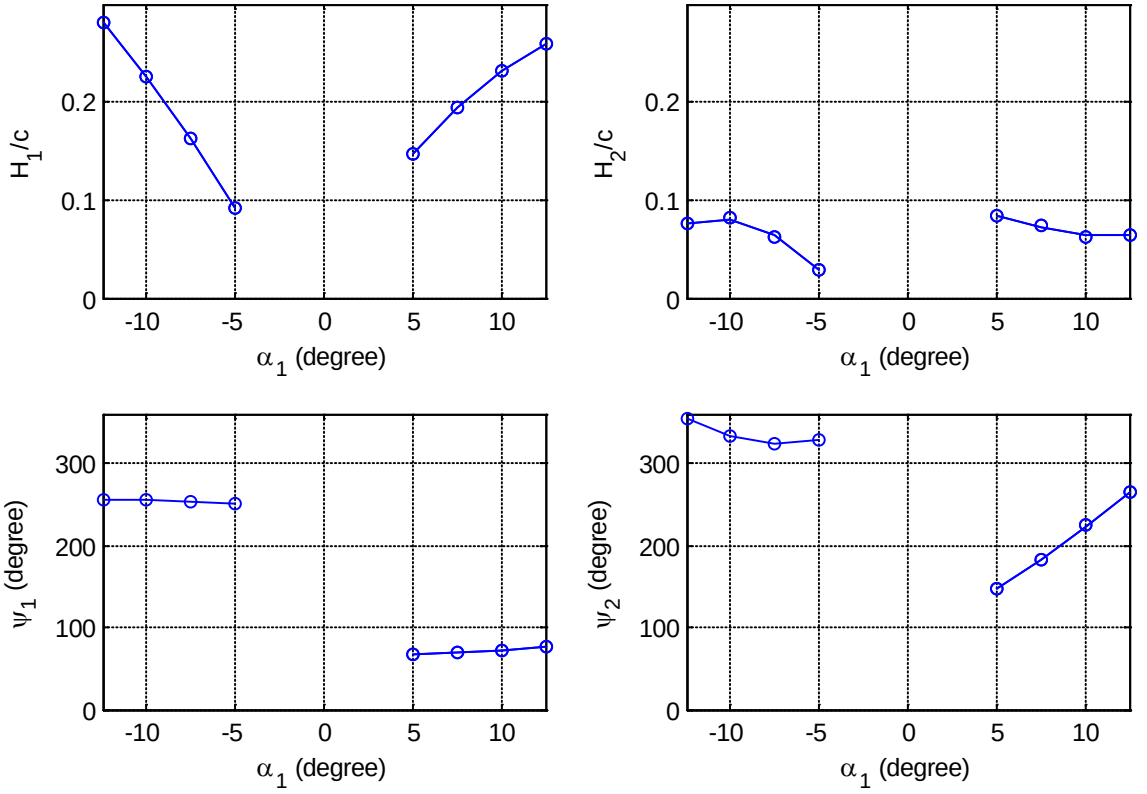

Figure 27 - Primary and secondary down-wave wave heights and phase angles as a function of α_1 for single hydrofoil wave generation.

5.1.2. Surface Pressure Distributions

A key advantage of the URANS simulations over previous inviscid simulations and experiments is the ability to investigate the detailed flow field around the hydrofoil. Hydrofoil surface pressure distributions are shown in Figure 28 during its final rotation. To examined the changes in the surface pressure distribution with hydrofoil circumferential position, C_p was plotted at θ = 0.88°, 90.88°, 180.88°, and 270.88° for α_1 = ±5°, ±7.5°, ±10°, and ±12.5°. The pressure coefficient, C_P, is defined as:

$$C_p = \frac{p - p_\infty}{\frac{1}{2}\rho(\omega R)^2} \tag{19}$$

where $p_\infty = 0$ and p is the static pressure with the hydrostatic pressure removed, which was calculated relative to the undisturbed free surface where $y = 0$ m.

As shown in Figure 28, the stagnation pressure coefficient is approximately $C_P = 1$ for all cases, but it did vary slightly due to the interaction of the hydrofoil with its own wake deficit and the free surface. Differences between the pressure distribution on the top and bottom surfaces of the hydrofoil were noted throughout the circumferential positions, indicating there is always a lift force and bound circulation which is why a fundamental wave is being generated for all examined pitch angles.

While there are variations in C_P with circumferential position for all pitch angles, the largest variations occurs for positive pitch angles. Although for these cases there is minimal change in surface pressure distribution for $\theta = 90°$, $\theta = 180°$, and $\theta = 270°$, when $\theta = 0°$ there is a significant change in the pressure distribution on both the upper and lower surfaces. At this point there is a drop in total pressure distribution suggesting the lifting performance of the hydrofoil has decrease which is likely due to the interaction of the hydrofoil and free surface. These findings are in agreement with the experimental findings of [23], which showed that the suction is reduced on the upper surface as a hydrofoil with a positive pitch angle is positioned closer to the free surface. It is interesting to note that for negative pitch angles there are large variations in peak suction C_P values for all circumferential positions and the maximum C_P difference between the upper and lower surfaces occurs at $\theta = 90°$. The above noted trend would tend to indicate sudden increase in lifting performance as the negatively pitched hydrofoils neared $\theta =$

90° which may also indicate a reduced interaction with the free surface. However, a key difference for these pitch angles is that the suction occurs on the inner surface which is further away from the free surface. The variation in pressure distribution for the negative pitch angles at θ = 90° may also be a result of the difference in its remaining wake compared to other circumferential positions.

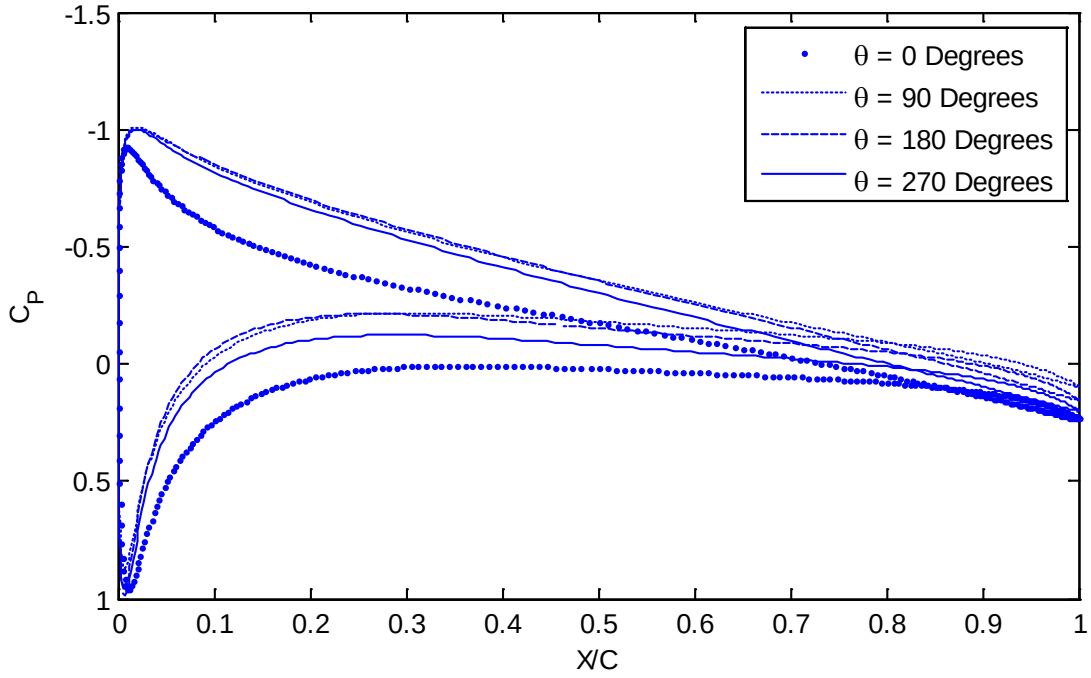

a) α_1 = 5°.

Figure 28 - Pressure coefficient along hydrofoil surface for all pitch angles.

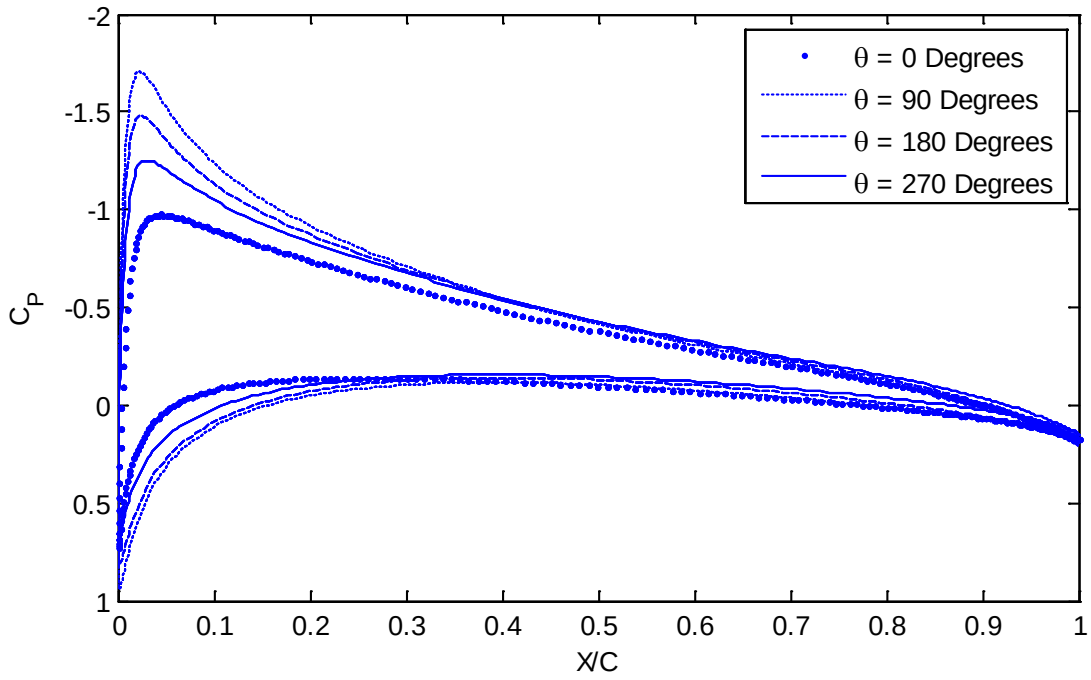

b) α_1 = -5°.

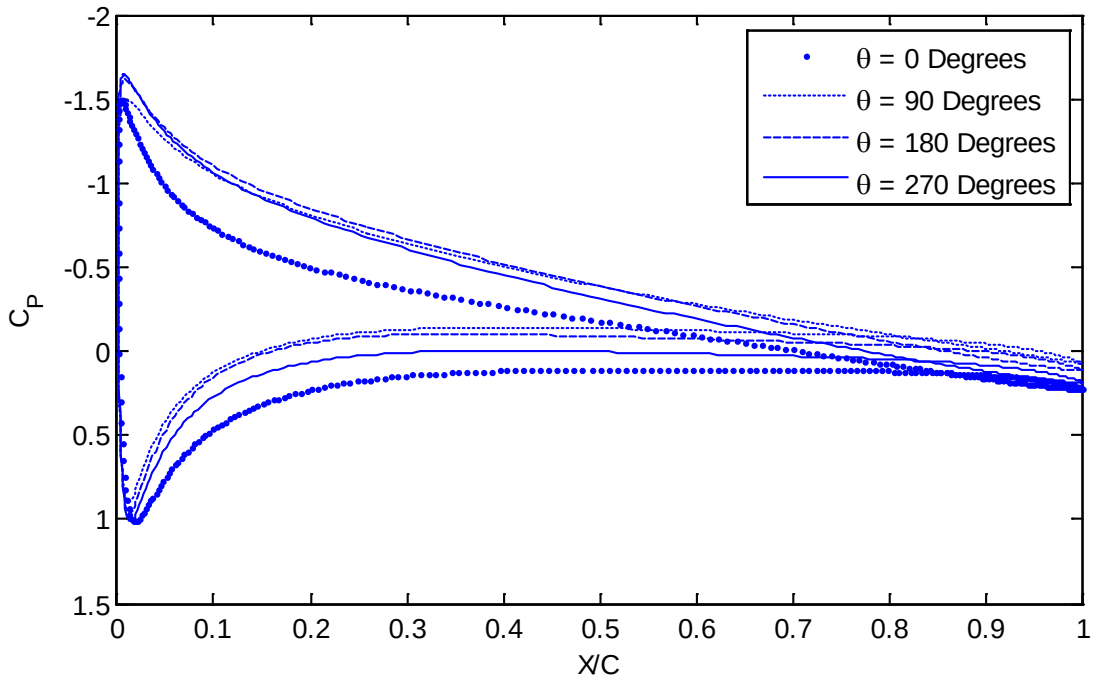

c) α_1 = 7.5°.

Figure 28 - Continued.

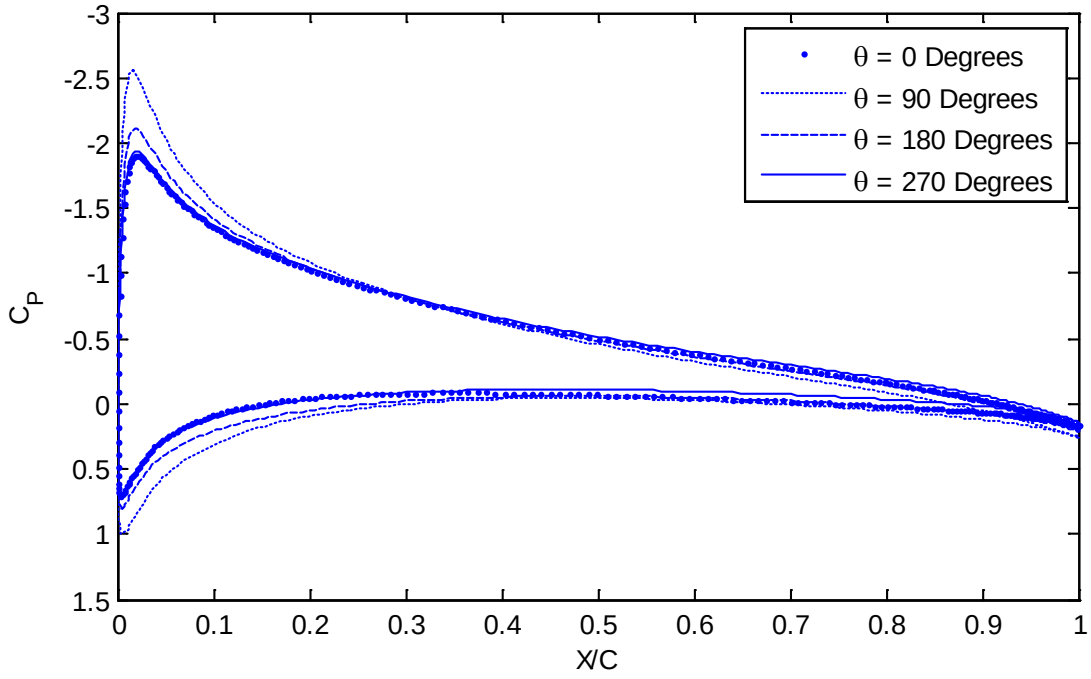

d) α_1 **= -7.5°.**

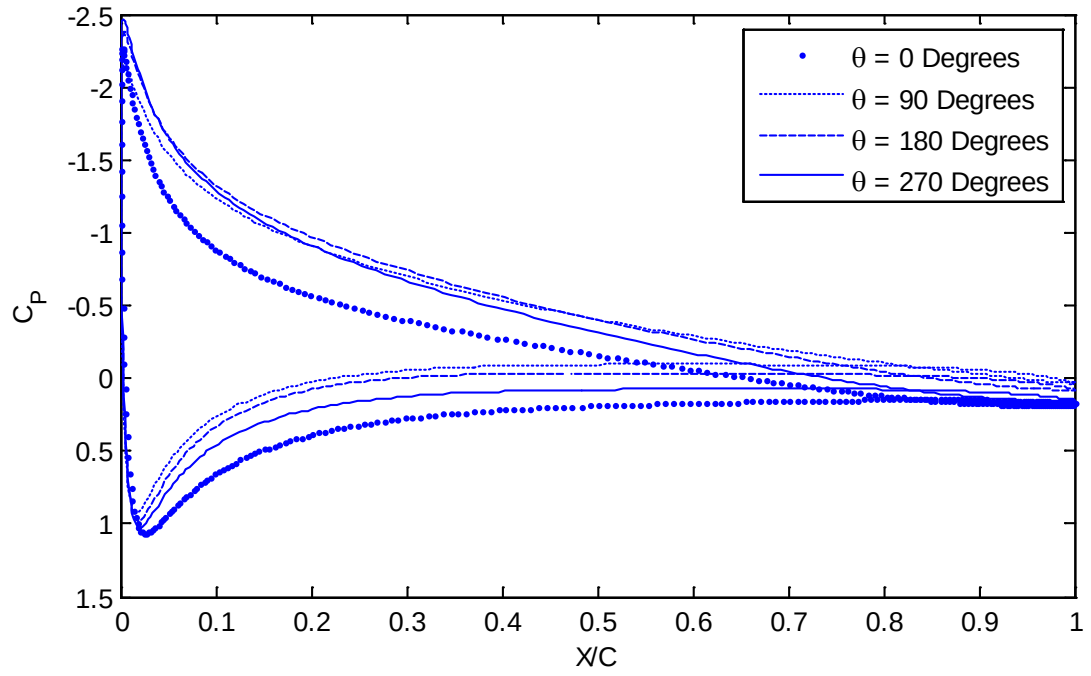

e) α_1 **= 10°.**

Figure 28 - Continued.

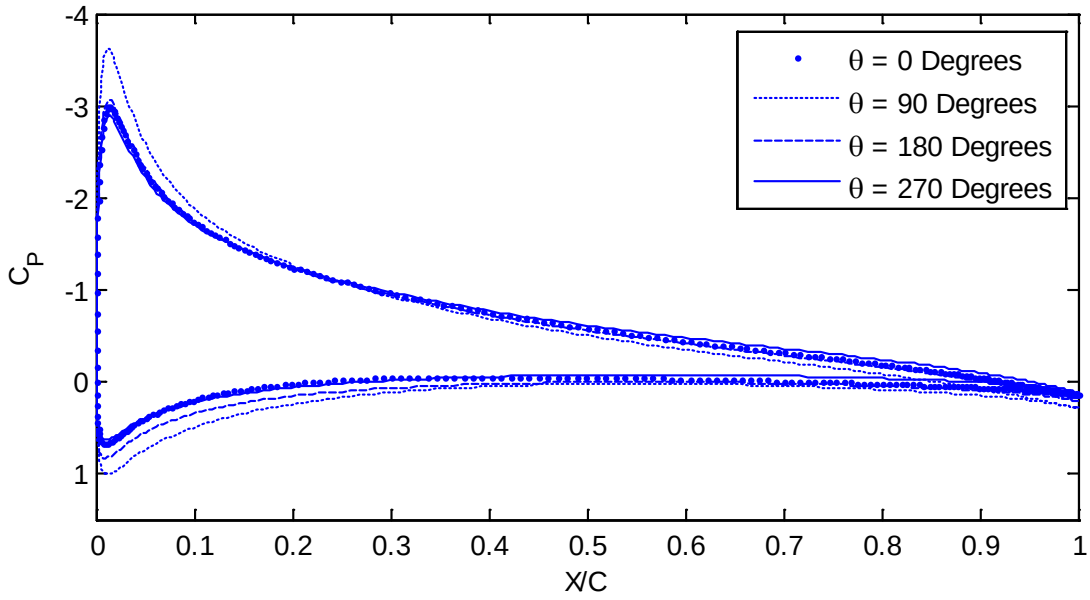

f) α_1 **= -10°.**

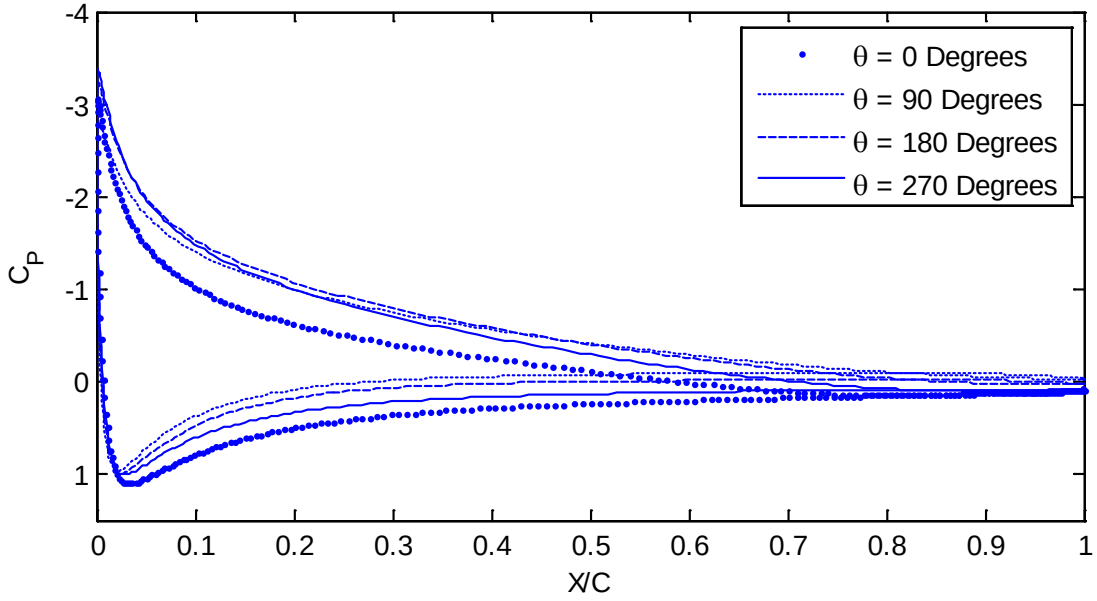

g) α_1 **= 12.5°.**

Figure 28 - Continued.

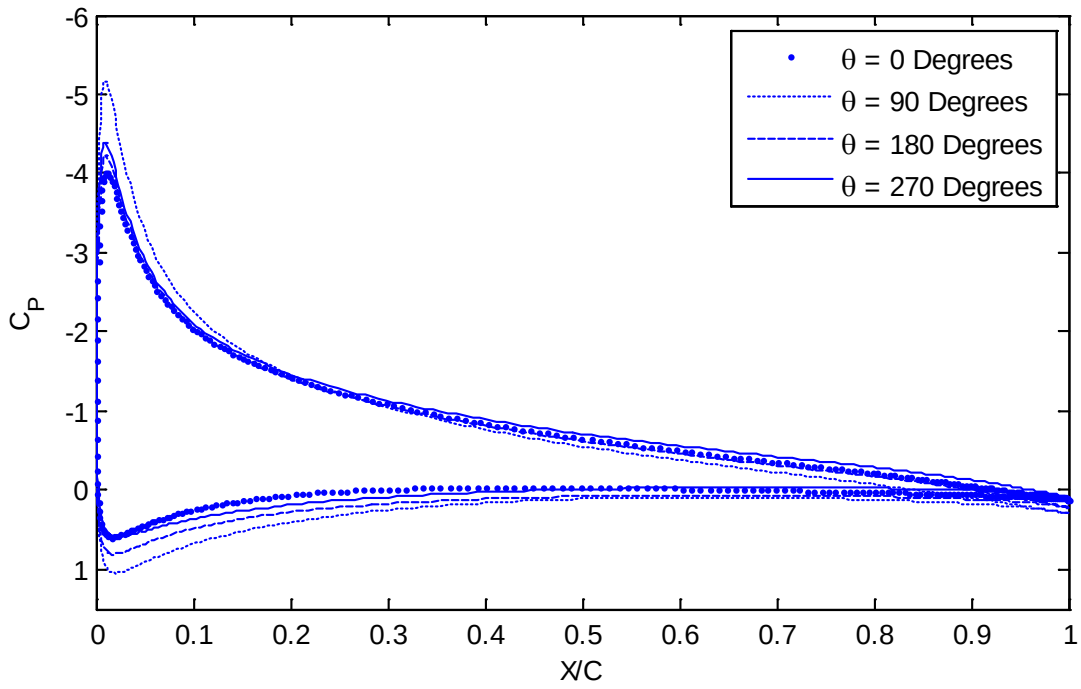

h) α_1 **= -12.5°.**

Figure 28 - Continued.

5.1.3. Hydrodynamic Forces

Another key advantage of the URANS simulations over previous inviscid simulations is the ability to predict the resulting hydrodynamic forces on the rotating hydrofoil. This was achieved by integrating the wall shear stress and the surface pressure along the hydrofoil surface. Unsteady body-fixed force coefficients, as defined in Section 3.1, are shown in Figure 29. The hydrodynamic forces varied significantly with pitch angle. In general, as α_1 increased positively, C_R also increased positively indicating a net outward radial force. Whereas as α_1 increased negatively, C_R increased negatively indicating a net inward radial force. The variation of C_T with pitch angle was more complicated, but was clearly largest for α_1 = -12.5º, indicating that the tangential force is largest for this pitch angle.

Fluctuations of both C_R and C_T with circumferential position are due to the interaction of the hydrofoil with the free surface, and possibly, also due to unsteady interactions of the hydrofoil and its own wake deficit. For positive pitch angles it was found that $|C_T|$ was at a maximum when $\theta = 90°$ and $|C_T|$ was at a minimum directly after the hydrofoil passes under the free surface. For negative pitch angles, $|C_T|$ was also found to be at a maximum near $\theta = 90°$ but the minimum of $|C_T|$ occurred just before the hydrofoil approached the free surface.

Analyzing the C_R fluctuations for positive pitch angles revealed that $|C_R|$ was at a maximum when $\theta = 270°$. This maximum is immediately followed by a sudden decrease in $|C_R|$ as the hydrofoil passes underneath the free surface until $|C_R|$ is at a minimum near $\theta = 45°$. The sudden decrease in $|C_R|$ is in strong agreement with the surface pressure distribution at $\theta = 0°$ in Figure 28 and the experimental findings of [23], which concluded that the performance of a lifting hydrofoil decreased as it was brought closer to a free surface. Negative pitch angles, however, produced significantly different C_R variations. A minimum in $|C_R|$ was found at $\theta = 0°$ which, was immediately followed by a sudden increase in $|C_R|$ until the maximum was reached at $\theta = 90°$. Having a maximum in $|C_R|$ at $\theta = 90°$ aligned with the C_P results, which found the largest difference in total surface pressure between the upper and lower hydrofoil surfaces at the same circumferential position. As the pitch angle increased in the negative direction second local minimums and maxima were noted in $|C_R|$ at $\theta = 180°$ and $\theta = 270°$, respectively. Thus, for negative pitch angles it was noted that for $|C_R|$, a maximum and minimum occurred twice every revolution.

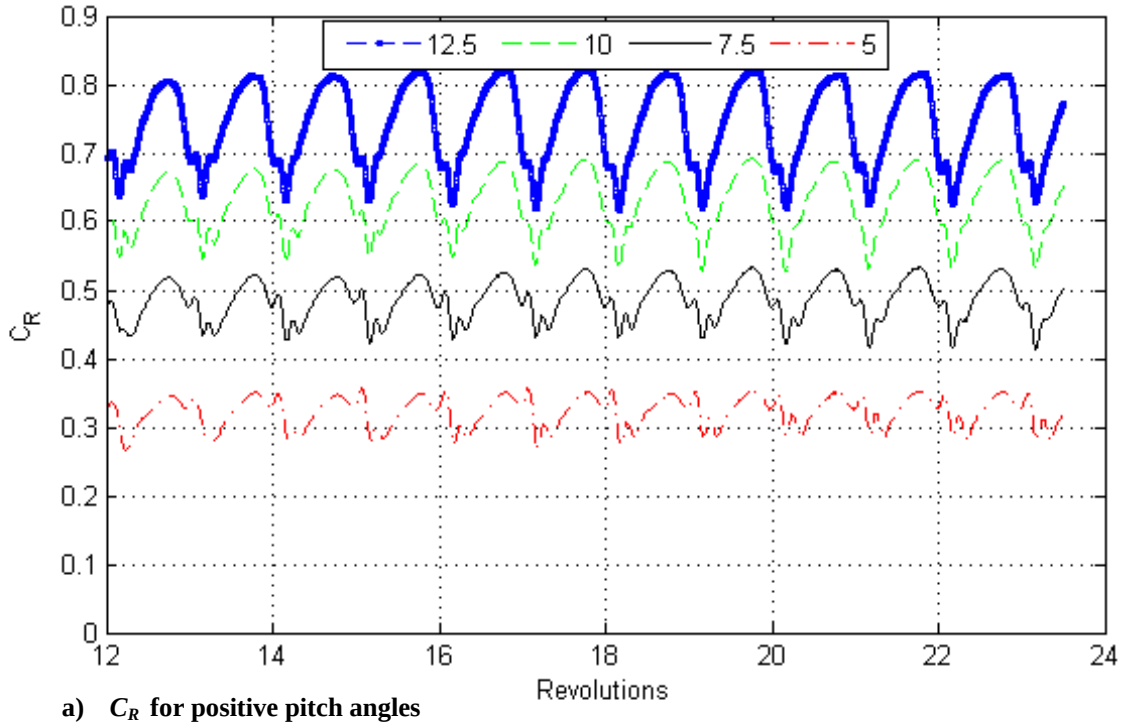

a) C_R for positive pitch angles

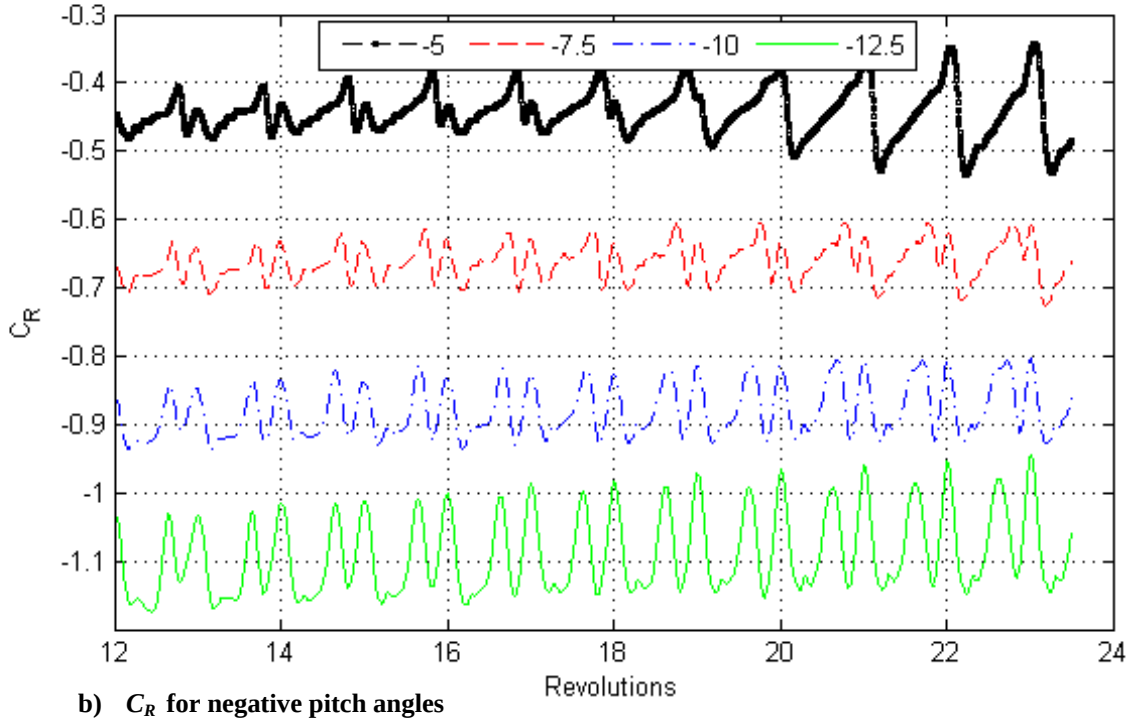

b) C_R for negative pitch angles

Figure 29 - Hydrofoil body-fixed radial and tangential force coefficients for all tested pitch angles.

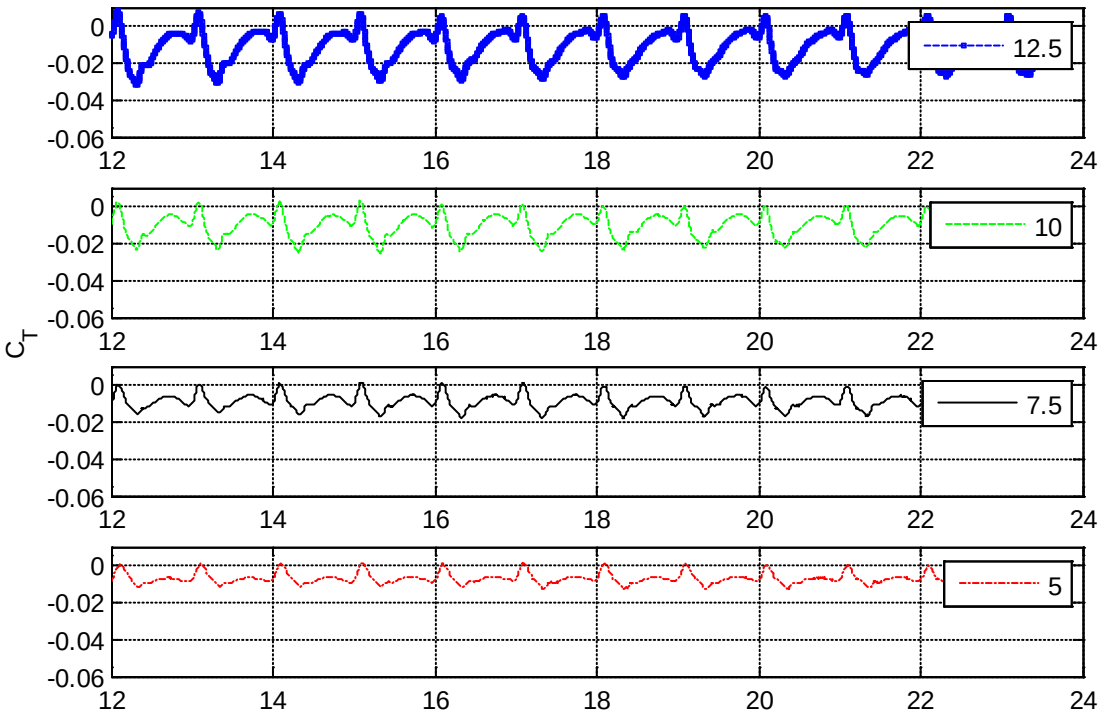

c) C_T for positive pitch angles

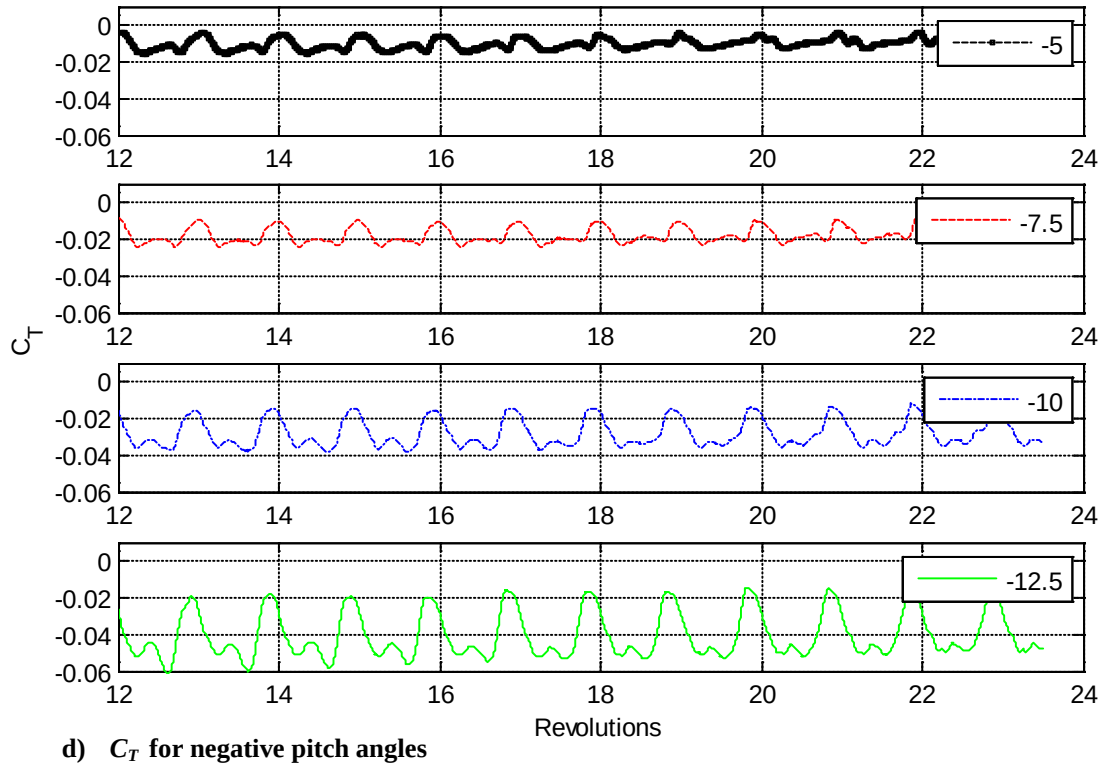

d) C_T for negative pitch angles

Figure 29 - Continued.

CHAPTER 6

6. NUMERICAL WAVE GENERATION RESULTS

URANS predictions of numerical wave generation resulting from the addition of a mass source region in the CFD domain are presented in this section. Based on the grid refinement and time step studies completed for numerical wave generation in sections 4.2.1 and 4.2.2, a fine unstructured grid was employed below the free surface for all simulations with Δt = 0.01255 seconds. The numerical wave tank is validated by comparing the generated incident wave field to linear wave theory for deep ocean waves with constant water depth. The free surface topology is investigated at a constant horizontal location while the spatially and temporally variant velocity fields are examined in both the near and far field regions.

6.1. Flow Field Modelling – Near Field Region

To highlight the fundamental operating principles of the mass source region as it generates a harmonic incident wave field, the near field flow is examined throughout one wave period. The velocity vector field within and the free surface topology above the mass source region are studied. Before the overall mass source region output is observed, an understanding of the mass source strength fluctuations within the mass source region is required. The spatially and temporally varying mass source strength is defined in section 3.2.3 and generates waves based on the user defined wave heights and phase shifts. At the center of the mass source term, for example, the mass source strength simply fluctuates as a cosine function as shown in Figure 30.

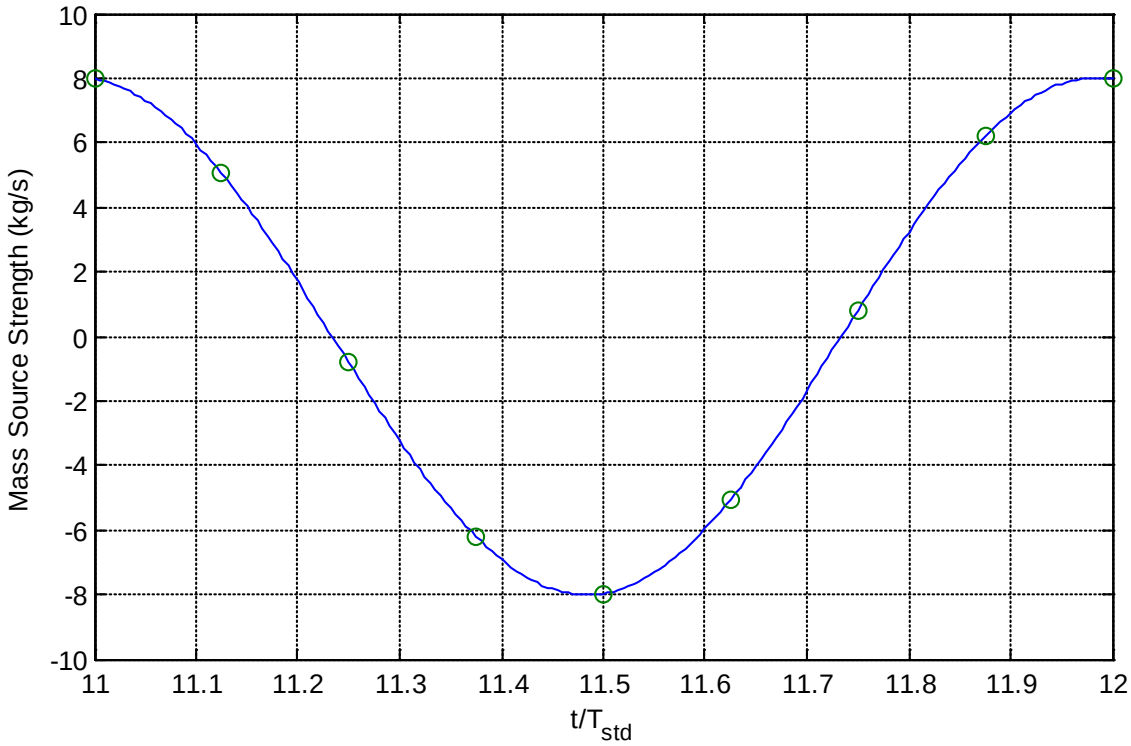

Figure 30 - Fluctuation in mass source strength at the center of the mass source zone during one wave period.

The velocity field within and free surface topology above the mass source region are shown in Figure 31 at nine instants in time throughout one wave period. The mass source term strength at the center of the mass source region at each instant in time is defined in Figure 31 and is equivalent to that plotted in Figure 30. Beginning with Figure 31 a), where the source strength is of large magnitude and positive, it is observed that the velocity vector field in and around the mass source region is clearly representative of the strong mass flow into the domain. As the source strength decreases but remains positive, as shown in Figure 31 b), the velocity field in the mass source region remains defined by the mass flow into the domain but the velocity field immediately surrounding the mass source region is now being influenced by the local velocity field. As the source strength nears zero, as shown in Figure 31 c), the velocity field in and around the source region becomes completed dominated by the local flow field because the source is not adding or subtracting mass from the domain. This trend is reversed and/or repeated in Figure 31 d) through i).

Also shown in Figure 31 is that at each point within the period the free surface directly above the center of the mass source zone fluctuated as expected, being pushed up when the source is positive and pulled down when the source is negative. However a slight time delay existed between the mass source strength reaching its maximum and the free surface reaching its maximum height is observed, which was due to the vertical displacement between the two.

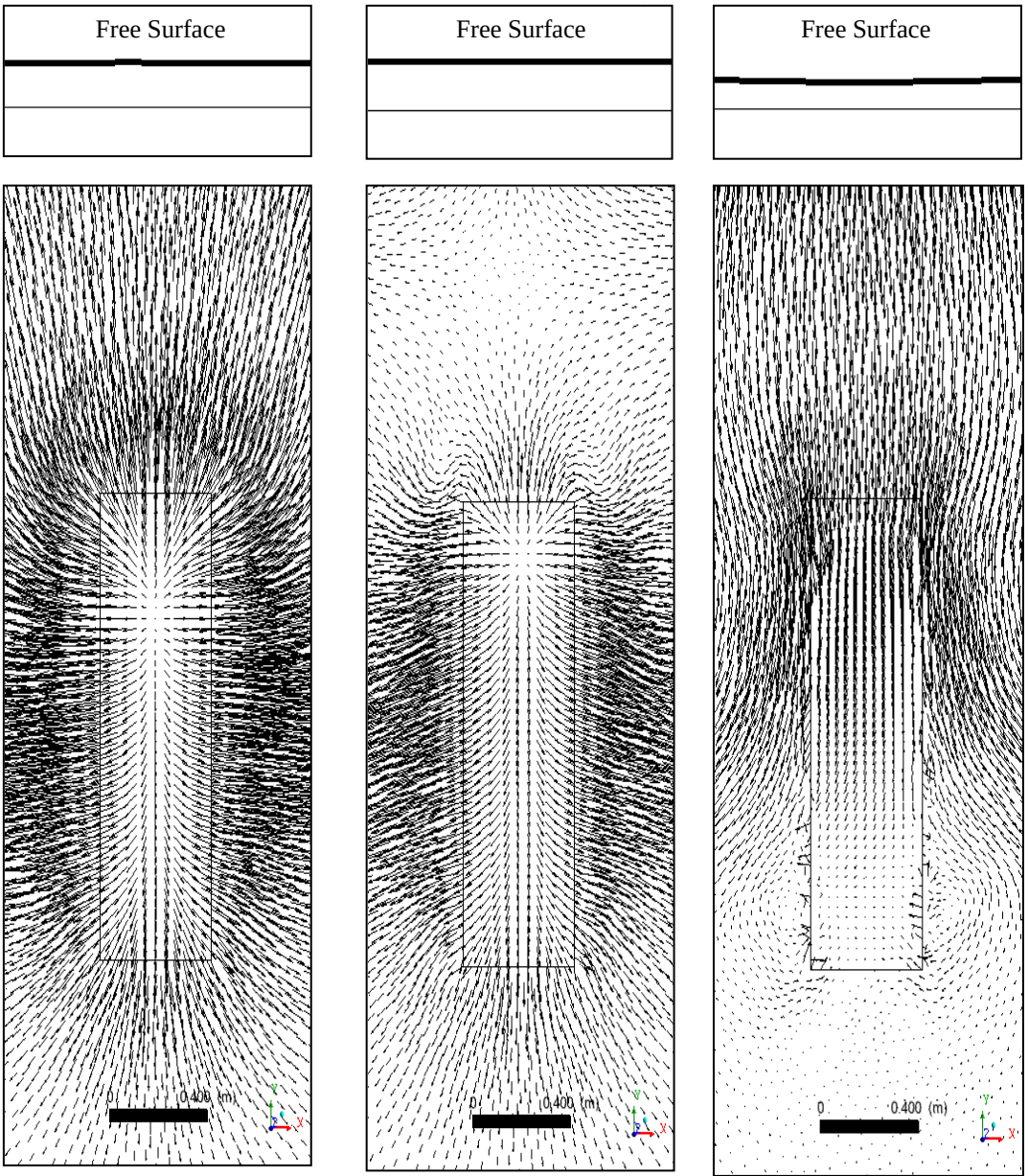

a) t/T_{std} = 11, s_m = 7.97 kg/s b) t/T_{std} = 11.125, s_m = 5.05 kg/s c) t/T_{std} = 11.25, s_m = -0.819

Figure 31 - Simulated free surface displacement above and velocity field around mass source zone at nine time intervals over one wave period (T_{std} = 2.51 seconds).

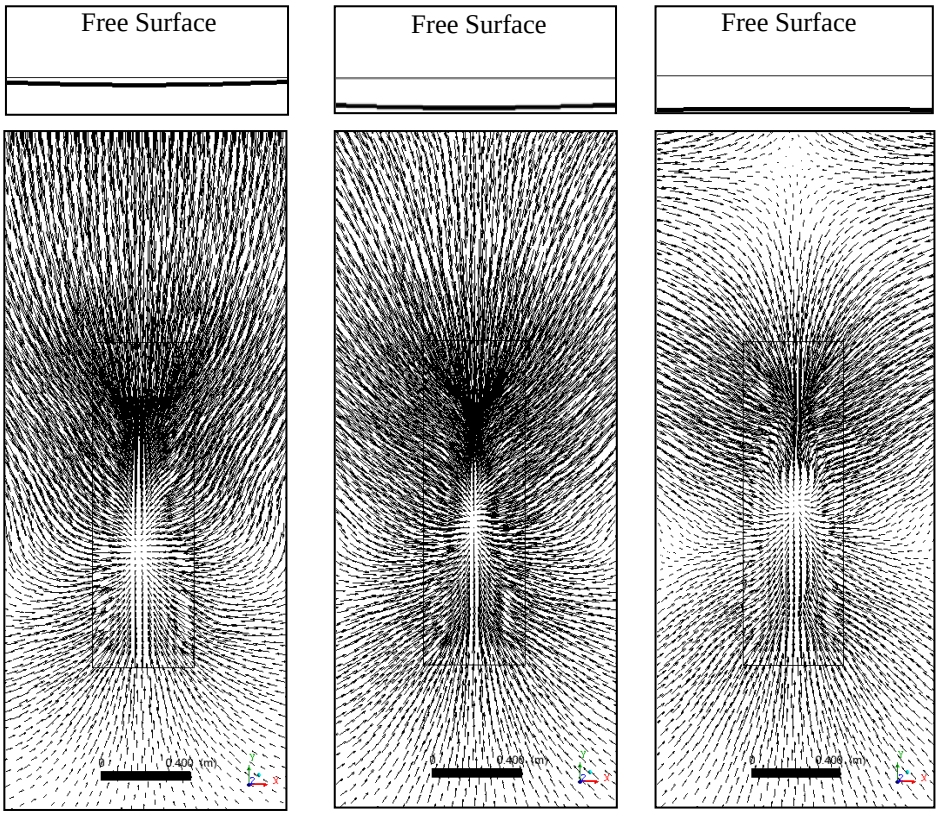

d) t/T_{std} = 11.375, s_m = -6.21 kg/s e) t/T_{std} = 11.50, s_m = -7.97 kg/s f) t/T_{std} = 11.625, s_m = -5.06 kg/s

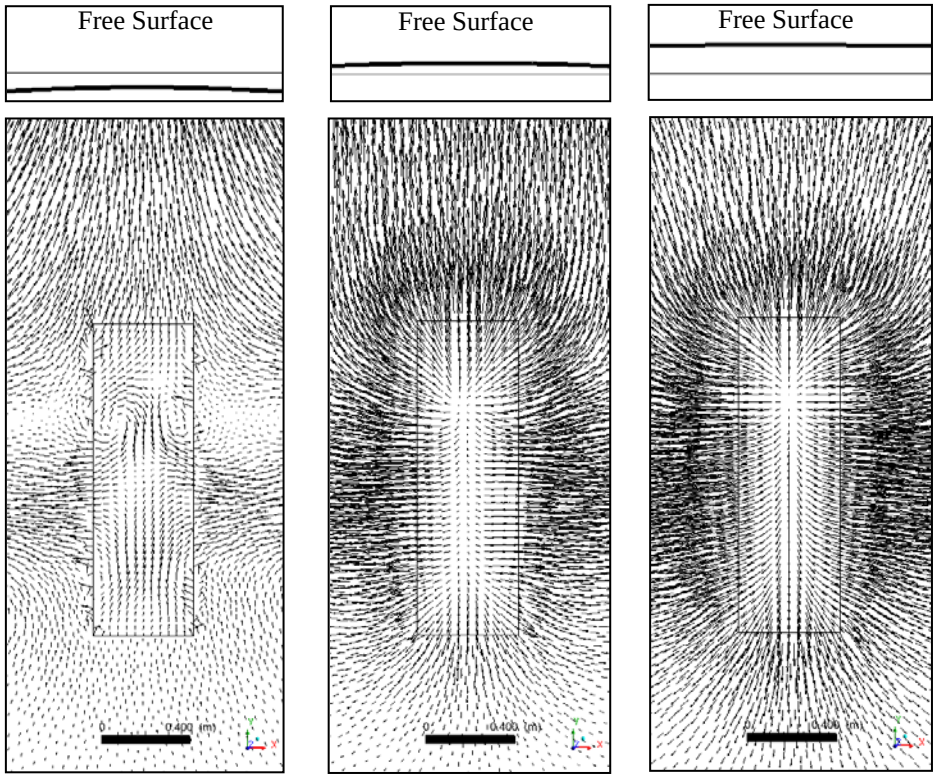

g) t/T_{std} = 11.75, s_m = 0.816 kg/s h) t/T_{std} = 11.875, s_m = 6.21 kg/s i) t/T_{std} = 12, s_m = 7.97 kg/s

Figure 31 - Continued.

6.2. Free Surface Topology

By design, the numerical wave tank generates linear wave fields that propagate from the mass source region towards the horizontal boundaries of the domain. The spatially and time varying source strength was previously defined in section 3.2.3. To initially evaluate the temporal accuracy the numerical wave tank, the free surface topology is investigated at x = 0 m.

Figure 32 contains a general and detailed view of free surface topology for a non-dimensional incident wave height of $H_A/c = 0.334$ and an incident wave phase shift of $\psi_A = -90.6°$. The analytical solution based on linear wave theory is also plotted for comparison purposes. The low accuracy of the numerical wave tank when $Time/T_{std} < 3$ shown in Figure 32 a) is due to the inability of the mass source term to instantaneously produce a fully developed flow field ten meters from its origin. Once the generated wave field is well established throughout the numerical domain the URANS and theoretical results are in strong agreement having an RMS difference of 5.94×10^{-3} for the location of the free surface.

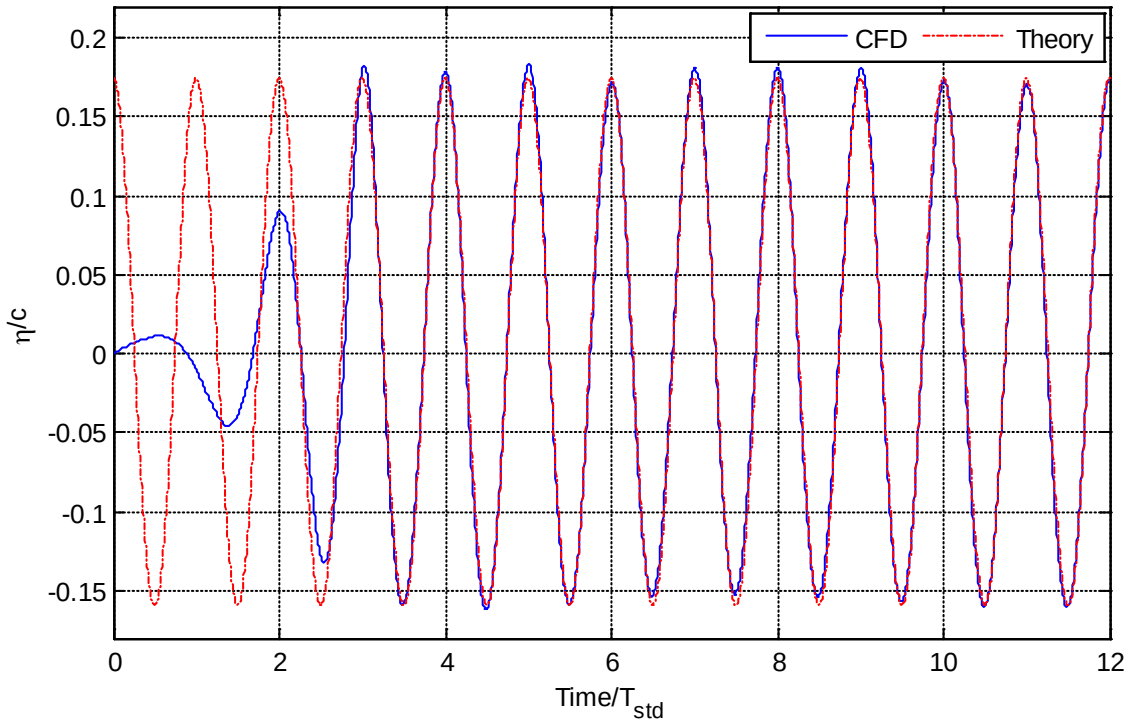

a) General view of generated wave field at *x* = 0 m.

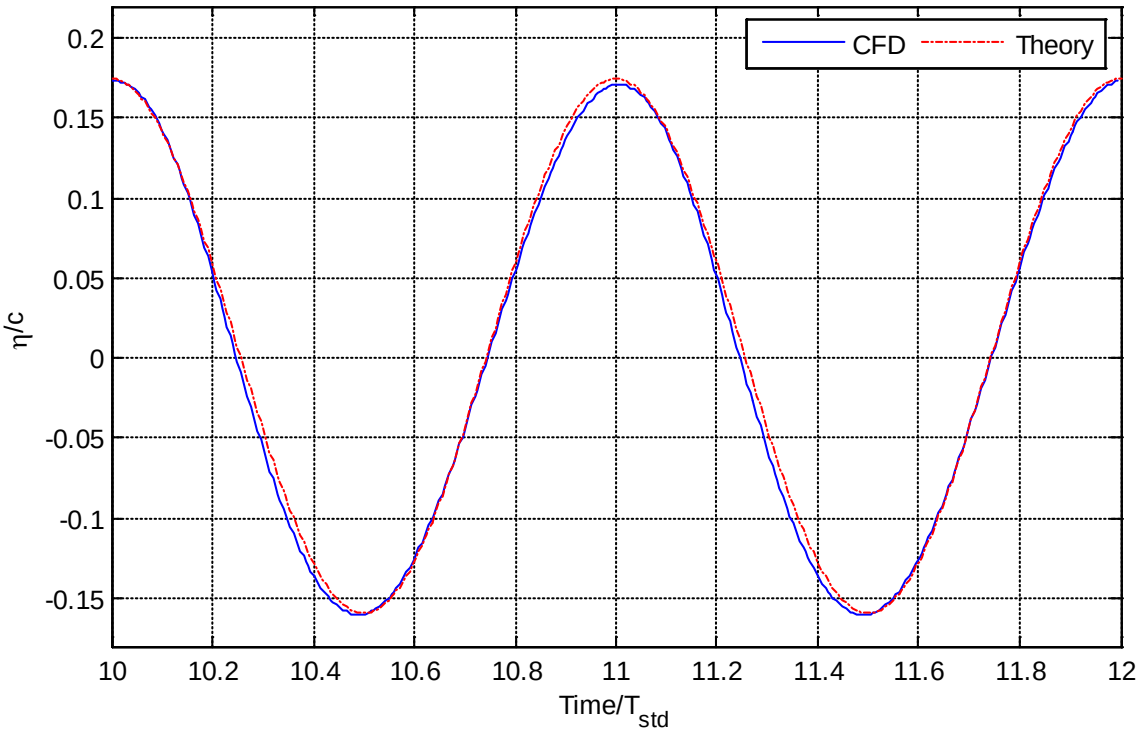

b) Detailed view of generated wave field at *x* = 0 m.

Figure 32 - Comparison of free surface topology from linear wave theory and numerical wave tank.

6.3. Velocity Profile Development

In order to evaluate the spatial accuracy of the numerical wave tank, the *u* and *v* velocity profiles under the generated wave field at eight horizontal locations, as shown in Figure 33, are compared to linear wave theory solutions at one instant in time (i,e., when $Time/T_{std}$ = 12). Note the horizontal and vertical velocity components of a far field progressive wave field are defined in section 3.2.3. The velocity profiles are compared at four near field regions (x-x_s < 6 m) and four far field regions (x-x_s > 6 m). The continually improvement in velocity profile agreement shown from Figure 33 a)-e) demonstrates the spatial requirement for the wave field to fully develop. Whereas, the continued agreement at x-$x_s \geq$ 10 m shown in Figure 33 f)-h) demonstrates that there is very little numerical dissipation of the generated wave field. The agreement at x-x_s = 10 m was crucial as this will be the location of the two-hydrofoil CycWEC model used to test the two-dimensional wave cancellation abilities of the device. As shown in Figure 33 h), the final horizontal location where the velocity profiles were examined was at x-x_s = 18 m or approximately at $2*\lambda_A$. Having the CFD results align well with linear wave theory at this location shows the accuracy of the model far away from its origin and is important as this will be where the wave cancellation data will be extracted during the final stage of this research. This location was selected because it is in the far field region for both the waves generated from the rotating hydrofoils and mass source region.

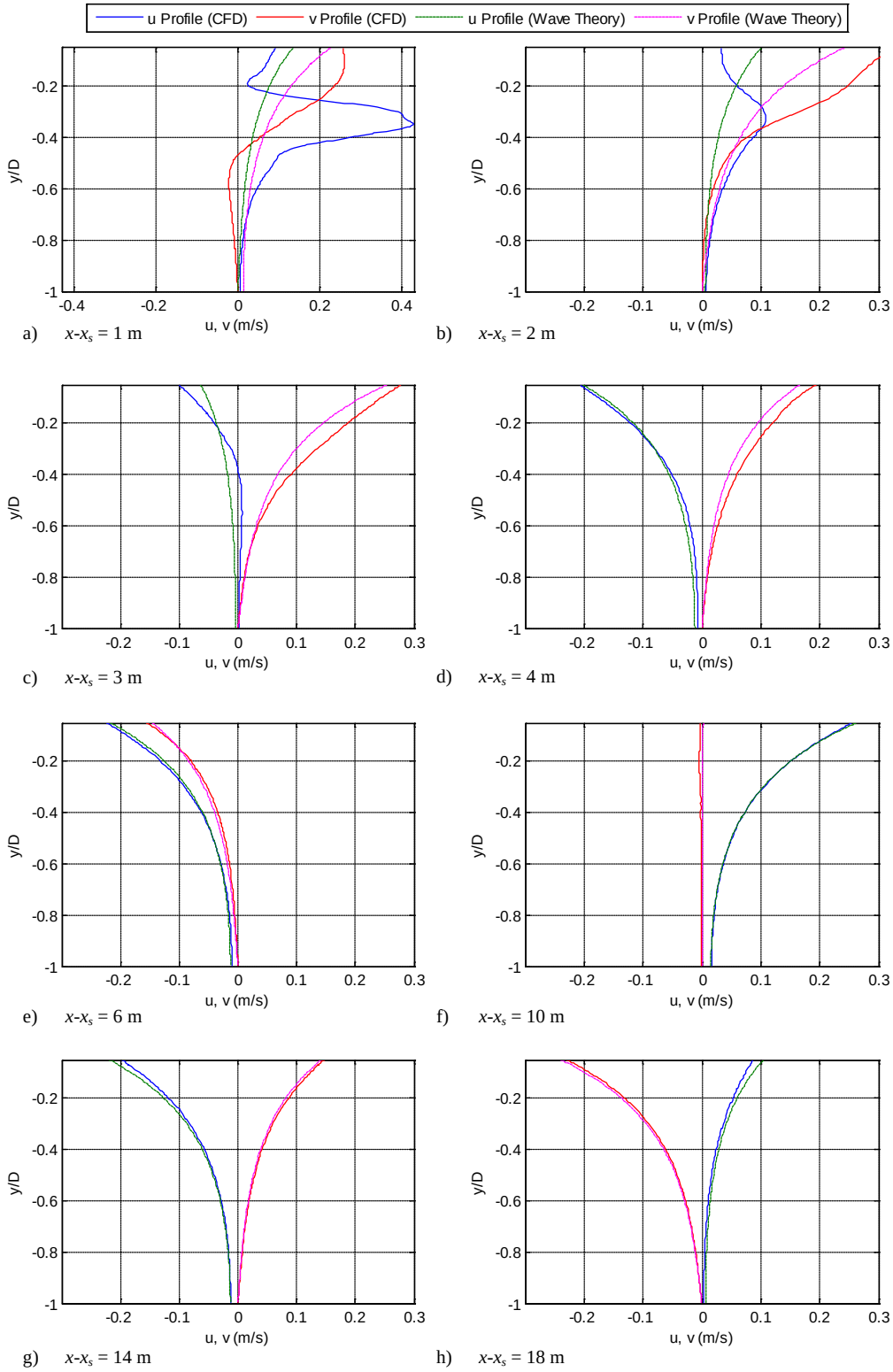

Figure 33 - Depth varying *u* and *v* velocity profiles of the incident wave field from CFD results and linear wave theory at 8 horizontal locations (measured relative to source center, x_s).

6.4. Flow Field Modelling – Far Field Region

To assess the temporal accuracy of the numerical wave tank in the far field region, the u and v velocity profiles under the generated wave field at x = 8 m are compared to linear wave theory at eight instants in time throughout one period. As shown in Figure 34, a strong agreement between the CFD and linear wave theory results was noted at each instant in time which indicates there is minimal temporal variation in the numerical wave tank performance.

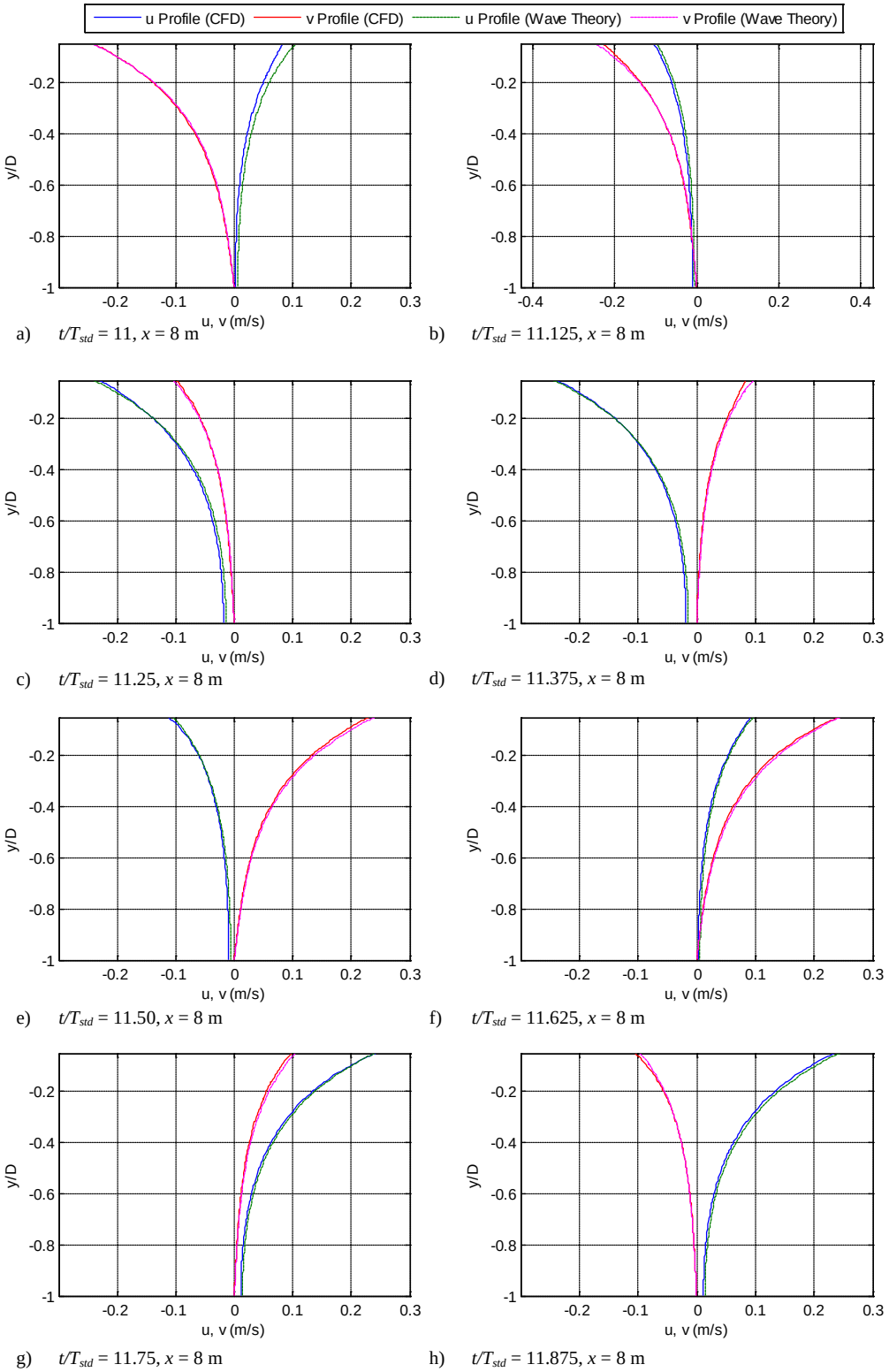

a) t/T_{std} = 11, x = 8 m b) t/T_{std} = 11.125, x = 8 m

c) t/T_{std} = 11.25, x = 8 m d) t/T_{std} = 11.375, x = 8 m

e) t/T_{std} = 11.50, x = 8 m f) t/T_{std} = 11.625, x = 8 m

g) t/T_{std} = 11.75, x = 8 m h) t/T_{std} = 11.875, x = 8 m

Figure 34 - Depth varying u and v velocity profiles of the incident wave field from CFD results and linear wave theory at eight instants in time throughout one wave period (T_{std} = 2.51 seconds).

CHAPTER 7

7. TWO-HYDROFOIL WAVE GENERATION AND CANCELLATION RESULTS

The final objectives of the current research involve the analysis of wave generation and wave cancellation abilities of a two-hydrofoil CycWEC model using URANS simulations. The two-hydrofoil wave generation is investigated for combinations of α_1 and α_2 with equal magnitude but opposite sign (eg. α_1 = 5° and α_2 = -5°). Predicted free surface topologies, primary and harmonic wave heights, surface pressure distributions, hydrodynamic forces, required shaft power, and device wave generation efficiencies are all examined as a function of pitch angle. Finally, all knowledge gained throughout each stage of this research was combined into one final set of simulations to determine the two-dimensional wave cancellation abilities of the CycWEC when subject to regular incident wave fields. Using numerical wave generation to produce the incident wave field, the hydrodynamic efficiency of the two-hydrofoil CycWEC model is examined

along with several other parameters that have been commonly evaluated throughout this research.

7.1. Two-Hydrofoil Wave Generation

URANS predictions of the wave generation resulting from two hydrofoils rotating near a free surface are analysed in this section for pitch angle combinations of $\alpha_1 = 5°$ and $\alpha_2 = -5°$, $\alpha_1 = 7.5°$ and $\alpha_2 = -7.5°$, $\alpha_1 = 10°$ and $\alpha_2 = -10°$, and $\alpha_1 = 12.5°$ and $\alpha_2 = -12.5°$. Initially, the generated wave field is predicted based on the results of the single hydrofoil wave generation simulations. The results of two-hydrofoil URANS simulations are then analyzed in detail.

7.1.1. Predicted Characteristics of Generated Wave Field based on Single Hydrofoil Simulations

Wave generation properties of a two-hydrofoil CycWEC are predicted using the principle of superposition, which assumes the flow field behaves linearly with minimal interactions between the hydrofoils (i.e., potential flow). With this assumption, the addition of a second hydrofoil displaced $\theta = 180°$ relative to the original hydrofoil will produce a free surface topology equal to the sum of the free surface topologies resulting from the single hydrofoil wave generation simulations at α_1 and α_2, but with a phase shift of 180° applied to the free surface displacement resulting from α_2 to compensate for the change in circumferential position. This approach was applied to produce the free surface topologies shown in Figure 35 which shows that as the pitch angle is increased the resulting free surface topologies are approaching a regular wave field having a period equal to the device period. This means that generated harmonic waves are having less

effect on the resulting free surface topology as the pitch angle is increased. This is in agreement with Siegel and al. [11], which concluded that for two hydrofoils with equal and opposite circulation and 180° of phase shifts, the harmonic waves cancel making the device ideal for regular wave cancellation. These conclusions are further supported by the results of an FFT analysis of the resulting free surface. Predicted primary and first harmonic wave heights shown in Figure 36 highlight that the primary wave height increased with α_1 and the first harmonic wave height remained relatively unchanged. Note the second harmonic wave height was also predicted, but was an order of magnitude smaller than the first harmonic wave height and varied minimally with pitch angle, and therefore was not included in Figure 36.

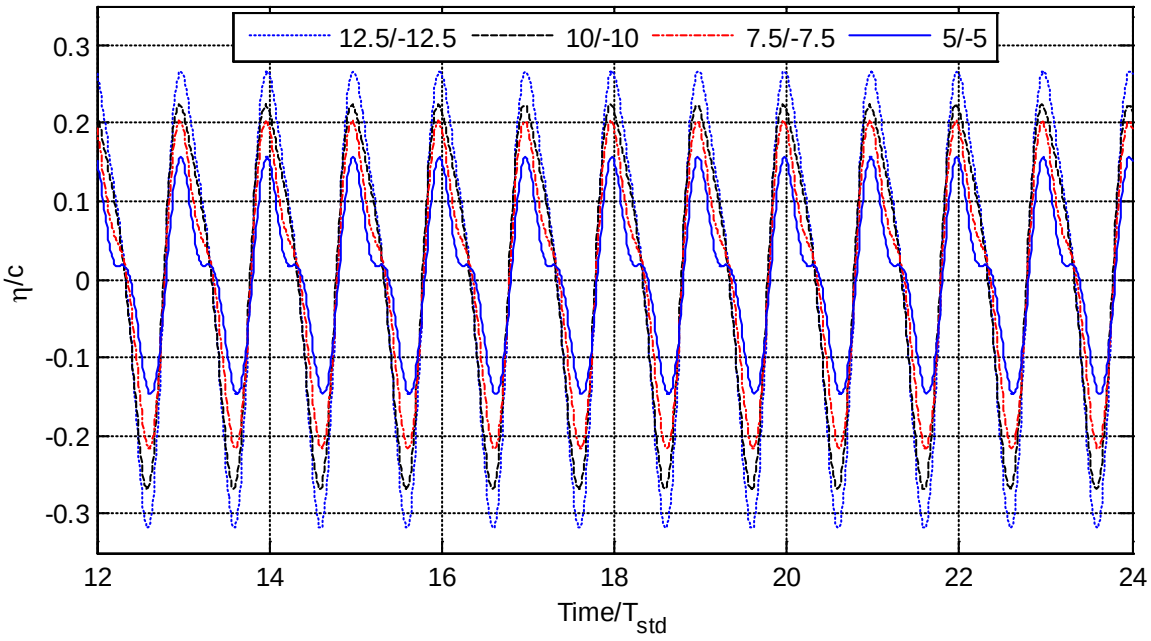

a) General view of predicted free surface topology for two-hydrofoil wave generation at *x* = 8 m.

Figure 35 - Predicted free surface topology for two-hydrofoil wave generation based on findings of single hydrofoil wave generation simulations.

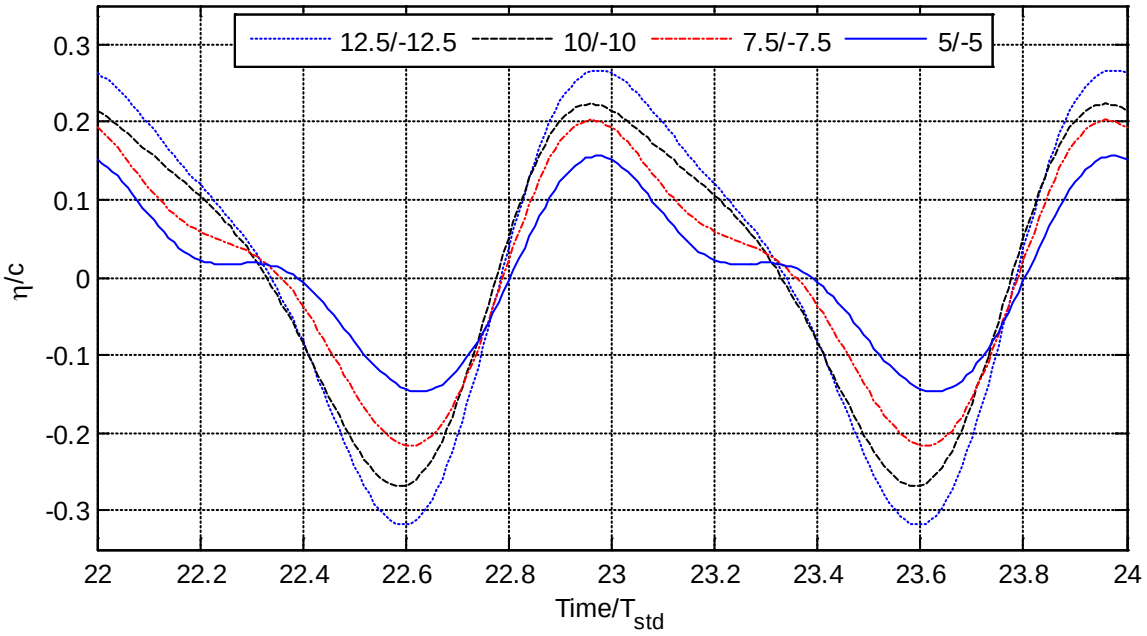

b) Detailed view of predicted free surface topology for two-hydrofoil wave generation at *x* = 8 m.

Figure 35 - Continued.

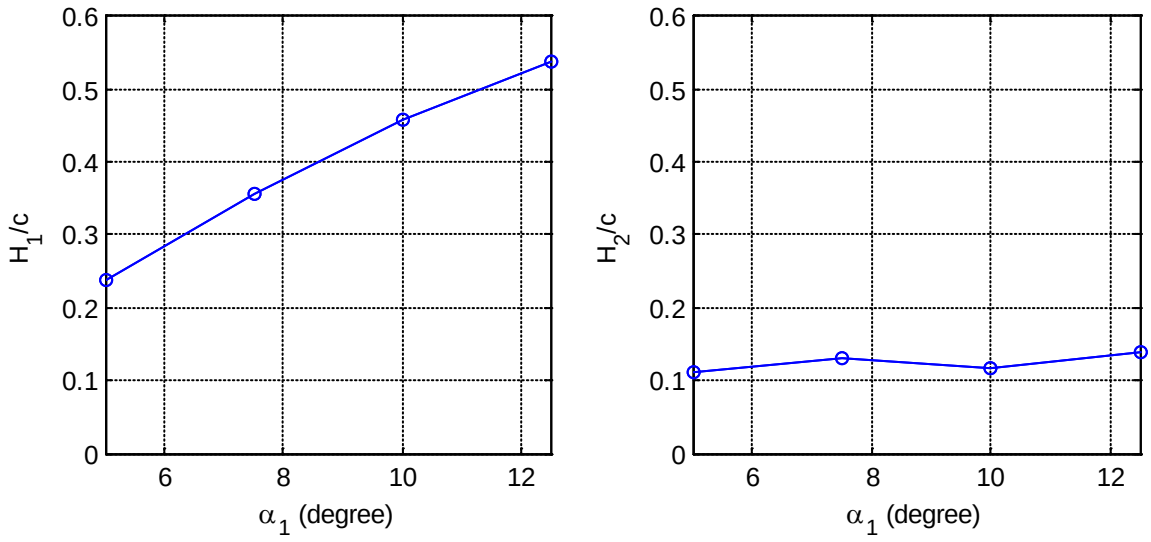

Figure 36 - Predicted primary and first harmonic wave heights, H_1 and H_2, at *x* = 8 m, as a function of pitch angle for two-hydrofoil wave generation based on superposition of single hydrofoil wave generation simulations. (Note $\alpha_2 = -\alpha_1$)

7.1.2. URANS Predicted Characteristics of Generated Wave Field

URANS simulation were completed for pitch angle combinations of α_1 = 5° and α_2 = -5°, α_1 = 7.5° and α_2 = -7.5°, α_1 = 10° and α_2 = -10°, and α_1 = 12.5° and α_2 = -12.5°. To demonstrate the unsteady flow field the two-hydrofoil model is subject to as it rotates, contours of velocity in a stationary frame are plotted in Figure 37 at specific instances in time throughout the final revolution for α_1 = 10° and α_2 = -10°. As both the positively and negatively pitched hydrofoils approach and pass under the free surfaces, major changes can be seen in the velocity field surrounding the hydrofoil. The velocity contours demonstrate that the radial variation of the hydrofoil's trailing edge results in the leading edge of both hydrofoils operating directly in the wake deficit left behind from the other hydrofoil. As noted during the single hydrofoil simulations, hydrofoils with a negative pitch angle push the free surface up as they pass underneath (see Figure 37 a)), whereas hydrofoils with a positive pitch angle pull the free surface downward(see Figure 37 e)).

The temporally varying free surface topologies for the previously mentioned pitch angle combinations are measured at x = 8 m and shown in Figure 38. Comparing the CFD results of Figure 38 to the predicted free surface topologies contained in Figure 35, illustrate that the URANS generated wave field compares well with the trends of the predicted free surface topology. However upon closer inspection significant differences were noted indicating that the flow field is non-linear with significant interactions between the hydrofoils. It was predicted, that at maximum pitch angles of α_1 = 12.5° and α_2 = -12.5°, the free surface would see fluctuation up to η/c = 0.60 but the URANS fluctuations were found to be less than η/c = 0.40, suggesting that generated wave heights are less than predicted.

The over prediction of free surface fluctuations can be correlated to the velocity fields shown in Figure 37. For single hydrofoil wave generation, each hydrofoil operated near its own wake deficit, but due to differences in the leading edge and trailing edge radial position the hydrofoil did not operate directly in its own wake when the absolute value of pitch angle was greater than 5°. The wake also had a full period to dissipate before interacting with the hydrofoil again. However, when a second hydrofoil of opposite pitch angle is added to the system, the leading edge of each hydrofoil operates directly in the wake deficit of the opposing hydrofoil. This, combined with the fact that the wake only has half a period to dissipate before encountering the next hydrofoil resulted in each hydrofoil seeing a completely different flow field than it did when operating as a single hydrofoil system. The change in flow fields seen by the rotating hydrofoils is something that cannot be predicted by the super position approach (as it is a physical change in operating conditions). The impact this change has on the device performance will be investigated further in this chapter.

As previously discussed in section 5.1.1, an ideal CycWEC would have no up-wave effects resulting from its operation, the free surface topology shown in Figure 39 suggests the presence of a small amplitude disturbance travelling in the up-wave direction with that same period as the rotating hydrofoils. This will reduce the wave generation efficiency of the device, but since the amplitude of the peak-to-peak up-wave disturbance was an order of magnitude smaller than that of the down-wave disturbance its effect will be small.

To illustrate in detail the characteristics of the generated wave field down-wave a FFT was performed on the free surface topologies shown in Figure 38. The results are

summarized in Figure 40 for the four tested pitch angle combinations. The FFT showed that the only significant waves generated were the primary wave, having a period equal the device and the first harmonic wave, having a period equal to half the device period. The primary wave height, H_1, constantly increased as α_1 increased reaching a non-dimensional wave height of H_1/c = 0.3562 when α_1 = 12.5°. The secondary wave height, H_2 consistently decreased as α_1 increased reaching a minimum non-dimensional wave height of H_1/c = 0.0218 when α_1 = 12.5°. Based on these results, the ratio of H_1/H_2 increased from 2.12 to 16.34 as the pitch angle increased from α_1 = 5° to α_1 = 12.5°. This agrees with the conclusions of Siegel and al. [11], which found the first harmonic from each hydrofoil cancels and a regular wave field having a period equal to the rotational period of the device is generated. Comparing the URANS predicted wave heights to the estimates based on superposition found that estimated wave heights were on average 51.6% and 231.1% larger than the URANS simulation results for H_1 and H_2, respectively.

Examining the resulting primary and secondary phase angles, also shown in Figure 40, concluded that, like the single hydrofoil simulations, the phase angle of the primary wave varies little with pitch angle. Meanwhile larger fluctuations were noted for the secondary phase angle as the pitch angle increased.

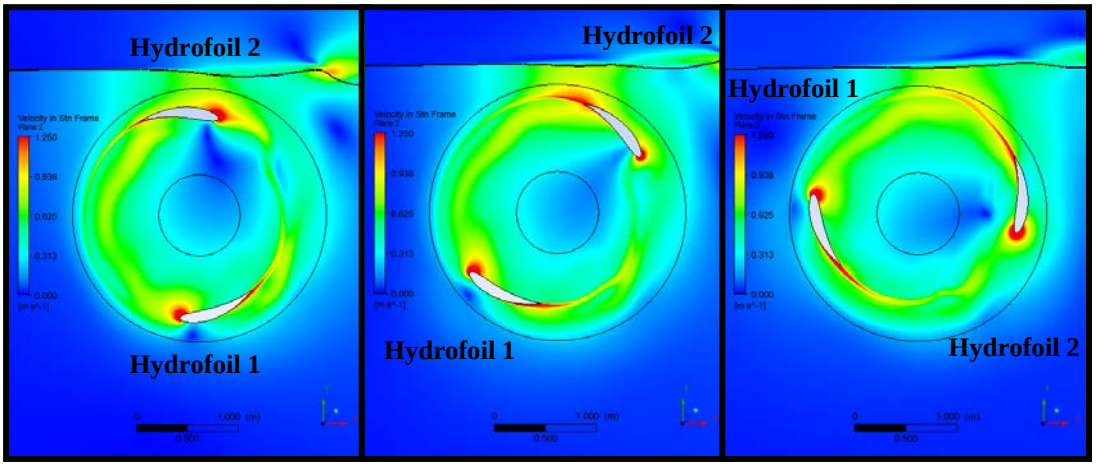

a) t/T_{std} = 23 b) t/T_{std} = 23.125 c) t/T_{std} = 23.25

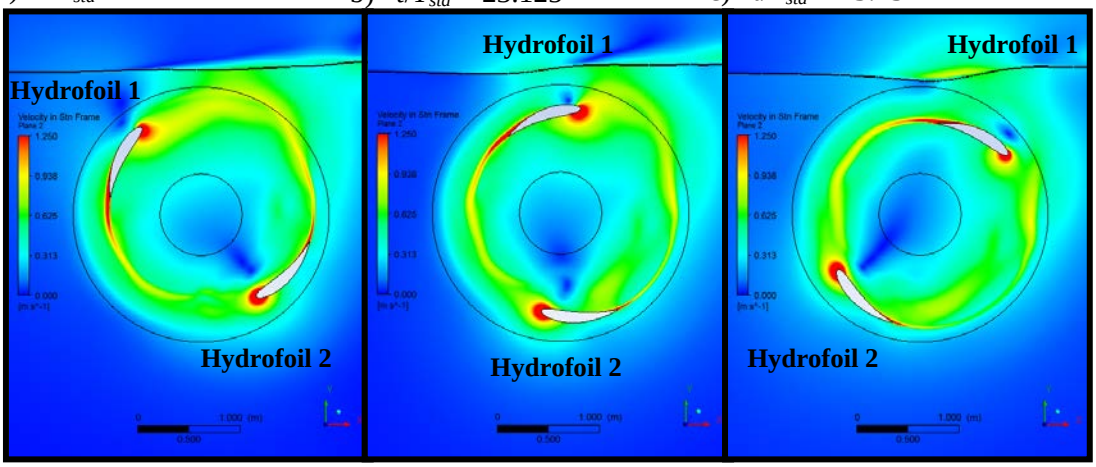

d) t/T_{std} = 23.375 e) t/T_{std} = 23.5 f) t/T_{std} = 23.625

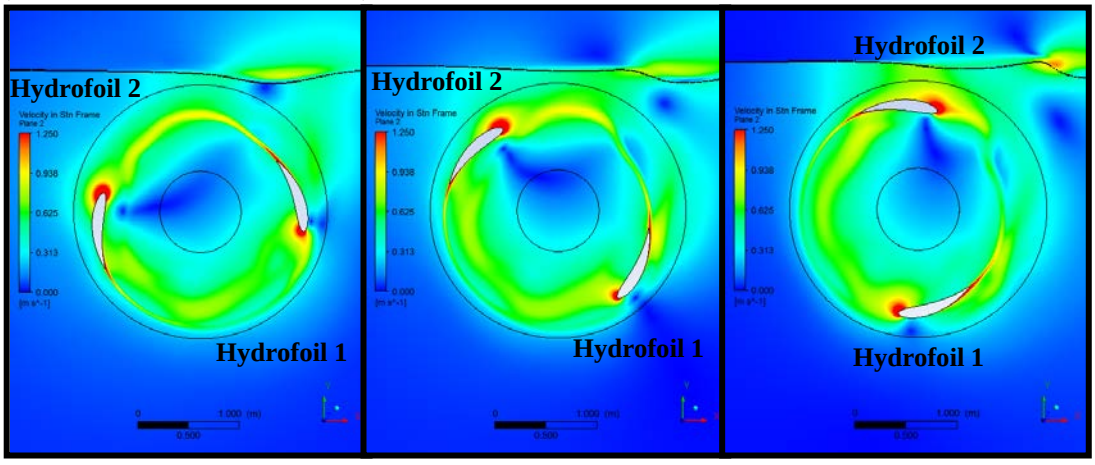

g) t/T_{std} = 23.75 h) t/T_{std} = 23.875 i) t/T_{std} = 24

Figure 37 - Velocity in stationary frame during the final revolution of α_1 = 10° (shown as Hydrofoil 1), α_2 = -10° (shown as Hydrofoil 2). The free surface is shown as a solid black line.

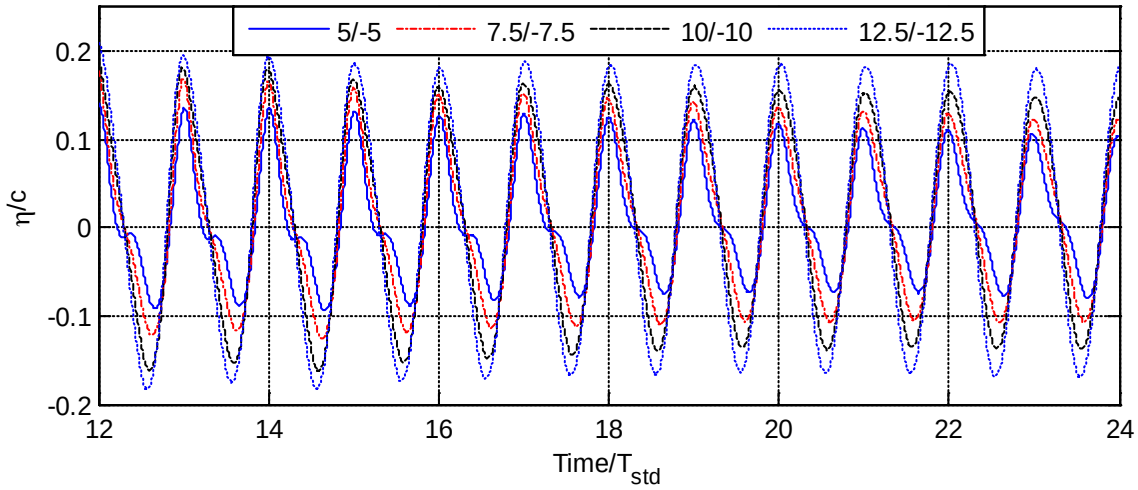

a) General view of free surface topology for two-hydrofoil wave generation at *x* = 8 m.

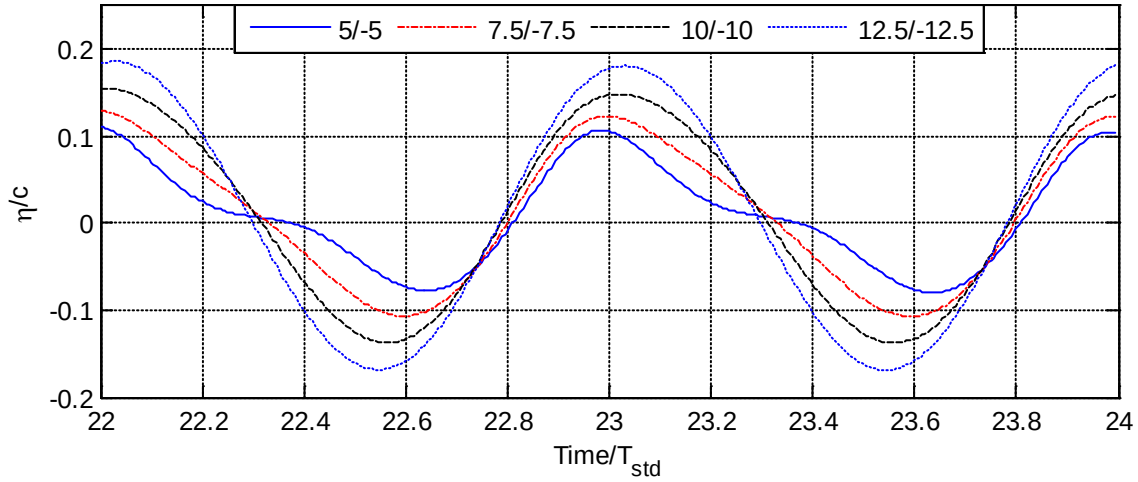

b) Detailed view of free surface topology for two-hydrofoil wave generation at *x* = 8 m.

Figure 38 - Free surface topology down-wave for two-hydrofoil wave generation simulations.

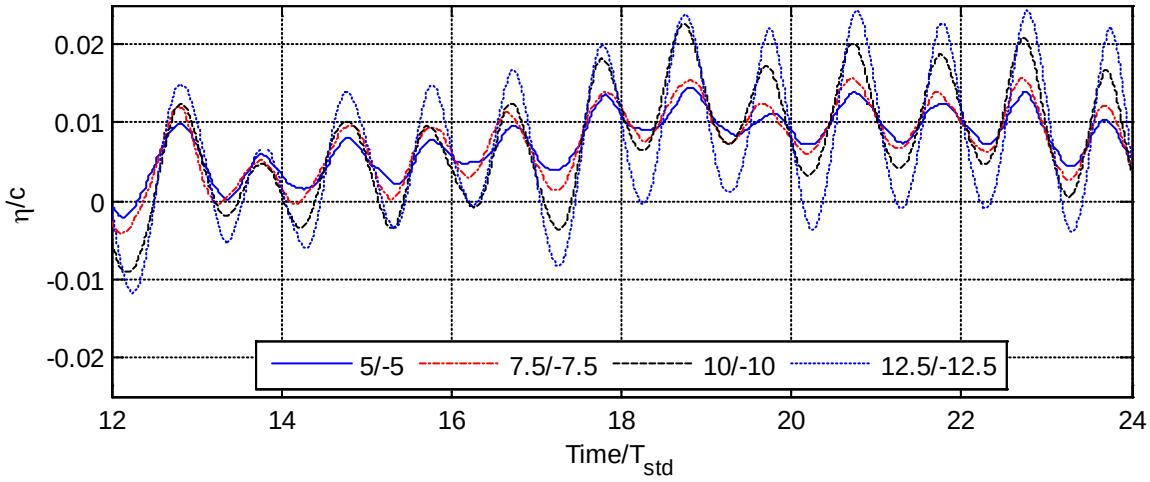

Figure 39 - Free surface topology up-wave at *x* = -8 m for two-hydrofoil wave generation simulations.

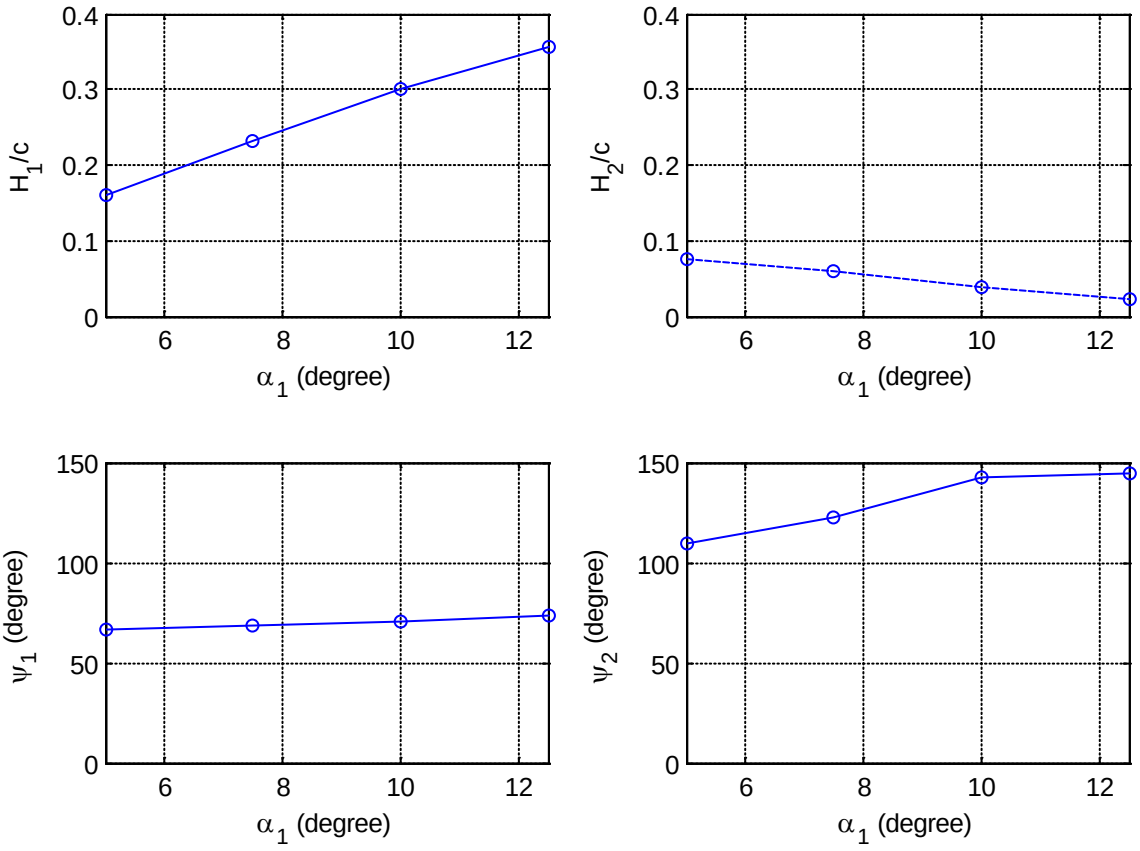

Figure 40 - Primary and secondary wave heights, H_1 and H_2, and phase angles, ψ_1 and ψ_2, as a function of pitch angle from two-hydrofoil wave generation measured at x = 8 m. (Note $\alpha_2 = -\alpha_1$)

7.1.3. Surface Pressure Distributions

The ability of the URANS simulations to predict the detailed flow field around the hydrofoil is advantageous when a device design change occurs, such as the addition of a second hydrofoil to the geometry, as the direct influence of this change can be analysed. To examined the surface pressure distributions for the two-hydrofoil wave generation simulations, C_p was calculated during the final revolution of each hydrofoil at θ = 0.88°, 90.88°, 180.88°, and 270.88° and plotted in Figure 41. As shown in Figure 41, the

stagnation pressure coefficient does not reach a value of $C_p = 1$ for any case due to the hydrofoils operating directly in an increased wake deficit resulting from the presence of the second hydrofoil. As shown previously in Figure 28, during single hydrofoil wave generation simulations, the stagnation pressure was reached for all pitch angles.

While there were variations in C_P with circumferential position for all pitch angles, the influence the additional hydrofoil had on the resulting C_P distributions in comparison to the single hydrofoil results depended on the sign of the pitched hydrofoil. For positive pitch angles, unlike the single hydrofoil results, significant fluctuations in C_P distribution were noted for all θ values. It was also found that at $\theta = 0°$ the C_P range along the upper and lower surface decreased by up to 35% compared to single hydrofoil results. The most intriguing finding for the positively pitched hydrofoils occurred at $\theta = 90°$, where difference between the minimum and maximum C_P along the hydrofoil surface was found to decrease by an average of 50% compared to the single hydrofoil results. For single hydrofoil results, no major change in surface pressure distribution was measured at $\theta = 90°$. It is unclear if the drop in lifting performance of the positively pitched hydrofoils is completely the due to the change in wake deficit, the hydrofoil operating in closer proximity to the free surface due to the larger amplitude wave that are generated, or a combination of the two.

Contrary to the positively pitched hydrofoils, for negative pitch angles C_P distributions did not significantly vary with θ, except near the free surface, where $\theta = 0°$. In addition, it was observed that at $\theta = 0°$ the minimum and maximum value of C_P decreased by approximately 50% and 75%, respectively, compared to single hydrofoil results. Due to

proximity of the hydrofoil to the free surface at this circumferential location it is difficult to determine if this change in device performance is due to hydrofoil's interaction with the free surface, the increased wake deficit, or both. It should be noted that the experimental findings of [23] only found drops in lifting performance of positively pitched hydrofoil as they neared the free surface but negative pitch angels were not investigated.

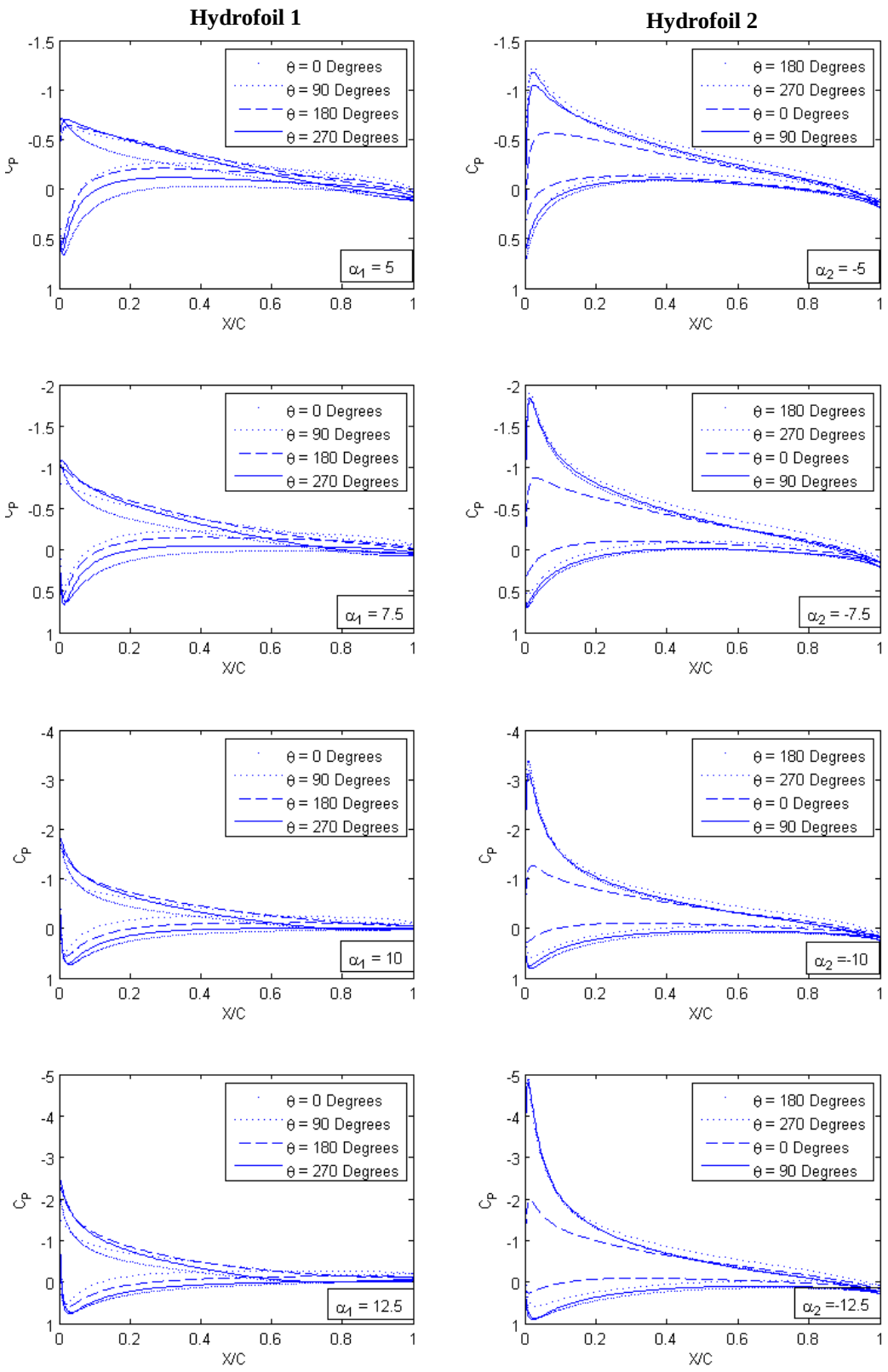

Figure 41 - Pressure coefficients along hydrofoil for two-hydrofoil wave generation.

7.1.4. Hydrodynamic Forces

To further examine the impact the addition of a second hydrofoil had on the near field flow field, the hydrodynamic forces acting on both hydrofoils were calculated. The radial and tangential force coefficients, C_R and C_T, are again calculated integrating the wall shear stress and the surface pressure along each hydrofoil surface. The unsteady body-fixed force coefficients are shown in Figure 42 and Figure 43 for each two-hydrofoil wave generation case. It should be noted that unlike the circumferential position of the hydrofoil, θ, which is measured in the global coordinate system, a revolution, as plotted along the x-axis in Figure 42 and Figure 43, is measured relative to the unique starting position of each hydrofoil. As a result, the positively pitched hydrofoil is, for example, at $\theta = 0°$ at the end of the 18^{th} revolution, while the negatively pitched hydrofoil is at $\theta = 180°$ after the exact same number of revolutions.

Figure 42 and Figure 43 demonstrates just how significant the variation in hydrodynamic forces are as pitch angle is changed. As was the case with the single hydrofoil wave generation results, as α_1 increased positively, C_R also increased positively indicating a net outward radial force. Whereas as α_2 increased negatively, C_R increased negatively indicating a net inward radial force. For the positively pitched hydrofoils, a sudden decrease in C_R was noted immediately after the hydrofoil passed under the free surface and continued until it reached a local minimum near the quarter revolution point (i.e., $\theta = 90°$). This is similar to the trend noted during single hydrofoil wave generation. This decrease in radial force can be directly correlated to the 50% decrease in C_P range between the hydrofoil's upper and lower surface that was noted in Figure 41 at the same circumferential position.

When C_R was examined for the negatively pitched hydrofoils, the results illustrated that $|C_R|$ was a minimum after the hydrofoil passed under the free surface where $\theta = 0°$. The circumferential location of this minimum is a direct result of the decrease in C_P variation between the upper and lower surface on negatively pitched hydrofoils, which was shown in Figure 41. As was the case with the single hydrofoil results, this minimum was followed by a sudden increase $|C_R|$ until the maximum $|C_R|$ was reached, at $\theta = 90°$. It is also evident from Figure 42 that $|C_R|$ remained near this maximum value from $\theta = 90°$ to $\theta = 270°$, which also directly correlates with previously presented pressure distributions, that showed minimal changes in C_P distribution for these θ values.

By examining distributions of C_T it can be concluded that overall trends are the same as the single hydrofoil wave generation results. The variation of C_T had the same range as single hydrofoil results and the location of the local maximum and minimum remained the same. However, the maximum $|C_T|$ decreased for all pitch angles, indicating that operating the two-hydrofoil model in an increased wake deficit resulted in a drop in total tangential force per revolution.

Several important facts were uncovered upon closer inspection of the maximum and minimum values for $|C_R|$ and $|C_T|$. For positively pitched hydrofoils the minimum and maximum in $|C_R|$ were found to decrease by approximately 45 and 25 percent, respectively, when compared to the single hydrofoil wave generation results while, for negatively pitched hydrofoils the minimum and maximum of $|C_R|$ decreased by approximately 50 and 15 percent. As a result of the range of $|C_R|$ throughout a revolution on average increased by over 40% and 200%, respectively, for positive and negative

pitched hydrofoils, and thus are significantly more variable than the single hydrofoil simulation results.

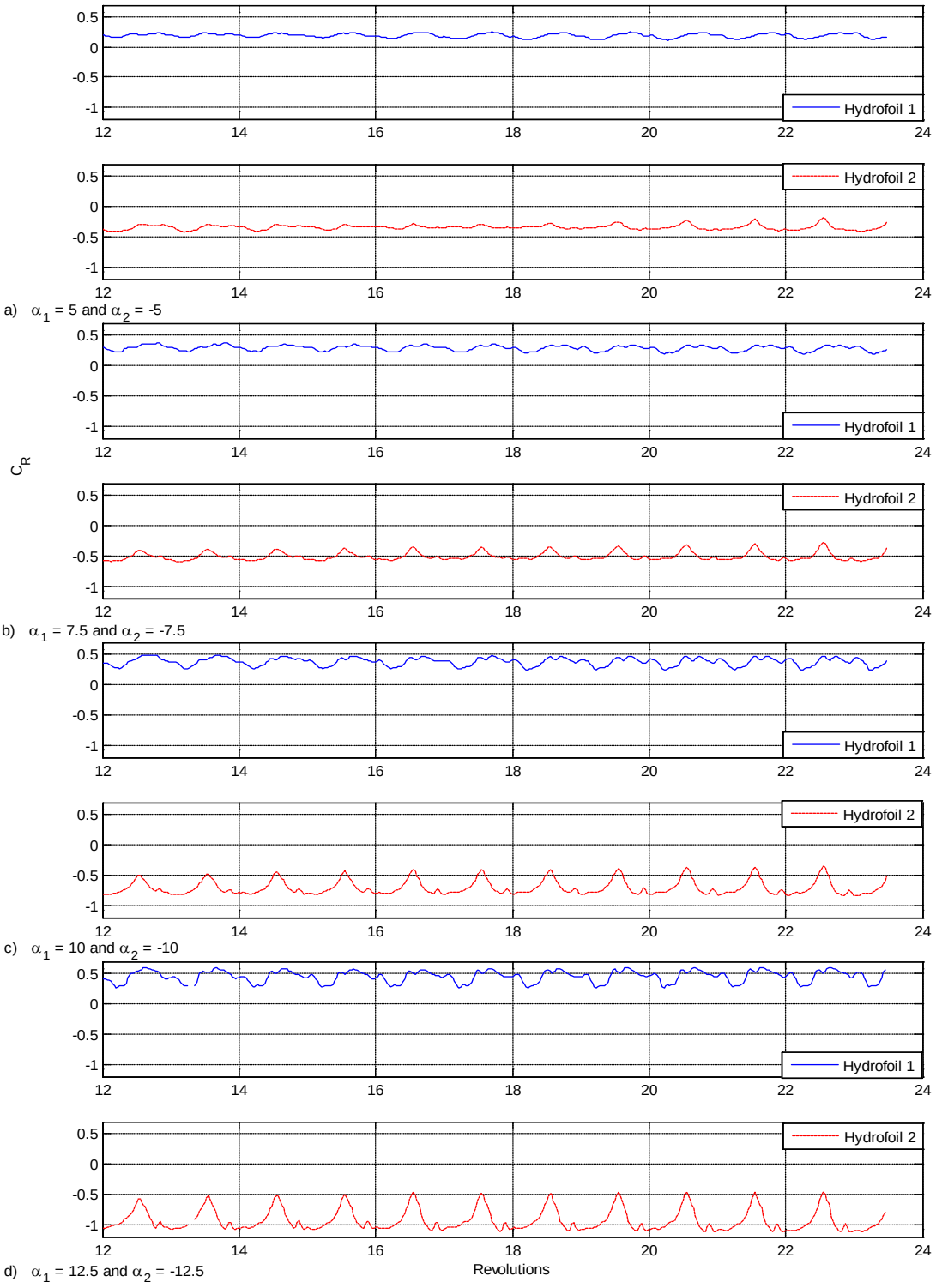

Figure 42 - Hydrofoil body-fixed radial force coefficients from two-hydrofoil wave generation for four combinations of α_1 and α_2 combinations.

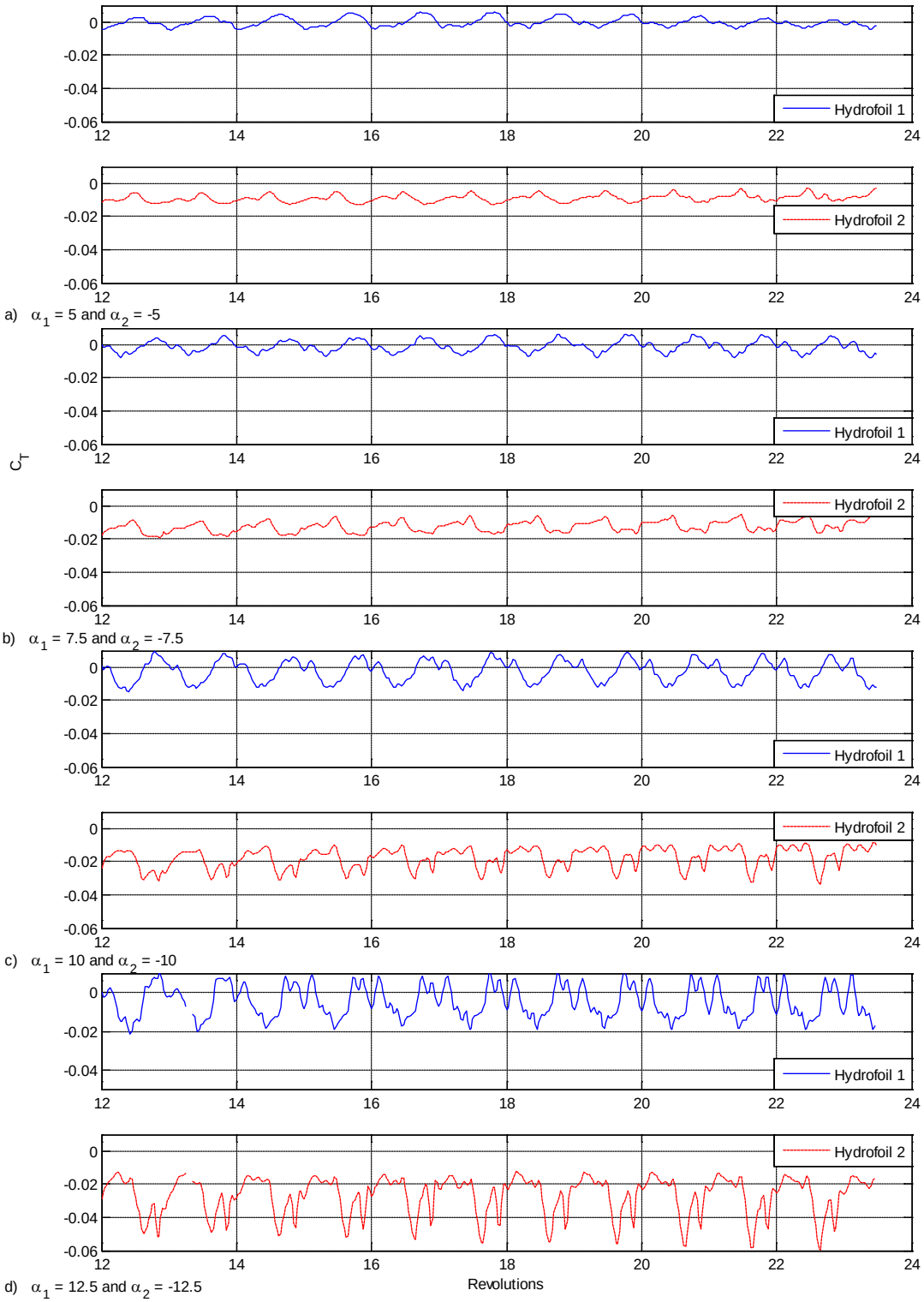

Figure 43 - Hydrofoil body-fixed tangential force coefficients from two-hydrofoil wave generation for four combinations of α_1 and α_2 combinations.

7.1.5. Wave Generation Efficiency

An important parameter to examine when developing a wave terminating energy extraction device, such as the CycWEC examined in this research, is the wave generation efficiency. A device that can generate a wave with minimum viscous losses will conversely perform better when operating as an energy extracting device.

The average power per unit width of the generated wave fields are shown in Figure 44 for the four wave generation cases simulated. The average power of the primary wave and its two first harmonics are defined as $\bar{E}_1$, $\bar{E}_2$, and $\bar{E}_3$, respectively, and the average total wave power of the generated wave field is defined as $\bar{E}_T$. Note the average power per unit width is calculated as per equation (2).

Since the average power per unit width is proportional to square of the wave height, the primary wave heights generated by the two-hydrofoil model contain a large quantity of the total power in the wave field. Using the wave heights shown in Figure 40 it was calculated that $\bar{E}_1$ accounts for 90.0%, 96.8%, 99.2% and 99.8%, respectively, of the total wave power, as the pitch angle is increased from α_1 = 5° to α_1 = 12.5°. As shown in Figure 44, $\bar{E}_T$ increases approximately linearly with pitch angle from $\bar{E}_T$ = 38.27 W/m when α_1 = 5° to $\bar{E}_T$ = 171.8 W/m when α_1 = 12.5°.

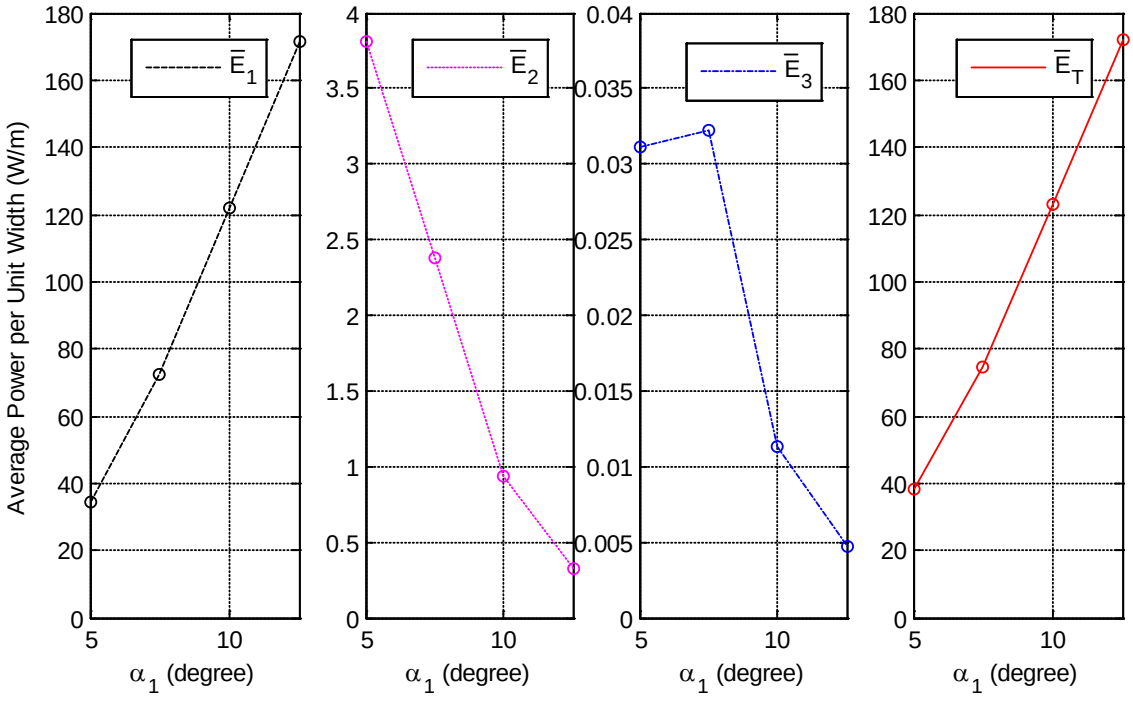

Figure 44 - Average power per unit width for primary wave, first two harmonics, and total wave power. (Note $\alpha_2 = -\alpha_1$)

Knowing the average power per unit width for the generated wave field is the first step in determining the wave generation efficiency of the device. The final step is quantifying the amount of power per unit width required to drive the two-hydrofoil rotating system that created the generated wave fields. The required power per unit width, referred to as the shaft power per unit width, is first calculated for each hydrofoil in the system as the product of the tangential force per unit width, the constant rotational speed (i.e., ω = 2.503 rad/s), and the radius of the rotational path of the hydrofoil (i.e., R = 1 m). The total shaft power per unit width, E_{Shaft}, is simply the sum of the shaft power per unit width of the two hydrofoils.

The required instantaneous shaft power as a function of circumferential position is shown in Figure 45 for each hydrofoil. The average total wave power per unit width, $\bar{E}_T$,

of the generated wave fields was included for comparison to the total average shaft power per unit width, $\bar{E}_{Shaft}$, which was calculated by integrating E_{Shaft} throughout one revolution. Figure 45 illustrates that the difference between $\bar{E}_T$ and $\bar{E}_{Shaft}$ decreased as pitch angle is increased, suggesting an increase in device wave generation efficiency. Figure 45 also demonstrates how the negatively pitched hydrofoils have a much larger power requirement compared to the positively pitched hydrofoils to rotate at the same angular velocity.

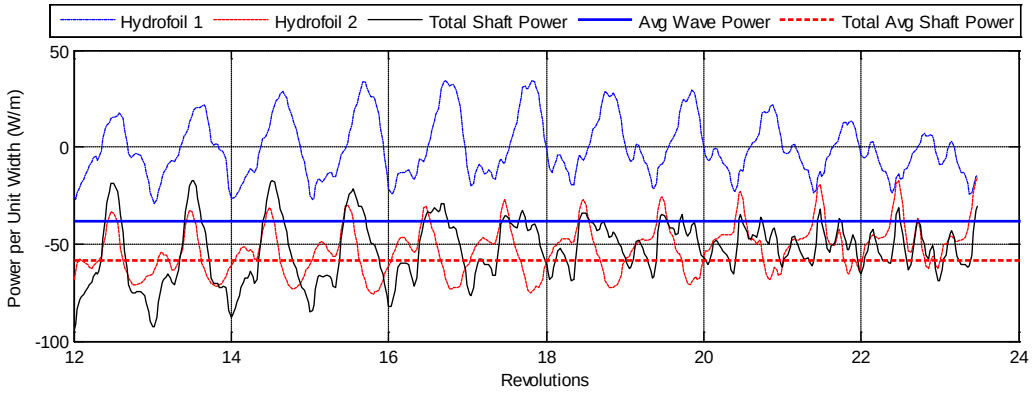

a) α_1 = 5 and α_2 = -5

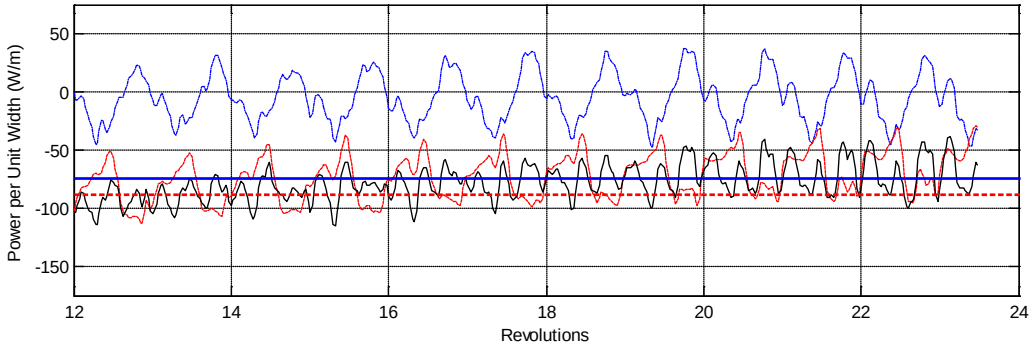

b) α_1 = 7.5 and α_2 = -7.5

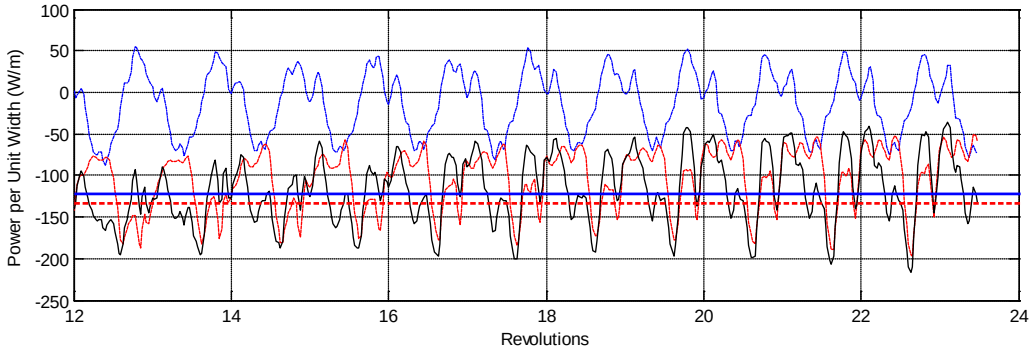

c) α_1 = 10 and α_2 = -10

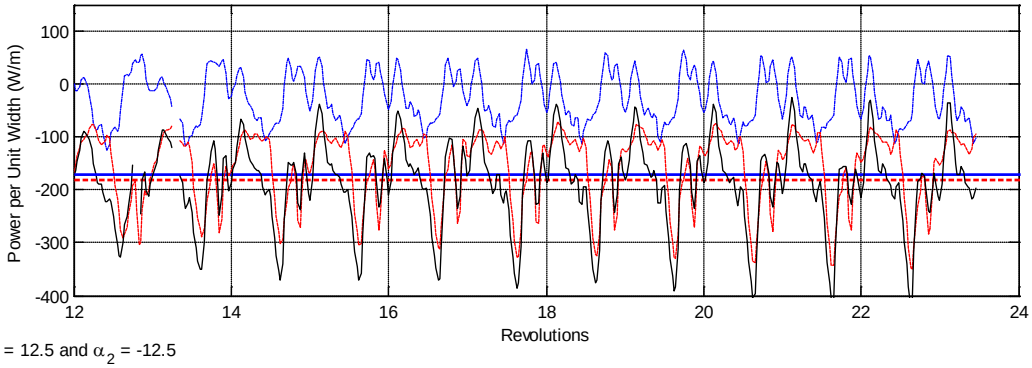

d) α_1 = 12.5 and α_2 = -12.5

Figure 45 - Required shaft power and average wave power for two-hydrofoil wave generation.

Total average shaft power per unit width, was compared to the total average power of the generated wave field down-wave to provide the average wave generation efficiency, ε_G, of the device which is defined as:

$$\varepsilon_G = \frac{\overline{E}_T - \left|\overline{E}_U\right|}{\overline{E}_{Shaft}}. \tag{20}$$

where $\bar{E}_U$ is the average up-wave wave power per unit width generated by the CycWEC, an inefficiency of the device that was determined from Figure 39. The average wave generation efficiency was calculated for the four completed wave generation simulations and the results are summarized in Table 3. The results show a major increase in wave generation efficiency as the pitch angle is increased from ε_G = 65.17% when α_1 = 5° to ε_G = 93.95% when α_1 = 12.5°. Combined with the fact that when α_1 = 12.5° the primary wave accounts for over 99% of the total wave power, meaning that over 90% of the shaft power input into the rotational system is transformed into $\bar{E}_1$ which is desired for an optimal wave energy extraction.

Table 3 - Wave generation efficiency for two-hydrofoil wave generation.

Two Hydrofoil Wave Generation Statistics						
Simulation #	α_1	α_2	$\bar{E}_T$	$\bar{E}_U$	$\bar{E}_{Shaft}$	ε_G
	(deg)	(deg)	(W/m)	(W/m)	(W/m)	%
1	5	-5	38.32	0.04	58.74	65.17
2	7.5	-7.5	74.79	0.09	88.69	84.23
3	10	-10	122.83	0.26	133.19	92.03
4	12.5	-12.5	171.83	0.63	182.23	93.95

7.2. Wave Cancellation Simulations

The final stage of the research involved using URANS predictions to test the wave cancellation abilities of the two-hydrofoil CycWEC model. These simulations encompassed elements of all stages of the research, such as the required grid and time step parameters from the preliminary single hydrofoil research, the numerical wave generation capabilities of the mass source region, and information from the two-hydrofoil wave generation results to correctly configure the mass source strength of the incident wave field.

The wave cancellation properties of the two-hydrofoil model was first tested with pitch angles of α_1 = 7.5° and α_2 = -7.5°, for two difference user defined incident wave heights. The first simulation, referred to as Case 1, had an incident wave height defined based on the primary wave heights measured during the two-hydrofoil wave generation simulation. The second simulation, referred to as Case 2, had a prescribed incident wave height nearly 15% less than Case 1. Final simulations included single tests for pitch angles of α_1 = 10° and α_2 = -10°, and α_1 = 12.5° and α_2 = -12.5° and were referred to as Case 3 and 4, respectively. The prescribed incident wave heights for Cases 3 and 4 were defined using the same manner as Case 1. Note the wave cancellation simulations were ended after 3600 time steps, or 45.18 seconds due to the heavy computational requirements for these simulations. Having completed 4800 times steps for Case 1, no new information arose during the final 1200 time steps so the remaining cases were assigned a shortened total run time. The reduced total run time also permitted the completion of multiple wave cancellation simulations.

7.2.1. Characteristics of the Generated Wave Field

To test the wave cancellation abilities of a two-hydrofoil CycWEC model, a fundamental requirement is to generate an appropriate incidence wave field to interact with the device. For Cases 1-4, the mass source term was defined to produce an incident wave field with wave heights of H_A/c = 0.2684, 0.2314, 0.3528, and 0.4127, respectively. Required phase shifts were also input into the mass source term based on two-hydrofoil wave generation findings.

The resulting free surface topology measured at x = -4 m are shown in Figure 46 for all cases. FFT analysis of the free surface revealed that mass source zone performed as designed, generating the desired incident wave field within 2.5% and 0.5% of the prescribed incident wave height and phase shift, respectively. The fluctuations in free surface topology illustrated in Figure 46 are due to an inefficiency in the converter generating a wave propagating in the up-wave direction as these fluctuations were not found when the mass source was tested individually. The disturbance had a mean measured wave height of H/c equal to 8.8% of H_A/c. This up-wave disturbance will be accounted for when analyzing the overall efficiency of the device.

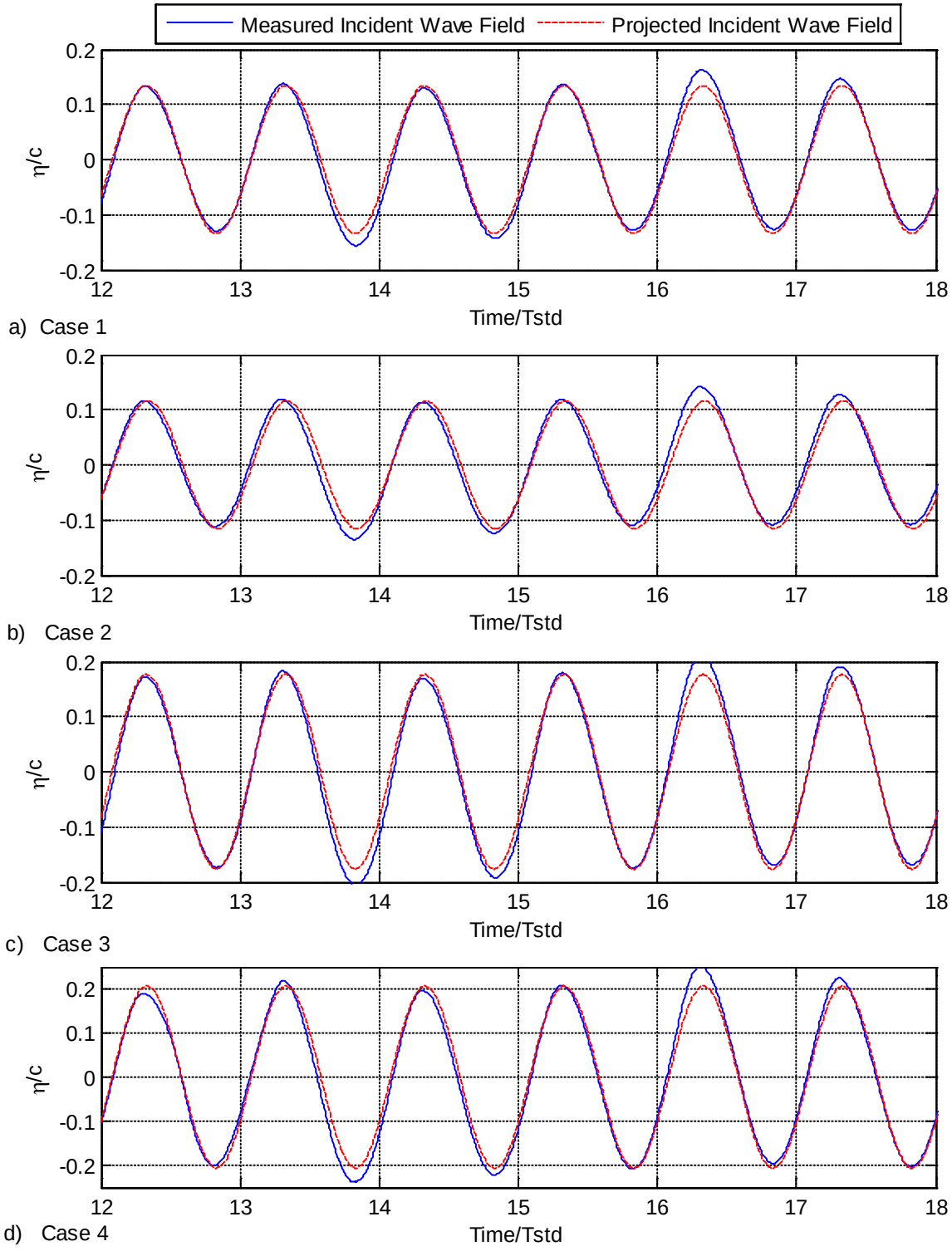

Figure 46 - Free surface topology up-wave at *x* = -4 m for wave cancellation simulations.

7.2.2. Characteristics of the Cancelled Wave Field

The remaining wave field down-wave at x = 8m is examined in this section for all cases. If complete wave cancellation occurred an undisturbed free surface would be expected in the down-wave direction relative to the CycWEC. As shown by the temporal free surface variations measured at x = 8 m in Figure 47, this unfortunately was not the case as a quantifiable down-field wave field remained. However, comparing the wave cancellation results of Figure 47 to the projected undisturbed incident wave field, significant amounts of power were extracted from the wave field because the average wave power is proportional to H^2. Closer examination of the free surface topologies for Case 1 and 2 suggests that Case 1 had less of a down-wave wave field remaining compared to Case 2, even with a 15% larger incident wave field.

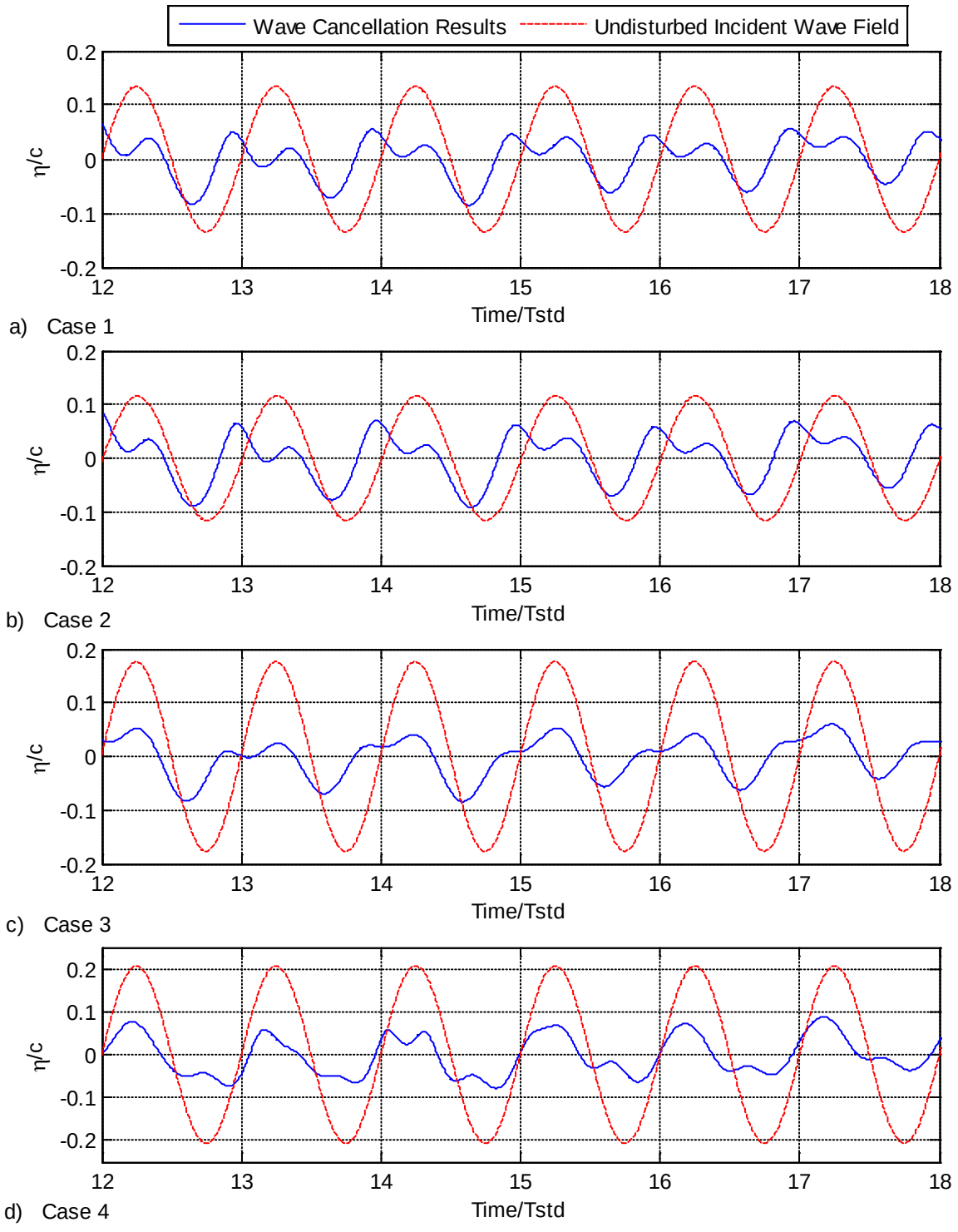

Figure 47 - Free surface topology down-wave for wave cancellation simulations at x = 8 m.

To complete the analysis of the down-field wave field a FFT was applied to the free surface topologies. The FFT analysis showed that the down-wave free surface topology consisted of the primary wave and the first and second harmonic. The resulting wave heights of each component wave was determined and are shown in Figure 48 along with the incident wave height, H_A/c, for each simulation. Comparing the incident and primary wave heights, which both have the same wavelength, indicate a major decrease in wave height for all cases. In terms of wave cancellation, the harmonics are inefficiencies; having smaller wavelengths then the incident wave, the harmonic waves are not able to cancel out the incoming incident wave field. As illustrated in Figure 48, as α_1 is increased the harmonic wave heights are found to decrease, supporting a preliminary assumption that as the pitch angles are increased so too will the device cancellation efficiency. Also shown in Figure 48 is that the decrease in device performance for Case 2 is because both H_1/c and H_2/c are larger in comparison to Case 1.

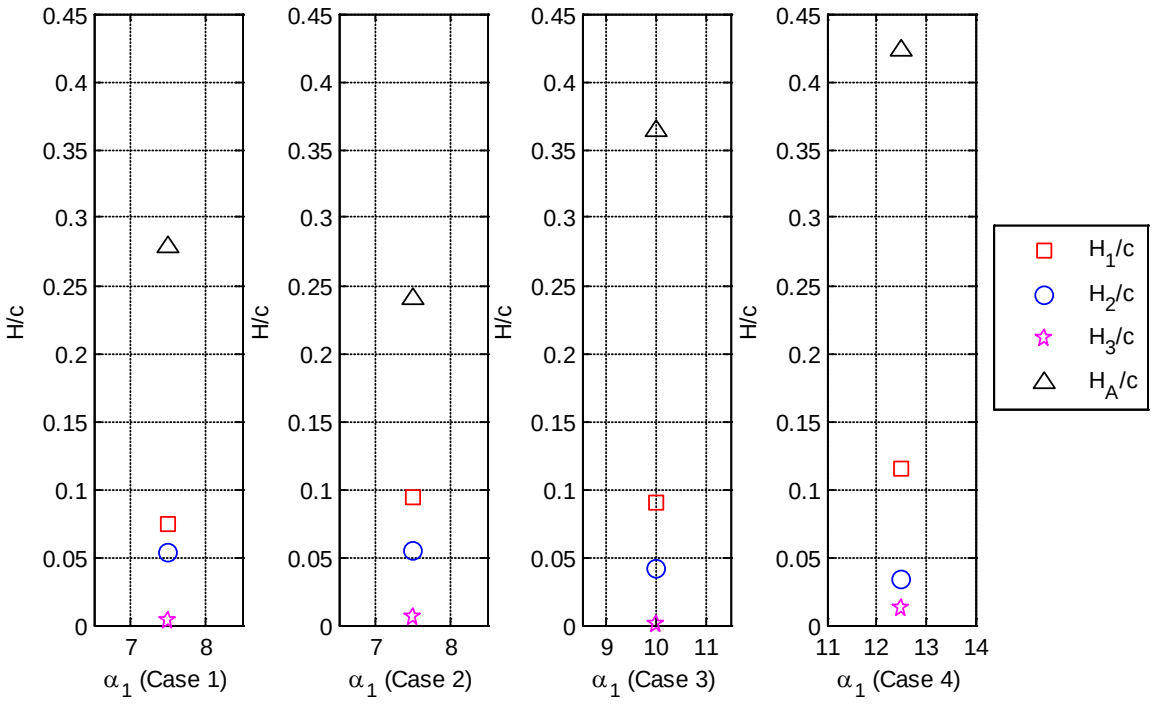

Figure 48 - Primary wave height, H_1, harmonic wave heights H_2 and H_3, incident wave height H_A as a function of pitch angle for wave cancellation, measured at x = 8 m. (Note α_2 = - α_1)

7.2.3. Surface Pressure Distributions

Surface distributions of C_p were calculated for each hydrofoil during the final revolution of each of the four cancellation simulations at θ = 0.88°, 90.88°, 180.88°, and 270.88° and the results are plotted shown in Figure 49. As illustrated in Figure 49, even when subject to an incident wave field, the stagnation pressure coefficient of C_p = 1 is still not reached, suggesting that hydrofoils still operate in an increased wake deficit.

When the two-hydrofoil CycWEC model operates in wave cancellation conditions major changes in the overall surface pressure distributions resulted compared to the wave generation results. Although minimal or no change was noted for the maximum C_p value for any pitch angle, the minimum C_p value on the suction side increased by over 200%

and 300%, respectively, for the positively and negatively pitched hydrofoils. For negative pitch angles it was determined the largest difference in pressure between the lower and upper surfaces occurred when $\theta = 90°$ and the smallest difference occurred when $\theta = 0°$. Interestingly it was determined for positive pitch angles that the largest difference in pressure on the lower and upper surfaces occurred when $\theta = 0°$ and was smallest when $\theta = 90°$. It should be noted that this completely opposes what was found during single hydrofoil wave generation research and experimentally by [23], which all suggested a drop in lifting performance of a positively pitched hydrofoil as it approached the free surface. However, it should be also noted that the velocity field induced by the incident wave is largest near the free surface and decreases exponentially with depth and this could be changing the local angle of attack on the hydrofoil in this region. A common point for all pitch angles was that minimal change in pressure distributions were noted between $\theta = 180°$ and $\theta = 270°$.

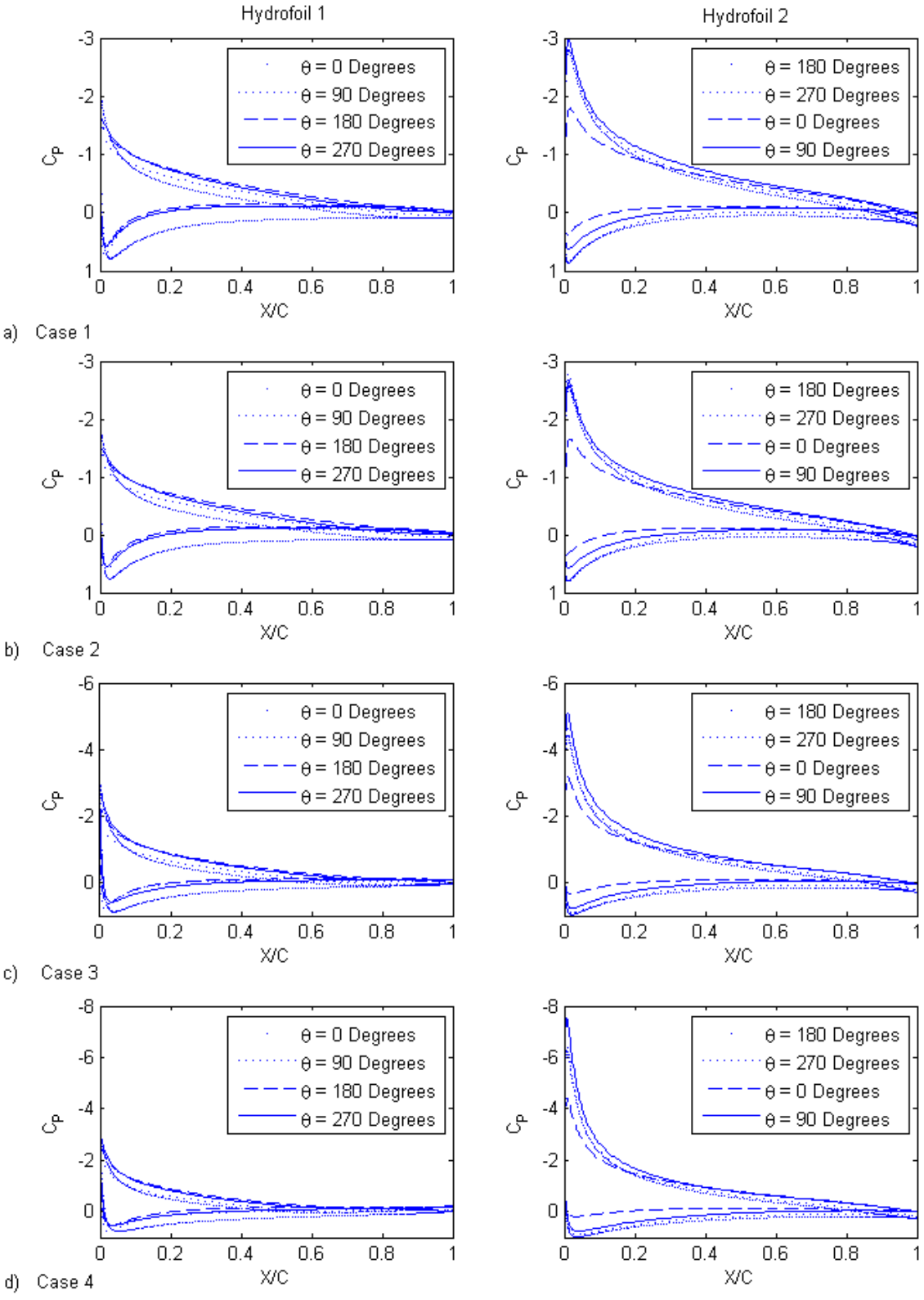

Figure 49 - Pressure coefficients along hydrofoil for two-hydrofoil wave cancellation.

7.2.4. Hydrodynamic Forces

The instantaneous body-fixed force coefficients C_R and C_T, are shown in Figure 50 and Figure 51, respectively, for each of the wave cancellation simulations. It should be noted once again that unlike the circumferential position of the hydrofoil, θ, which is measured in the global coordinate system, a revolution, as plotted along the x-axis in Figure 51, is measured relative to the unique starting position of each hydrofoil. As a result, the positively pitched hydrofoils are, for example, at $\theta = 0°$ at the end of the 18^{th} revolution, while the negatively pitched hydrofoil is at $\theta = 180°$ at the exact same time.

The radial force coefficient, C_R, shown in Figure 50 a), was determined to have significant differences from the C_R values obtained for the wave generation simulations. For both positively and negatively pitched hydrofoils the maximum, minimum, and mean values of $|C_R|$ increased in comparison to the wave generation results. This increase correlates well with the increased variation of surface pressure distribution between the upper and lower surfaces that was noted in the previous section.

For positively pitched hydrofoils, once C_R was at its maximum after the hydrofoil passed under the free surface (i.e., $\theta = 0°$), a sudden decrease in C_R occurred which continued until reaching its minimum near the quarter revolution point (i.e., $\theta = 90°$). For negatively pitched hydrofoils, however, the minimum $|C_R|$ occurred when $\theta = 0°$, which was followed by a sudden increase in $|C_R|$ that continued until reaching its maximum when $\theta = 90°$. C_R remained nearly constant from $\theta = 180°$ to $\theta = 0°$ for all hydrofoil pitch angles.

The tangential force coefficient, C_T, shown in Figure 51 clearly has one major difference then all other C_T plots. For the first time C_T values are consistently positive,

especially for positively pitched hydrofoils. This is a significant result as it indicates that the device is successfully being driven forward by the incident wave field, and therefore, extracting shaft power from the incident wave. In addition, the range of C_T was found to increase substantially, and thus C_T fluctuations were larger throughout each revolution. For the positive pitch angles it was noted that within each revolution the local maximum C_T value occurred just before or just after the hydrofoil passed below the free surface and the local minimum occurred when the hydrofoil was furthest away from the free surface. A brief decrease in C_T was also noted as the hydrofoil is directly under the free surface. For the negatively pitched hydrofoil the fluctuations of C_T were found to have a mean value near $C_T = 0$ because C_T was often negative during intervals of each revolution suggesting that this hydrofoil is not significantly contributing to the extracted shaft power.

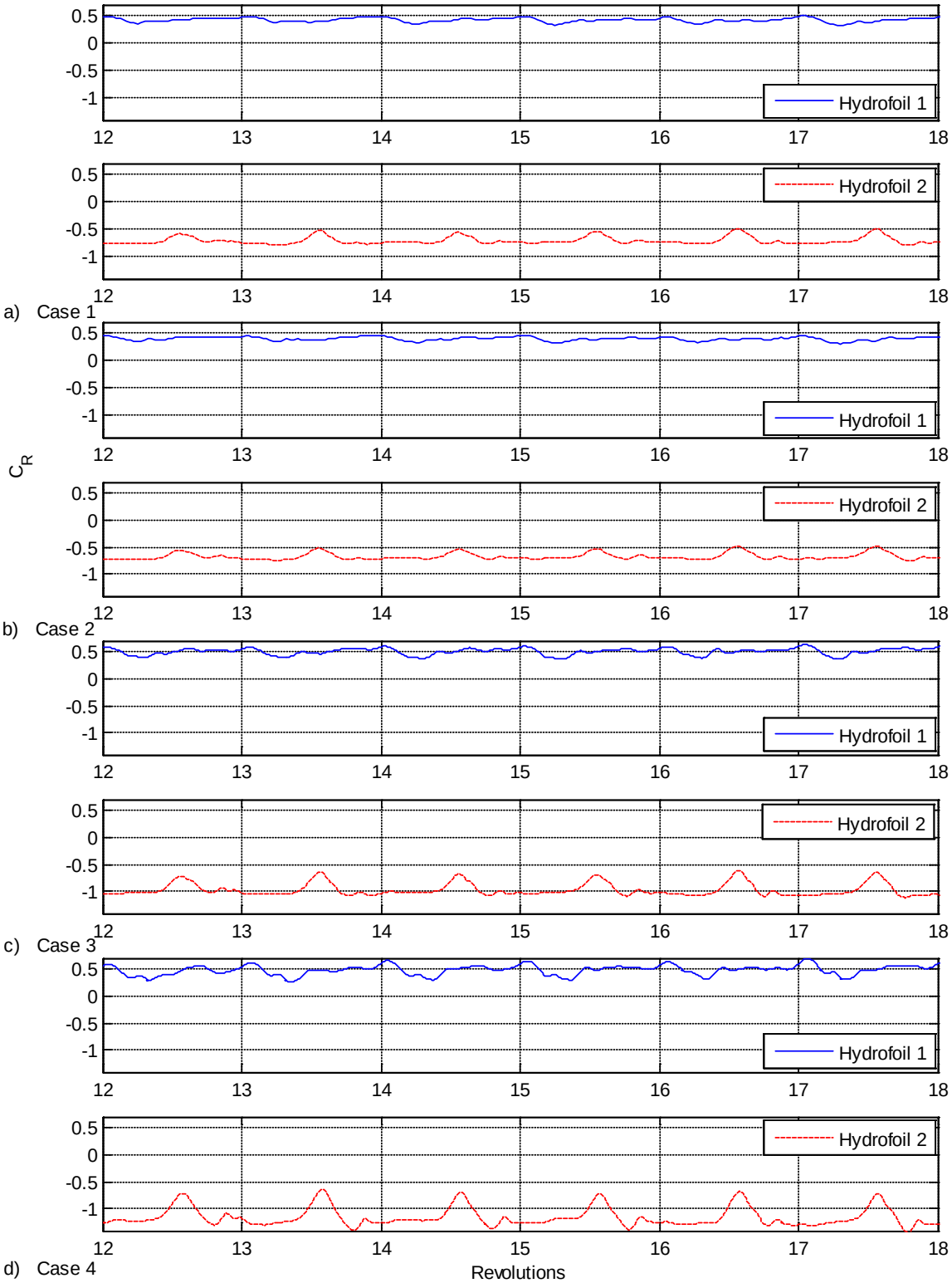

Figure 50 - Hydrofoil body-fixed radial force coefficients resulting from wave cancellation simulations.

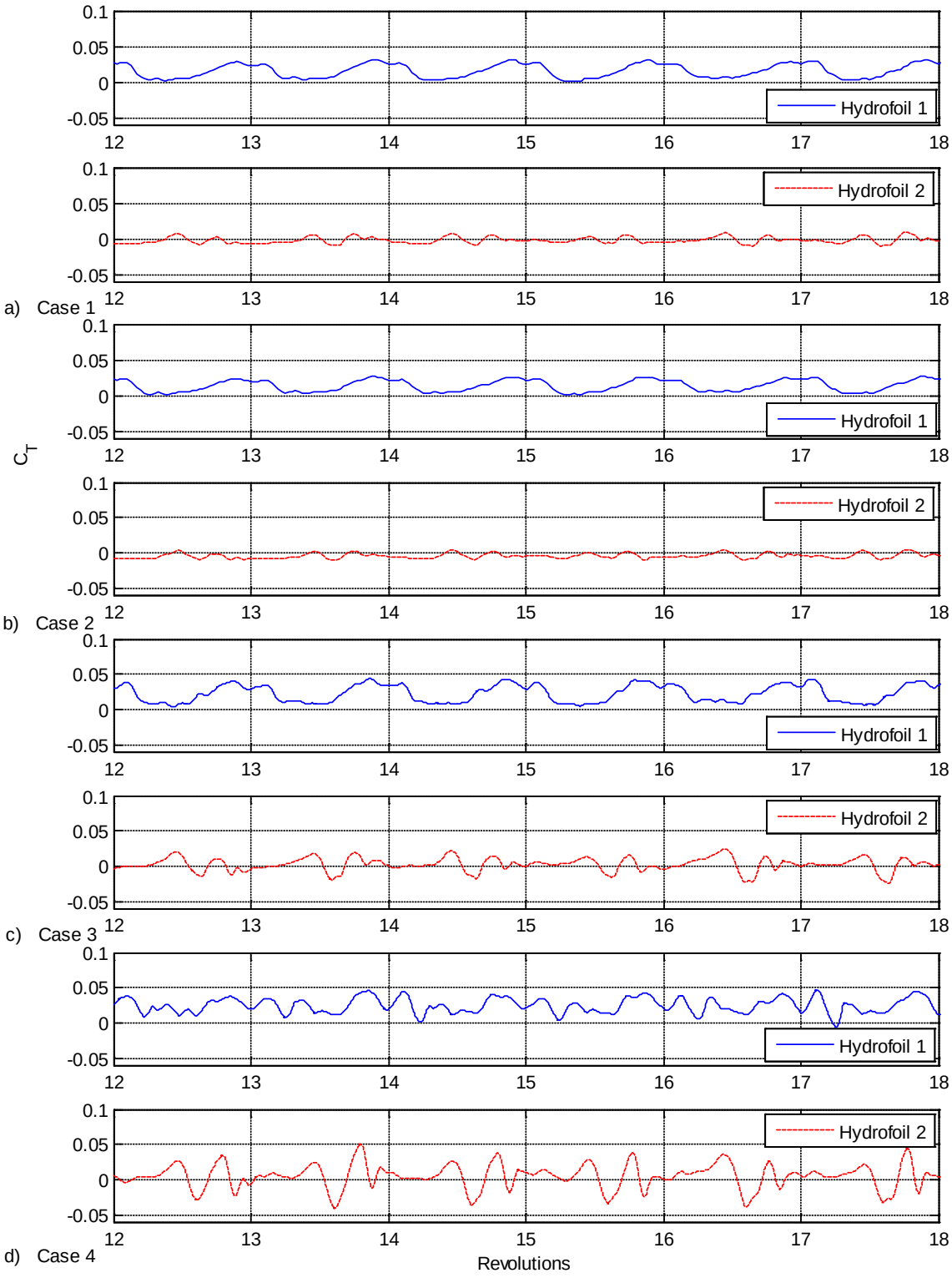

Figure 51 - Hydrofoil body-fixed tangential force coefficients resulting from wave cancellation simulations.

7.2.5. Average Wave Cancellation Efficiency

To quantify the wave cancellation ability of the two-hydrofoil CycWEC model the average wave cancellation efficiency was examined for each of the four simulations. This was accomplished by comparing the differences in wave power (due to energy extraction) between the undisturbed incident wave field, measured at x = -4 m, and the resulting wave field, measured at x = 8 m. Initially the average power per unit width of the primary wave, $\bar{E}_1$, and its two first harmonics, $\bar{E}_2$ and $\bar{E}_3$, remaining down-wave from the device at x = 8 m was calculated. The total average power of the remaining wave field per unit width, $\bar{E}_T$, is simply the summation of $\bar{E}_1$, $\bar{E}_2$, and $\bar{E}_3$. The average power for each down-wave wave component along with the total average wave power and the average power of the undisturbed incident wave per unit width, defined as $\bar{E}_A$, are shown in Figure 52. Clearly the device was able to cancel more power from the incident wave field when the hydrofoils were pitched at higher incident angles. To quantify the performance of the device the average wave cancellation efficiency, ε_{WC}, is defined as:

$$\varepsilon_{WC} = 1 - \frac{\left|\overline{E}_U\right| + \overline{E}_T}{\overline{E}_A} \tag{21}$$

where $\bar{E}_U$ is the average difference between the wave power per unit width of the undisturbed incident wave field and the resulting up-wave wave field at x = -4 m, as determined from Figure 46. The average wave cancellation efficiency was calculated for each cancellation cases using equation (21) and the results are summarized in Table 4. The wave cancellation efficiency was found to be the lowest when the hydrofoils were pitched to α_1 = 7.5° and α_2 = -7.5° and the incident wave height was reduced (i.e., Case

2). For Cases 1, 3, and 4 the wave cancelation efficiency of the device varied from 90% to 93%, suggesting that the two-hydrofoil CycWEC is an effective wave cancelling device when subject to an incident wave field of appropriate height, frequency, and phase.

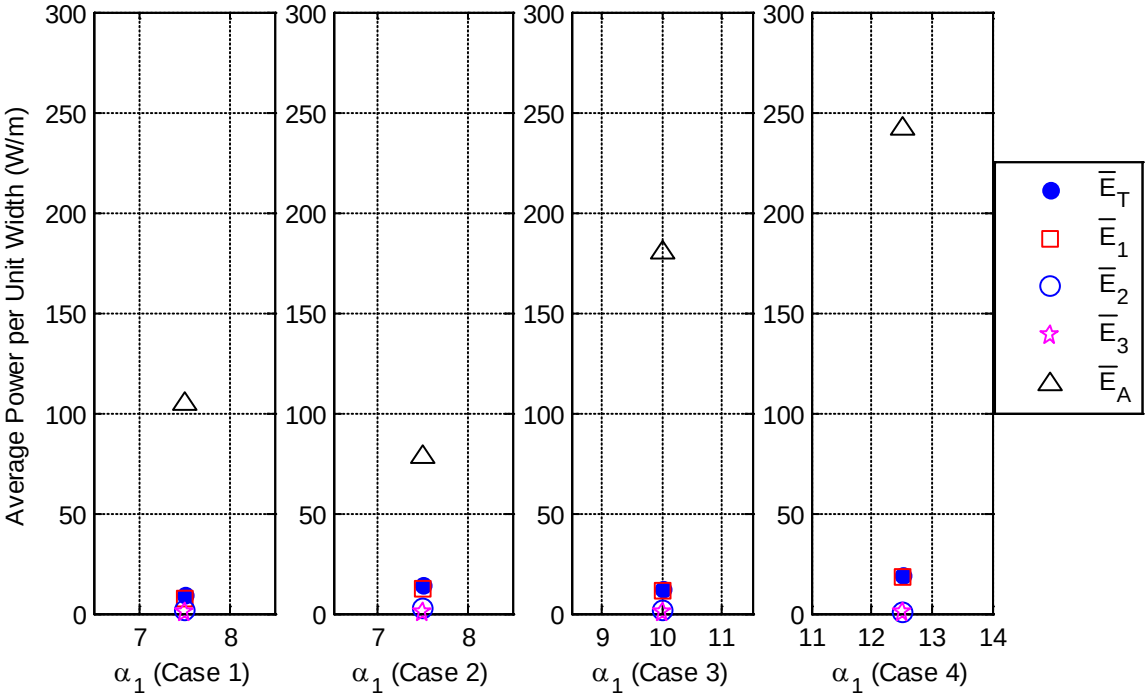

Figure 52 - Total average wave power, average power for primary wave, and first two harmonics, and average incident wave power for two-hydrofoil wave cancellation. (Note $\alpha_2 = -\alpha_1$)

Table 4 - Wave cancellation efficiency for two-hydrofoil CycWEC model.

Two Hydrofoil Wave Cancellation Efficiency Statistics						
Simulation #	α_1	α_2	$\bar{E}_T$	$\bar{E}_U$	$\bar{E}_A$	ε_{WC}
	(deg)	(deg)	(W/m)	(W/m)	(W/m)	%
1	7.5	-7.5	9.37	0.72	104.45	90.34
2	7.5	-7.5	14.01	0.84	77.78	80.91
3	10	-10	12.21	1.21	179.47	92.52
4	12.5	-12.5	18.79	1.47	241.83	91.62

7.2.6. Average Power Conversion Efficiency

Having a wave energy converter that cancels waves efficiently is important but is irrelevant if the device cannot convert the cancelled wave power into shaft power. To investigate the average power conversion efficiency, ε_{PC}, of the device several important parameters were required. Initially the required power per unit width, referred to as the shaft power per unit width, is calculated for each hydrofoil and the total shaft power per unit width, E_{Shaft}, is then calculated simply as the sum of the two. The fluctuations of the shaft power resulting from each hydrofoil and the total shaft power are shown in Figure 53. The average incident wave power per unit width, $\bar{E}_A$, was also included in Figure 53 to illustrate an ideal power conversion value for $\bar{E}_{Shaft}$, if all the incident wave power was converted to shaft power. Evidently there is major change compared to the two-hydrofoil wave generation shaft powers plotted previously in Figure 45. The total shaft power is now primarily positive throughout each revolution meaning that the incident wave field is driving the two-hydrofoil system forward and that wave power is successfully being converted to shaft power. However, it is important to note that the total shaft power is very close to the shaft power for the positively pitched hydrofoil. The difference in shaft power for the positively and negatively pitched hydrofoils suggest that although both hydrofoils are essential for incident wave cancellation, the power conversion efficiencies of the device are heavily dependent on the positively pitched hydrofoil. In fact, the hydrofoils with negative pitch angles were found to require shaft power for a short periods of time just as the hydrofoil passed under the free surface near θ = 0°. Fundamentally there would be a flaw in the CycWEC design if the total shaft power was constantly below zero and drawing power from the system. However, this is not the case

because positively pitched hydrofoils are constantly converting wave power into shaft power, keeping the total shaft power consistently above zero, except for brief instances in time for high pitch angles cases. Finally it should be noted that the point of peak power conversion for the positively pitched hydrofoils occurred near $\theta = 270°$ which is when the hydrofoil is closest to the incident wave field, and thus is the only time in its rotational that it is interacting with the undisturbed incident wave field.

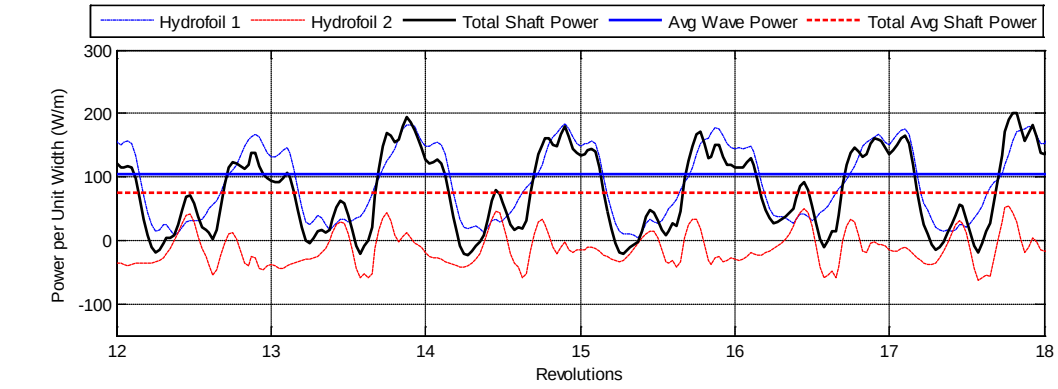

a) Case 1

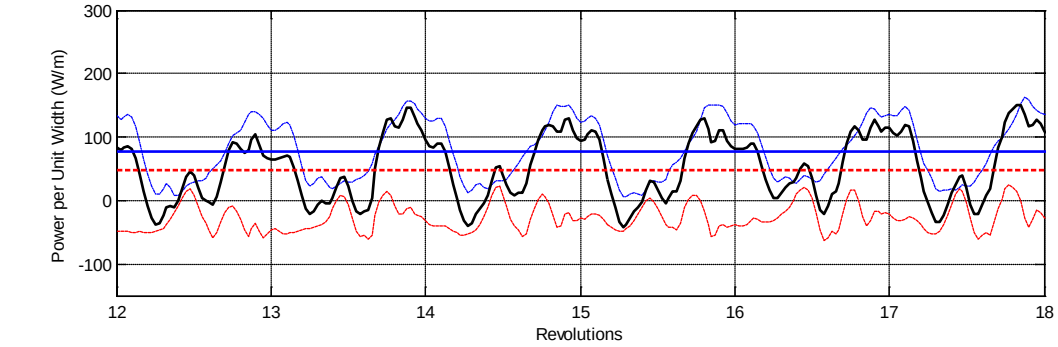

b) Case 2

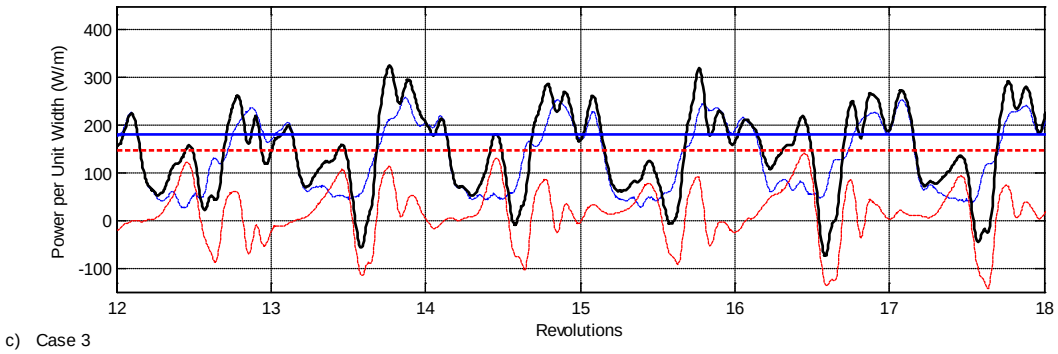

c) Case 3

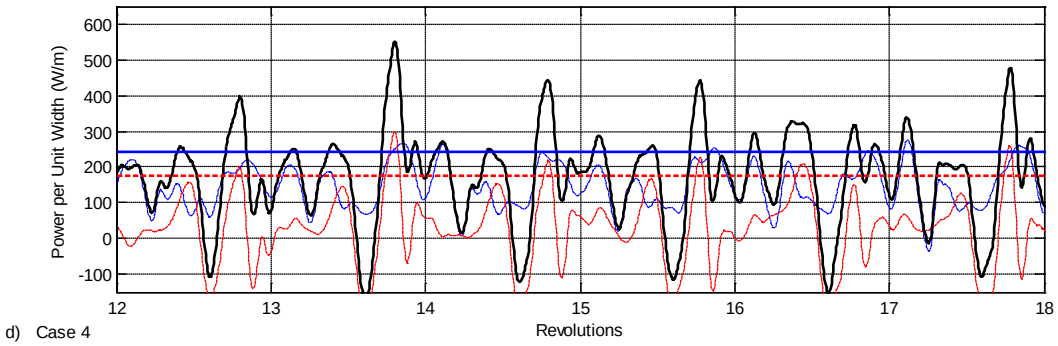

d) Case 4

Figure 53 - Shaft power and average incident wave power for two-hydrofoil wave cancellation.

The average power conversion efficiency of the device, ε_{PC}, quantifies the efficiency of the device in converting the cancelled wave power, $\bar{E}_A \cdot \varepsilon_{WC}$, into shaft power and is defined as:

$$\varepsilon_{PC} = \frac{\overline{E}_{Shaft}}{\overline{E}_A \cdot \varepsilon_{WC}}. \tag{22}$$

Summarized in Table 5 are the average power conversion efficiencies for the four completed wave cancellation simulations. The results illustrate that the average power conversion efficiency was the highest for Case 3, outperforming the other cases by 10% or more. The lowered conversion efficiencies of Case 1 and 2 can be connected to the performance of the negatively pitched hydrofoil which had a mean shaft power per unit width below zero meaning it was frequently drawing power from the system during each rotation. The lower wave conversion efficiency of Case 4 can also be attributed to the negatively pitched hydrofoil, which as shown in Figure 53, spends 1/8 of the rotation drawing power.

Table 5 - Average power conversion efficiency for wave cancelling two-hydrofoil CycWEC model.

Two Hydrofoil Power Conversion Efficiency Statistics						
Simulation #	α_1	α_2	$\bar{E}_{Shaft}$	$\bar{E}_A$	ε_{WC}	ε_{PC}
	(deg)	(deg)	(W/m)	(W/m)	%	%
1	7.5	-7.5	74.96	104.45	90.34	79.44
2	7.5	-7.5	48.75	77.78	80.91	77.47
3	10	-10	148.43	179.47	92.52	89.39
4	12.5	-12.5	174.34	241.83	91.62	78.68

7.2.7. Average Total Power Extraction Efficiency

With the average wave cancellation efficiency, and average power conversion efficiency calculated, the overall performance of the two-hydrofoil CycWEC model can be quantified. The average total power extraction efficiency, ε_{TP}, represents the ratio of total average shaft power per unit width, to the average power of the incident wave per unit width and is defined as:

$$\varepsilon_{TP} = \frac{\overline{E}_{Shaft}}{\overline{E}_{A}} = \varepsilon_{WC} \cdot \varepsilon_{PC} \,. \tag{23}$$

This efficiency is the fundamental efficiency of any wave energy converter because it determines how much of the incident wave power is being converted into useful shaft power. Table 6 contains the calculated average total power extraction efficiencies for each wave cancellation simulation. Comparing the results of Cases 1 and 2 confirms that the CycWEC will experience a decrease in total power extraction efficiency when the incident wave is smaller than required based on the pitch angles, or conversely, if the hydrofoils are not pitched to the correct angle given the wave height of the incident wave field. Based on the prescribed incident wave heights, Case 3 had the best overall performance with an ε_{TP} value of 82.7%. However it is important to note that the efficiencies of the other cases may increase for an incident wave field of different wave height. The largest quantity of power was extracted for Case 4 where $\bar{E}_{Shaft}$ = 174.34 W/m, however the overall efficiency was less than Case 3 because the incident wave field contained more power.

Table 6 - Average total power extraction efficiency for two-hydrofoil CycWEC model.

Total Power Extraction Efficiency Statistics							
Simulation #	α_1	α_2	$\bar{E}_{Shaft}$	$\bar{E}_A$	ε_{WC}	ε_{PC}	$\boldsymbol{\varepsilon_{TP}}$
	(deg)	(deg)	(W/m)	(W/m)	%	%	**%**
1	7.5	-7.5	74.96	104.45	90.34	79.44	**71.77**
2	7.5	-7.5	48.75	77.78	80.91	77.47	**62.68**
3	10	-10	148.43	179.47	92.52	89.39	**82.70**
4	12.5	-12.5	174.34	241.83	91.62	78.68	**72.09**

CHAPTER 8

8. SUMMARY

A computational fluid dynamic study was completed on the Atargis Cycloidal Wave Energy Converter (CycWEC) to investigate the wave generation and cancellation characteristics using a two-dimensional model. The numerical modeling was based on the unsteady Reynolds average Navier Stokes (URANS) equations and the free surface fluctuations were determined using the volume of fluid method. A specialized hybrid grid design was required to accurately resolve the complex viscous flow field resulting from one or more hydrofoils rotating beneath the free surface at a constant angular velocity. The research progressed incrementally from single and two-hydrofoil wave generation to numerical wave generation and finished with two-hydrofoil wave cancellation. The URANS simulations were able to model nonlinear free surface interactions and viscous effects, unlike previous inviscid simulations, and provided complete velocity and pressure fields which experimental work could not.

The specific research objectives defined at the beginning of this report were accomplished. The two-dimensional CFD model of a single hydrofoil rotating beneath a free surface at a fixed pitch angle and angular speed was developed. Its computational requirements and accuracy were optimized by a grid and time step sensitivity study. The two-hydrofoil CycWEC CFD model was developed from the original single hydrofoil CFD model. Completed URANS simulations explored the wave generation properties of the single and two-hydrofoil device. A two-dimensional numerical wave tank was constructed to generate user defined incident wave fields and validated by linear wave theory. Lastly the numerical wave tank was added to the two-hydrofoil CycWEC model for final URANS simulations that illustrate the wave power extraction efficiency of the device when subject to a regular wave field.

The single hydrofoil CFD model employed a hybrid grid to model the rotation of a modified NACA 0015 hydrofoil beneath the free surface. The model, was subject to a grid and time step study which minimized the discretization error and computational requirements. The single hydrofoil CFD model was employed for URANS simulations at α_1 = ±5°, ±7.5°, ±10°, and ±12.5°. The resulting free surface variations for all cases agree with findings of Siegel and al. [11], which concluded a rotating hydrofoil near a free surface will generate a one-side wave field, primarily consisting of a fundamental wave, and its first harmonic. A FFT analysis of the resulting wave field showed the primary wave height increased as α_1 increased, but the first harmonic wave height decreased as α_1 varied positively from α_1 = 0°, and increased as α_1 varied negatively from α_1 = 0°. The mean difference in primary wave phase angles between α_1 and -α_1 is 176.6°, suggesting that oppositely pitched hydrofoils would be near ideal for two-hydrofoil wave generation.

By examining the pressure coefficient along the hydrofoil surfaces it was determined the stagnation pressure coefficient of $C_P = 1$ is reached for all cases. For positively pitched hydrofoils, when $\theta = 0°$ there is a significant change in the pressure distribution on both the upper and lower surfaces. This is in agreement with the Parkin and Perry [23], which determined the lifting performance of a positively pitched hydrofoil, would worsen as it approached a free surface. Total hydrodynamic forces showed that for positive α_1 values a net outward radial force is generated while negative α_1 values generate a net inward radial force.

The two-hydrofoil CFD model was based on the single hydrofoil grid design and grid refinement study but was modified to include a second hydrofoil shifted by $\theta = 180°$. Initially wave generation properties of a two-hydrofoil CycWEC are predicted using the principle of superposition and single hydrofoil results. A near regular wave field having a period equal to the device period, was predicted as the pitch angles increased, meaning the harmonic waves are decreasing. This is in agreement with Siegel and al. [11] which concluded that for two hydrofoils where $\alpha_1 = -\alpha_2$ and 180° of phase shift, the harmonic waves cancel making the device ideal for regular wave cancellation.

The URANS simulations employed the two-hydrofoil CFD model where $\alpha_1 = -\alpha_2$ and $\alpha_1 = 5°$, 7.5°, 10° and 12.5°. The generated wave field trends were consistent with predictions, but upon closer inspection significant differences were noted. The discrepancies indicate the flow field is non-linear with significant interactions between the hydrofoils, resulting in generated wave heights being less than predicted. A FFT analysis of the resulting wave field showed H_1, increased as α_1 increased, reaching non-dimensional wave heights up to $H_1/c = 0.3562$ when $\alpha_1 = 12.5°$. H_2 consistently

decreased as α_1 increased reaching a minimum non-dimensional wave height of H_2/c = 0.0218 when α_1 = 12.5°. Based on these results, the ratio of H_1/H_2 increased from 2.12 to 16.34 as α_1 is increased from α_1 = 5° to α_1 = 12.5°. Examining C_p along the hydrofoil surfaces revealed the stagnation pressure coefficient does not reach a value of C_p = 1 for any case. These differences from single hydrofoil results are due to the hydrofoils operating directly in an increased wake deficit resulting from the presence of the second hydrofoil.

From the body-fixed forces, for the positively pitched hydrofoils, a sudden decrease in C_R was noted immediately after the hydrofoil passed under the free surface and continued until it reached a local minimum near the quarter revolution point (i.e., θ = 90°). For negatively pitched hydrofoils, the minimum value of $|C_R|$ occurred after the hydrofoil passed under the free surface where θ = 0°, which was followed by a sudden increase until $|C_R|$ was a maximum at θ = 90°.

The wave generation efficiency is explored in this research because a device that can generate a wave with minimum viscous losses will conversely perform better when operating as an energy extracting device. A major increase in wave generation efficiency was uncovered as the pitch angle is increased from ε_G = 65.17% when α_1 = 5° to ε_G = 93.95% when α_1 = 12.5°.

The numerical wave tank employed methods outlined by Fang and al. [18]. The mass source strength is a function of the induced horizontal and vertical velocity components of a linear progressive wave field and CFD grid size, within the mass source region. The grid was sized based on findings of Lin and Liu [16], who fixed the source size based on tank depth, and desired wave height and wavelength. The numerical wave tank is

accurate, modelling phase shifts within 0.2° of the user input. When validating the generated wave field with linear wave theory, an RMS difference of 5.94×10^{-3} was found for the location of the free surface.

The CycWEC wave cancellation CFD model combined the numerical wave tank and two-hydrofoil CFD model. Having elements totals of 380 000-420 000, and time step of Δt = 0.01255 seconds, the final simulations were computationally demanding. For all simulations the hydrofoils were rotated to equal but opposite pitch angle such that $\alpha_1 = -\alpha_2$. Four simulations were completed α_1 = 7.5° (Case 1), α_1 = 7.5° (Case 2), α_1 = 10° (Case 3), and α_1 = 12.5° (Case 4) having incident wave heights of H_A/c = 0.2684, 0.2314, 0.3528, and 0.4127, respectively, which were defined based on the two-hydrofoil wave generation research. Case 2 tested device performance when subject to a reduced H_A/c. Comparing the H_A/c and H_1/c down-wave, indicated a major decrease in wave height for all cases, meaning wave power was cancelled by the CycWEC. In terms of wave cancellation, harmonic wave heights, which decrease efficiency, were found to decrease as pitch angle is increased.

The wave cancellation efficiency of the device was found to be the lowest for Case 2 , which was subject a reduced incident wave height. For Cases 1, 3, and 4 the wave cancelation efficiency of the device varied from 90% to 93%, suggesting that the two-hydrofoil CycWEC is an effective wave cancelling device when subject to an incident wave field of appropriate height, frequency, and phase.

The average total power extraction efficiency, ε_{TP}, is the fundamental efficiency of any wave energy converter because it determines how much of the incident wave power is being converted into useful shaft power. Comparing Cases 1 and 2 confirms the total

power extraction efficiency of the CycWEC will decrease if the hydrofoils are not pitched to the correct angle given the wave height of the incident wave field. Based on the prescribed incident wave heights, Case 3 had the best overall performance with a ε_{TP} = 82.7% indicating that viscous and turbulence losses are low. The efficiencies of the other cases may increase for an incident wave field of different wave height. The largest quantity of power was extracted for Case 4 where $\bar{E}_{Shaft}$ = 174.34 W/m, however the overall efficiency was less than Case 3 because the incident wave field contained more power.

CHAPTER 9

9. FUTURE WORK RECOMMENDATIONS

After investigating the two-dimensional wave generation and cancellation properties of the CycWEC CFD models several recommendations are made as possible future research topics. Possible improvements to the computational efficiency of the simulations, the implementation of numerical wave absorbers, and the completion of supplementary wave cancellation simulations are all recommended short-term extensions of this research. Lastly several long-term research project ideas are proposed that would contribute to the ongoing research and development of the Atargis CycWEC.

9.1. Extension of Completed Research

9.1.1. Improvement of Computational Efficiency – Grid Resolution

The initial grid refinement study optimized the free surface capturing region which contains up to 80 % of the total grid elements while occupying less than 0.5 % of the total domain volume. Later in the research, the unstructured grid below the free surface

capturing region was refined and showed over a 75% improvement in spatial wave damping effects resulting from numerical dissipation. It is likely that some of the discrepancies between the results from the three grids initially used in the single hydrofoil grid refinement study were amplified by the overly coarse unstructured grid below the free surface. Completing a grid refinement study using the two-dimensional single hydrofoil CFD model developed in this research and incorporating the refined grid in the water region may illustrate that the grid designs used in this research were of higher resolution than required.

9.1.2. Implementation of Numerical Wave Absorbers

Every simulation completed during this research featured numerical beaches that extended from the ends of the domain of interest, where waves were generated and cancelled, to the vertical boundaries of the overall domain. The purpose of the numerical beach was to promote the numerical dissipation of the generated wave as they propagated towards the boundaries by incrementally increasing the grid spacing. This was done to prevent generated waves from reflecting off the boundaries back into domain. Although the domain of interest was only 30 meters in length, the numerical beaches increased the total numerical domain length to 130 meters. Just as the numerical wave tank developed in this research used a mass source region to generated waves, a momentum source region could be implemented along the boundaries to numerically absorb generated waves. This would eliminate the need for numerical beaches and reduce the overall size of the computation domain by over 70%.

9.1.3. Supplementary Numerical Wave Cancellation Testing

Due to time constraints and computational requirements of the wave cancellation simulations, two or less incident wave heights were tested for each pitch angle combination. Completing supplementary simulations that vary the incident wave height would provide a more in depth understanding of the wave power extraction efficiencies of the device when subject to oversized and undersized waves.

The wave cancellation results revealed that the negatively pitched hydrofoils were required to use shaft power each revolution while operating as an energy extraction device. The positively pitched hydrofoils did not have this problem and constantly extracted wave power through each revolution. The completion of other wave cancellation simulations where $\alpha_1 < -\alpha_2$, may prove to increase the wave power extraction efficiency. The hydrofoil with the positive pitch angle may continue to efficiently convert wave power to shaft power while the negatively pitched hydrofoil, now with a larger negative pitch angle, will spend less time drawing shaft power each revolution, potentially leading to higher device efficiency.

9.2. Potential Cycloidal Wave Energy Converter Research Projects

This research has explored several key principles applicable in the growing industry of ocean wave energy conversion. Building on the outcomes of this research it is foreseeable that future research projects could involve modelling the three-dimensional wave generation and cancellation abilities CycWEC when subject to a harmonic or irregular wave field. To model the true operating conditions of the CycWEC, the three-dimensional wave cancellation simulations would have the hydrofoils driven only by the

incident wave field by coupling the equation of motion to the CFD simulations and moving mesh would allow for active pitch angle control when subject to an irregular incident wave field.

REFERENCES

[1] J. Edwards, “Crude oil and alternate energy production forecasts for the 21st century,” AAPG Bulletin, New York, United States, 1997

[2] G. Boyle, “Renewable energy – power for a sustainable future,” Oxford University Press, 2004.

[3] R. Dean, R. Dalrymple, *Water Wave Mechanics for Engineers and Scientists*, 1st ed., World Scientific Publishing Company Limited, Singapore, 2010, vol. 2

[4] (2013) Earth Science Australia Corporate website. [Online]. Available: http://earthsci.org/education/teacher/basicgeol/ocean/waves.jpg

[5] T. Jeans, C. Fagley, S. Siegel, J. Seidel, “Irregular deep ocean wave energy conversion using a cycloidal wave energy converter,” in proceeding of the 9th EWTEC, September 2011.

[6] (2013) The Atargis Energy Corporation website. [Online]. Available: http://www.atargis.com/index.html

[7] J. Falnes, *Ocean Waves and Oscillating Systems: Linear Interactions Including Wave-Energy Extracting*, Cambridge University Press, New York, United States, 2002.

[8] C. Marburg, “Investigation on a rotating foil for wave energy conversion,” Master’s thesis, TU Delft, 1994.

[9] A. J. Hermans, E. van Sabben, and J. Pinkster, “A device to extract energy from water waves,” *Applied Ocean Research Computational Mechanics Publications*, vol. Vol 12 No. 4, p.5, 1990.

[10] E. van Sabben, “De in het snelheidsveld van lopende golven rondraaiende plaat; invloed op het vrije vloeistofoppervlak,” Master’s these, TU Delft, 1987

[11] S. G. Siegel, T. L. Jeans, and T. E. McLaughlin, “Deep ocean wave energy conversion using a cycloidal turbine,” *Applied Ocean Research, vol. 33, no. 2, pp.110-119, 2011*.

[12] S. G. Siegel, C. Fagley, S. Nowlin, “Experimental wave termination in a 2D wave tunnel using a cycloidal wave energy converter,” *Applied Ocean Research, vol. 38, no.2, pp.92-99, 2012.*

[13] C. Fagley, S. G. Siegel, J. Seidel, “Wave cancellation experiments using a 1:10 scale cycloidal wave energy converter,” in AWTCS 2012.

[14] G. I. Gretton, I.G. Bryden, S. J. Couch, D. M. Ingram, “The CFD simulation of a lifting hydrofoil in close proximity to a free surface,” Proceeding of the ASME 2010 29th International Conference on Ocean, Offshore and Artic Engineering, OMAE2010-20936, June 2010

[15] J. H. Duncan, “The Breaking and non-breaking wave resistance of two-dimensional hydrofoil,” *Journal of Fluid Mechanics*, pp.507-520, 1983.

[16] P. Lin, P. Liu, “Internal Wave-maker for Navier-Stokes Equations Models,” *Journal of Waterway, Port, Costal, and Ocean Engineering*, pp. 207-215, 1999.

[17] B. Guo, S. Steen, “Comparison of Numerical Methods for Wave Generation by VOF-based Numerical Wave Tank,” Proceeding of the ASME 2011 30th International Conference on Ocean, Offshore, and Artic Engineering, OMAE2011-49777, June 2011

[18] Z. Fang, L.Cheng, N. Zhang, “Development of 3-D Numerical Wave Tank and Application on Comb-type Breakwater,” Proceeding of the ASME 2010 29th International Conference on Ocean, Offshore and Artic Engineering, OMAE2010-20337, June 2010

[19] H. K. Versteeg, W. Malalasekera, *An Introduction to Computational Fluid Dynamics*, 2nd ed., Pearson Education Limited, England, 2007.

[20] Hirt C.W., Nichols B.D., “Volume of Fluid (VoF) Method for Dynamics of Free Boundaries”, *Journal of Computational Physics*, Vol. 39, No. 1, pp. 201-225, 1981.

[21] V.R Gopala, B. G.M van Wachem, “Volume of Fluid Method for Immiscible-fluid and Free-surface Flows,” *Chemical Engineering Journal*, vol 141, pp.204-221, December 2007

[22] M. E. McCormick, *Ocean Engineering Mechanics with Applications*, 1st ed, Cambridge University Press, New York, United States of America, 2010

[23] B. R. Parkin, B. Perry, T. Y. Wu, “Pressure distribution on a hydrofoil running near the water surface,” California Institute of Technology, Pasadena, California, Report No. 47-2, 1955.

[24] “ANSYS CFX-Solver Modelling Guide”, ANSYS Inc., Version 14.0, Canonsburg, PA, 2011

[25] S. Tavoularis, *Measurement in Fluid Mechanics,* Cambridge University Press, New York, United States of America, 2005

VITAE

Christopher John Caskey

University of New Brunswick

Bachelor of Science in Mechanical Engineering

May 2012

Publications:

Conference Presentations: Christopher Caskey, Tiger Jeans, *Analysis of a Cycloidal Wave Energy Converter using Unsteady Reynolds Averaged Navier-Stokes Simulation*, The 10th European Wave and Tidal Energy Conference, Aalborg, Denmark, September 2013